

# **A MATHEMATICAL PROCEDURE FOR GENERATED ENERGY PREDICTION IN PV ARRAYS BY CONSIDERING PARTIAL SHADING, DEGRADATION, AND DIFFERENT PV CELL TECHNOLOGIES**

**Mariana Durango Flórez**

**Maestría**  
en Automatización y Control Industrial

Directores: Ph.D. D. Gonzalez Montoya  
Ph.D. L. A Trejos Grisales



**Institución Universitaria**

*Instituto Tecnológico Metropolitano*  
*Facultad de Ingeniería*  
Medellín, 2023



# ACKNOWLEDGEMENTS

I want to thank all the members of the Electronics and Renewable Energy Laboratory of the Instituto Tecnológico Metropolitano Santiago Acevedo Pérez, Juan Pablo Villegas Ceballos, Elkin Henao Bravo, Kevin mith, Miguel Ángel Robles, Cristian Escudero, Jhon Jairo Montano, Andrés Felipe Tobón and Bonie Restrepo for their emotional support, for their help in the experimental tests and in general in the development of this thesis. To my directors Luz Adriana Trejos Grisales and Daniel González Montoya, for their support not only academically but personal, their motivation throughout my research and teaching career for the last 6 years, as well as the development of this thesis with the knowledge they provided me.

And finally, to my family for all the support presented during the elaboration of this work.



# ABSTRACT

This document describes the development of a mathematical procedure to quantify the power loss in photovoltaic (PV) arrays, considering different technologies (i.e. mono-crystalline, poly-crystalline, and half-cell), partial shading patterns, and degradation types (i.e. soiling, exposure time and hot-spot). For this, a classification of different degradation types is performed to choose the appropriate degradation type for the experimental tests. For the impact of shading on the power generated, experimental tests were carried out with different shading patterns whereby a percentage of power loss was obtained regarding the different shading patterns studied based on the total solar radiation conditions. From the results, it was obtained that the diagonal shading pattern generates the least amount of power loss with a fill factor of 0.807 and a percentage of lost power of 19.216%. With the experimental tests performed in which different degradation test scenarios were taken into account, different mathematical methods were used with the collected data: a genetic algorithm for parameter estimation based on the single diode model (SDM) from the experimentally obtained curves, then an analytical method based on the Lambert W function for the calculation of the SDM parameters using the datasheet values of each PV panel under study to emulate a healthy PV panel, and the last method was a brute force using a Newton-Raphson with which an additional parameter ( $\delta$ ) was introduced to quantify the loss of the power supplied by the change in the parameters of series resistance  $R_s$  and shunt resistance  $R_{sh}$ . The results obtained from the methods described previously applied to the three PV panels under study are analyzed and it can be deduced that under the study conditions (i.e. soiling and no-soiling), the half-cell technology has the lowest power loss with 26.34% with respect to the P-V curve obtained of the healthy PV.

In turn, the quantification of power loss for the degradation test scenarios also showed that the half-cell technology has the lowest power loss at 27.55%. This procedure presents a method to give versatility to the calculation of PV modeling and PV array sizing since it considers the major causes of power loss, i.e., shading and degradation, and how they affect each PV technology.

**Keywords:** Photovoltaic models, degradation, PV panel, photovoltaic technologies, partial shading patterns, numerical methods.



# CONTENTS

<b>Acknowledgements</b>	<b>iii</b>
<b>Abstract</b>	<b>v</b>
<b>List of Figures</b>	<b>ix</b>
<b>List of Tables</b>	<b>xi</b>
<b>General index</b>	<b>xi</b>
<b>Introduction</b>	<b>xiii</b>
Basic concepts on PV arrays . . . . .	xiii
Bibliography . . . . .	xviii
<b>1 Degradation in photovoltaic panels</b>	<b>1</b>
1.1 Introduction . . . . .	1
1.2 Degradation causes and modes . . . . .	1
1.3 Detection methodologies . . . . .	4
1.4 Methodologies for measuring degradation . . . . .	6
Bibliography . . . . .	9
<b>2 Shadow impact on PV arrays</b>	<b>13</b>
2.1 Introduction . . . . .	13
2.2 Partial shading patterns . . . . .	13
2.3 Reconfiguration of PV arrays to mitigate shadow impact . . . . .	16
2.3.1 Mathematical procedure for PV losses quantification . . . . .	17
2.3.2 BF technique. . . . .	18
2.3.3 Identification of the optimal configuration. . . . .	19
2.3.4 Study cases for evaluation . . . . .	20
Bibliography . . . . .	25
<b>3 Parameter identification procedure and P-V curve calculation</b>	<b>29</b>
3.1 Introduction . . . . .	29
3.2 Genetic algorithm (GA) . . . . .	29
3.3 P-V curve calculation using $\delta$ parameter . . . . .	30
3.3.1 Analytical technique for ideal PV parameters . . . . .	32
3.3.2 Graphical interface for users . . . . .	35
Bibliography . . . . .	36
<b>4 Experimental tests and results</b>	<b>37</b>
4.1 Introduction . . . . .	37
4.2 Experimental test platform . . . . .	37
4.3 Soiling Impact on PV panels . . . . .	40
Bibliography . . . . .	46
<b>5 Conclusions</b>	<b>47</b>
<b>A Appendixes</b>	<b>49</b>
A.1 Python App for PV array sizing . . . . .	49
A.1.1 Buttons functionality . . . . .	51
A.1.2 PV array sizing computation . . . . .	54

---

A.1.3	Appendix . . . . .	56
A.1.4	Storing system computation . . . . .	66
A.2	Analysis of Electrical Models for Photovoltaic Cells under Uniform and Partial Shading Conditions	67
A.2.1	Introduction . . . . .	67
A.2.2	Models' mathematical representation . . . . .	69
A.2.3	Proposed parameter estimation technique. . . . .	71
A.2.4	Results and discussion . . . . .	73
A.2.5	Conclusions . . . . .	78
A.3	A low-cost system for real-time measuring of the sunlight incident angle using IoT. . . . .	78
A.3.1	Hardware in context . . . . .	78
A.3.2	Hardware description . . . . .	81
A.3.3	Design files . . . . .	83
A.3.4	Bill of materials . . . . .	84
A.3.5	Build instructions . . . . .	84
A.3.6	Operation instructions. . . . .	85
A.3.7	Validation and characterization . . . . .	85
A.3.8	Application example . . . . .	92
A.4	Products . . . . .	93
	Bibliography . . . . .	95



# LIST OF FIGURES

1	PV cell, PV panel, PV array. Adapted from: [27]	xiv
2	Single Diode Model circuit	xv
3	Double Diode Model circuit	xv
4	Bishop model circuit	xv
1.1	Corrosion in PV panel. Adapted from: [6]	2
1.2	PID in PV panel. Adapted from: [9]	2
1.3	EVA degradation in PV panel. Adapted from: [14]	3
1.4	Aging in PV panels. Adapted from: [17]	3
1.5	PV panel degraded due to exposure time. Adapted from: [20]	4
1.6	Soiling in PV panel. Adapted from: [23]	4
1.7	I-V curves of healthy and degraded PV panel	5
1.8	Dark I-V curve of solar cell before and after PID. Adapted from: [7]	5
1.9	PV panel with hot spot. Adapted from: [33]	6
1.10	Summary of degradation in PV panels	8
2.1	Long Narrow: real case. Adopted from: [11]	14
2.2	Diagonal: real case. Adapted from: [12]	14
2.3	Short narrow: real case. Adopted from: [13]	15
2.4	Short wide: real case. Adopted from: [14]	15
2.5	Example of connection matrix of a PV array.	18
2.6	Objective function vs. iteration time.	20
2.7	P-V curves for irradiance matrix of Table 2.3.	21
2.8	P-V curves for irradiance matrix of Table 2.5.	22
2.9	Diagonal shading pattern. (a) Shading pattern 1; (b) shading pattern 2; (c) shading pattern 3; (d) shading pattern 4.	23
2.10	Rectangular shading pattern. (a) Shading pattern 1; (b) shading pattern 2; (c) shading pattern 3; (d) shading pattern 4.	23
2.11	Shadow pattern vs. power production.	24
2.12	Shading pattern vs. execution time.	24
3.1	Parameter estimation for Hybrytec qm5-85/12 solar panel	31
3.2	Parameter estimation for SP090 solar panel	32
3.3	Parameter estimation for JKM400M-72H-V solar panel	33
4.1	Experimental setup	38
4.2	Connection scheme of the experimental setup	38
4.3	Experimental test for hybrytec qm5-85/12 PV panel	39
4.4	Experimental test for 90W solar panel	39
4.5	Faults present in 90W solar panel	40
4.6	Experimental test for JKM400M-72H-V solar panel	40
4.7	P-V curve of JKM400M-72H-V panel	41
4.8	P-V curve of SP090 panel	41
4.9	P-V curve of hybrytec qm5-85/12 panel	42
4.10	P-V curves of JKM400M-72H-V panel with and without soiling	43
4.11	P-V curves of hybrytec qm5-85/12 panel with and without soiling	43
4.12	P-V curves of S090 panel with and without soiling	44

A.1	Main window	49
A.2	Secondary window for computation by area	50
A.3	Secondary window for computation by energy	51
A.4	Instructions for main window use	52
A.5	Instructions for computation by area	52
A.6	Instructions for computation by energy to supply	52
A.7	Solar radiation profile used in the example	54
A.8	Computation by energy example	55
A.9	Example of computed data by energy option	55
A.10	Exported data of computation by energy option	56
A.11	Main data of the NSRDB Data Viewer	56
A.12	Data Layers view	57
A.13	Legend view	58
A.14	Query view	58
A.15	View to download data with Point	59
A.16	Form to download data	59
A.17	Window of data selection for download	60
A.18	Data selected with Full Disc option	60
A.19	Data download information	61
A.20	View of the email for data downloading	61
A.21	View example of the data downloaded from Full Disc option	61
A.22	Main view of <i>Consulta de datos hidrometeorológicos</i>	62
A.23	Weather stations view	62
A.24	Weather station information	63
A.25	Data consultation	64
A.26	Solar radiation parameter selection	65
A.27	Selection of the weather station for consult	65
A.28	Download of the selected solar radiation data	66
A.29	View of the downloaded data of the IDEAM web page	66
A.30	The electrical characteristic of a PV cell	68
A.31	Circuit diagram of the Direct-Reverse Model	70
A.32	Selection of the estimation parameters for the SDM	74
A.33	Estimation of DRM parameters for $Q_2$	75
A.34	Comparison between the experimental and estimated curves in $Q_1$ and $Q_2$ (zoom-in for $Q_2$ )	76
A.35	Comparison between the experimental and estimated curves (zoom-in for $I_{sc}$ )	77
A.36	Maximum power point for each model	77
A.37	Estimation error for each model	78
A.38	Physical prototype	81
A.39	Sensor capsule	82
A.40	Top view	82
A.41	Front view	82
A.42	Schematic	83
A.43	PV system and proposed prototype installed at $6^{\circ}14'39.9''N - 75^{\circ}33'07.0''W$	85
A.44	Energy consumption comparison for traditional ( $Mode_1$ ) and optimized ( $Mode_2$ ) modes	86
A.45	Sensors' vectorial representation at a given instant of time	87
A.46	Irradiance data for 31-08-2019	88
A.47	Irradiance data for 01-09-2019	88
A.48	Generated power	89
A.49	Higher irradiance vectors: 31-08-2019	90
A.50	Higher irradiance vectors: 01-09-2019	91

# LIST OF TABLES

1	PV models classification . . . . .	xiv
2.1	FF percentage loss . . . . .	16
2.2	GA parameters used for evaluation. . . . .	20
2.3	First case study. . . . .	21
2.4	Algorithm data. . . . .	21
2.5	Second case study. . . . .	22
2.6	Algorithm data. . . . .	22
2.7	FF percentage loss. . . . .	23
3.1	Results of parameter estimation for the PV panels under study . . . . .	34
4.1	Datasheet values for the PV panels . . . . .	37
4.2	FF percentage loss. . . . .	42
4.3	FF loss percentage . . . . .	44
A.1	Evaluation of the estimated $I_{cell}$ for each model. . . . .	72
A.2	Number of constraints for each model . . . . .	72
A.3	Parameter constraints. . . . .	73
A.4	Selection of GA variables for each model. . . . .	74
A.5	Parameters estimated for each model (mean $\pm$ standard deviation). . . . .	75
A.6	Parameters used for the best solution. . . . .	76
A.7	Relative error of some points of interest in the I-V and P-V curves. . . . .	77
A.8	Normalized integral of the irradiance . . . . .	92
A.9	PV Simulation using SAM . . . . .	93



# INTRODUCTION

Solar or photovoltaic (PV) technology are one of the most common renewable energy sources. Such a technology uses the sun as its main power source, which makes it a sustainable solution and, easy installation with relatively low maintenance [1]. Due to these advantages, global PV capacity has increased in the last few years. According to a report published by Global Data company in 2019, it was revealed an installed PV capacity of 593.9 GW and, an increased of 1,582.9 GW by 2030 is estimated [2]. Moreover the IEA (International Energy Agency) estimates an annual solar PV generation level of almost 6,970 TWh in 2030 from the current 820 TWh, which will require a yearly average generation growth of 24% during 2020-2030 [3]. A statistical report developed by the Renewable Energy Institute, shows that some of the countries with the largest cumulative PV capacity until april 2021 are: China with 254 GW, Japan with 67 GW, United States with 74 GW, Germany with 54 GW and India with 39 GW [4]. According to IRENA (International Renewable Energy Agency) 2019 report, Latin America will present a growth in the market, from 7 GW in 2018 to 280 GW by 2050. It is important to highlight that the use of such a type of clean energy is increasing in all sectors of the society [5]. In Colombia, the UPME (Unidad de Planeación Minero-Energética) studies reveal an important potential for solar energy use in regions such as La Guajira and the Caribbean coast. Additionally, Colombia has expressed its interest in including PV systems as it is stated in the program proposal of the strategic plan of science, technology and innovation in mining and energy for 2013-2022 (Propuesta de programa del plan estratégico de ciencia, tecnología e innovación en energía y minería para el período 2013-2022) [6]. This document also supports the Rational use of energy and non-conventional energy sources plan 2007-2025 (Plan de Uso Racional de Energía y de Fuentes no Convencionales de Energía 2007-2025) [7]. Finally, law 1715 of 2014 gives the guidelines for fiscal incentives in projects which use non-conventional energy sources [8].

These documents and strategies increase the confidence of both individuals and companies in using this type of energy sources, also considering that Colombia is a country with many advantages as it is located in the Equatorial Zone, as well as having a large amount of land available for the installation of solar plants.

## BASIC CONCEPTS ON PV ARRAYS

PV cell is a semiconductor device which employs the photo-electric effect to transform solar light in electrical energy. To achieve this, PV cell fabrication is based on a mix of three groups of chemical elements of the periodical table: elements from group IV, elements from group III and V, or a combination of elements from group III and VI [9]. The main goal of the cell is to absorb the largest amount of photons and produce the equivalent amount of electrical current with minimum losses. To achieve this, it is necessary to use different fabrication techniques and levels or percentages of doping (i.e. change the number of ions on the chemical structure) to increase the cell efficiency and lifetime. The most common doping technique is to mix N-type and P-type materials with different concentrations [10]. The most common materials employed in PV cell fabrication are Silicon (Si), Gallium Arsenide (GaAs), Cadmium Telluride (CdTe), Copper Indium Gallium Selenide (CIGS) and Perovskite [11].

A PV cell produces an average power of 3W. As Fig. 1 shows, PV cells are connected in series or/and parallel to form a PV panel and obtain an increase in the produced power. The connection between PV panels is known as a PV array, considering this information authors have named the different types of connections or configurations. These can be classified into two groups: regular (which follows a defined pattern) and irregular or hybrid (which are connected randomly or without a pattern). The most common regular configurations are BL (Bridge Linked), TCT (Total-Cross-Tied), SP (Series-Parallel), HC (Honey Comb). These configurations, regular and irregular can be used for large-scale photovoltaic farms where SP-TCT are the most common [12, 13].

The typical PV array output power is in a range of 100W to 100 MW, whether for house applications or large-scale photovoltaic farms [14]. Due to the versatility that PV arrays present, there are different types of PV mounting systems; taking into account the area of installation these may be ground-mounted, in which the PV array will be located on the ground [15], roof-mounted, which are located in the roof of the house or building, this option is the most used in urban environments [16].

Moreover, PV arrays can be also be installed on the facades of buildings, such an application is known as building-integrated PV systems; in this application conventional structural materials of walls, roofs and windows are replaced by PV panels [17]. On the other hand, another mounting option are the floating PV arrays, which are installed using platforms on the water [18]. Finally, the PV arrays application must also consider grid connection or stand alone operation according to the load needs.

The output power of PV cell/panel/array depends on the environment temperature and the level of solar radiation. An equivalent circuit as well as a mathematical model [19] allows to obtain the current-voltage (I-V) curve for different temperature and solar radiation levels. There are different models to represent the electrical behavior of a PV cell and, depending on the PV model, there are a defined amount of parameters that emulate their losses and physical phenomenons, whether the cell is forward-bias or reverse-bias. The most reported models for forward bias are: the single-diode model (SDM) [20] with 5 parameters, the double-diode model (DDM) [21] with 7 parameters, three-diode model (TDM) [22] with 9 parameters, dynamic model [23] with 6 parameters and, the models employed for reverse and forward-bias are Bishop Model [24] with 8 parameters and direct-reverse model (DRM) with 12 parameters minimum [25]. Fig 2 to Fig 4 shows the aforementioned circuit models highlighting that parameters  $\eta_n, I_{satn}$  describe the diode  $D_n$  in the Figure based on Shockley equation, and Table 1 has a summary of the parameters of some of the models. Studying in detail the behavior of the different models is a task that must be done since the accuracy of a PV array modeling process depends on choosing the correct model that represents the behavior of the PV panel technology. During this research work some studies were carried out which resulted in the generation of a paper reported in [26] detailed in appendix A.2.

Table 1: PV models classification

PV model	Parameters
SDM	$I_{ph}, I_{sat}, R_s, R_{sh}$ y $\eta$
DDM	$I_{ph}, I_{sat1}, I_{sat2}, R_s, R_{sh}, \eta_1$ y $\eta_2$
TDM	$I_{ph}, I_{sat1}, I_{sat2}, I_{sat3}, R_s, R_{sh}, \eta_1, \eta_2$ y $\eta_3$
Dynamic	$I_{ph}, C_D, R_D, C_T, R_s$ y $R_{sh}$
Bishop	$I_{ph}, I_{sat}, R_s, R_{sh}, \eta, m, V_{br}$ y $a$
DRM	$I_{ph}, I_{sat}, R_s, R_{sh}, \eta, V_{br1}, R_1, V_{br2}, R_2...$

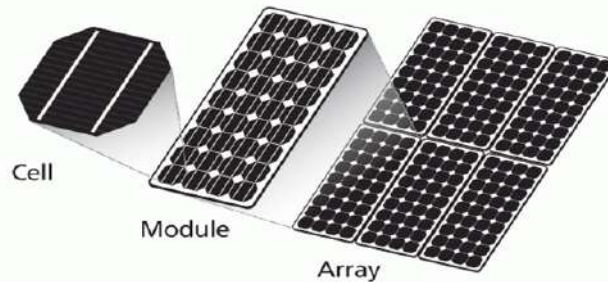


Figure 1: PV cell, PV panel, PV array. Adapted from: [27]

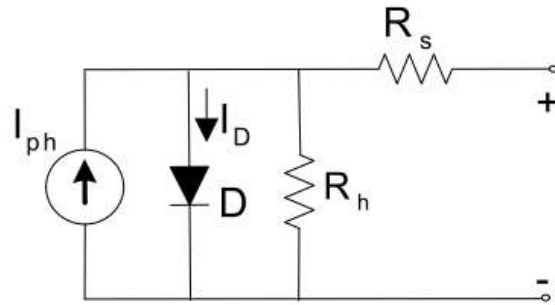


Figure 2: Single Diode Model circuit

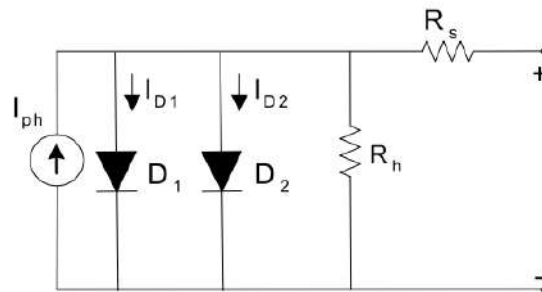


Figure 3: Double Diode Model circuit

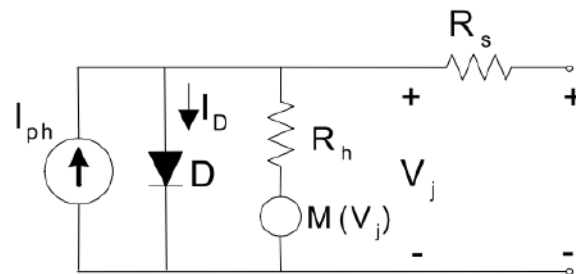


Figure 4: Bishop model circuit

The models shown above can be scaled to be used for PV arrays, this by considering the number of cells/panels in series  $N_s$  and in parallel  $N_p$ . A mathematical procedure must be employed to calculate the I-V characteristics and the maximum power generated by the PV array, considering the connections between the PV panels (i.e. configuration of the PV array). Several procedures to determine the maximum power of the PV array have been reported [28–30]; it is convenient that the method has a good trade-off between accuracy of the I-V characteristics prediction and complexity [31]; additionally, it must be able to be evaluated with non-uniform environmental conditions (i.e. presence of shadows, temperature changes, and degradation modes).

## PV POWER GENERATION ISSUES

The main goal of a PV array is to generate the maximum amount of electrical power thus, any factor that leads to a power drop must be considered in the PV array modeling to determine the real generated power. In the case of PV systems with a Maximum Power Point Tracking (MPPT) strategy, considering the factors responsible for power drops it is important to avoid falling into local minimum [32]. Conditions such degradation and shadowing are the main drawbacks that have a high effect on the generated power. Additionally, due to the technological

advancements in the fabrication of PV cells with higher efficiency, the described PV models must include the physical factors of each type of PV cell without compromising the PV model accuracy. With this in mind, the main drawbacks will be explained as follows:

- **Degradation:** Literature reports different faults in PV panels where degradation is one of the most studied phenomena since some of their modes or causes suppose an irreversible process due to its principal cause: the passing of time [33]. Nevertheless, it is necessary to monitor the state of health of the PV panels, especially if those are in a traditional outdoor PV array instead of a Building-integrated photovoltaics (BIPV). It is necessary to take measures before the state of health of the whole PV array and, its optimum operation gets compromised. A report of The National Renewable Energy Laboratory [34] has shown that solar panels have a median degradation rate of about 0.5% per year but, the rate could be higher in hotter climates and for rooftop systems. A degradation rate of 0.5% implies that production from a solar panel will decrease at a rate of 0.5% per year. The inclusion of a degradation parameter in the PV model implies the calculation of the prediction of the PV array lifetime performance and reliability by taking into account the environmental conditions to which the PV array is exposed. On the other hand, the economic analysis will provide a more accurate return and estimation date of investment.
- **Shading:** The sun is the power source for the PV cell, the presence of total or partial shading on the PV panel leads to a drop in the photon recollection and thus in the current generated. Buildings, trees, billboards, and birds are the principal causes of shading. Then to avoid it, it is imperative to recognize the environment before the PV array installation [14]. Shading is the main cause of mismatching (i.e., any electrical difference between the PV cells). Under shading conditions, the PV panel works in the second quadrant (i.e., positive current and negative voltage); here, the PV panel works as a load instead of working as a source, that is, the PV cell is reverse biased, which may cause damages to the PV panel due to the appearance of hot-spots [35]. The power-voltage (P-V) curve, obtained by multiplying the current by the voltage using Watt's law, shows several inflection points and local maximums due to the bypass diode activation used to protect the PV panel against mismatching [36]. The method employed to calculate the current and voltage of the PV array must consider with the Global Maximum Power Point (GMPP) and avoid the Local Maximum Power Points (LMPPs) for a proper representation of the PV array's behavior. To mitigate the effect of shading and increase the power supplied, it is common to use strategies to improve the MPPT or, PV array reconfiguration, that is, to implement changes between the different configurations of the PV array [37]. In the mathematical procedures, it is common to describe a set of equations that relates the incident shadow with the short-circuit current of the PV panels and the configuration of the PV array, obtaining a relation between the shading profile and the power produced by the PV array under such operating conditions.
- **PV model:** The development of the PV model is necessary for obtaining the parameters which describe the physical phenomena inside the PV cell/panel/array for energy conversion, as for obtaining I-V and P-V curves. The mathematical models of the PV are developed from an equivalent circuit and represented by equations with a specific number of variables which are estimated to accurately reproduce the I-V characteristics of the PV under study [38]. Material selection and module design are key parameters for climate-sensitive degradation and weather-induced reliability issues, as for higher efficiency levels. Therefore, the different semiconductor materials employed for PV cell fabrication and the introduction of the different amounts of doping, results in different mathematical models to represent the PV technologies such Bifacial, crystalline, PERC, so forth [39, 40]. Each model has a given complexity based on the number of parameters to estimate and the operating zone of the PV (i.e., first quadrant and/or second quadrant). For their calculation, there are several approaches such, analytical methods [41] and meta-heuristic techniques [42]. These must take into account the operating conditions: temperature, irradiance profile, and the number of cells/panels in the PV panel/array.

Since most of PV applications employ arrays instead of cells, tools to model PV arrays are required. Such tools must consider the array configuration, partial shading, and failures among other conditions which causes losses in the power generated by the PV array. In this way, a more realistic prediction will be obtained.



Considering the aforementioned, this work aims to the development of a mathematical procedure based on analytical and metaheuristic techniques for solving the PV model considering partial shading patterns and degradation to obtain the power generated by the PV panels. Additionally, this contribution considers PV panels of different technology to add versatility (i.e. monocrystalline, polycrystalline, and half-cell). This work proposes as well a power loss quantification analysis for degradation and shading scenarios. This work is organized as follows: Chapter 1 exposes the causes, detection methodologies and measure methods for PV panel degradation. Chapter 2 refers to the impact of shading patterns more employed in literature in the deliver power of PV arrays. Chapter 3 explains the mathematical procedure performed for the calculation of the power-voltage (P-V) profiles considering 3 different PV technologies and degradation in the PV panels. Chapter 4 presents the experimental results and the quantification of the power losses due to the conditions of shading and degradation. Finally, Chapter 5 describe the conclusions of the work.

## BIBLIOGRAPHY

- [1] International Energy Agency. Snapshot of global pv markets 2016. Technical report, International Energy Agency (IEA), 2017.
- [2] GlobalData. Solar photovoltaic (pv) market, update 2019 – global market size, market share, average price, regulations, and key country analysis to 2030. url <https://www.globaldata.com/>, 2019.
- [3] International Energy Agency. Solar pc analysis. url <https://www.iea.org/reports/solar-pv>, 2020.
- [4] Renewable Energy Institute. Solar pv cumulative installed capacity in selected countries (gw). url <https://www.renewable-ei.org>, 2021.
- [5] International Renewable Energy Agency. Future of solar photovoltaic: Deployment, investment, technology, grid integration and socio-economic aspects (a global energy transformation: paper). Technical report, IRENA, 2019.
- [6] Colciencias, M. d. Energía, U. d. Minero-Energética, and C. PIEM. Plan estratégico de ciencia, tecnología e innovación en energía y minería. bogotá: Dirección de desarrollo tecnológico e innovación. Technical report, Colciencias, 2019.
- [7] UPME and Consorcio Baricloche BRP. Consultoría para la formulación estratégica del plan de uso racional de energía y fuentes no convencionales de energía 2007-2025. Technical report, UPME, 2017.
- [8] Congreso de Colombia. Ley 1715 de 2014 por medio de la cual se regula la integración de las energías renovables no convencionales al sistema energético nacional. Technical report, REPÚBLICA DE COLOMBIA – GOBIERNO NACIONAL, 2014.
- [9] C.B.Honsberg and S.G.Bowden. Photovoltaics education website. url [www.pveducation.org](http://www.pveducation.org), 2019.
- [10] S. Sharma, K. K. Jain, and A. Sharma. Solar cells: In research and applications—a review. *Materials Sciences and Applications*, 6:1145–1155, 2015.
- [11] Solar Energy Technologies Office. Solar photovoltaic cell basics. url <https://www.energy.gov/eere/solar/solar-photovoltaic-technology-basics>, 2022.
- [12] N. Mishra, A. Yadav, R. Pachauri, Y. Chauhan, and V. Yadav. Performance enhancement of pv system using proposed array topologies under various shadow patterns. *Solar Energy*, 157:641–656, 2017.
- [13] S. Bana and R. P. Saini. Experimental investigation on power output of different photovoltaic array configurations under uniform and partial shading scenarios. *Energy*, 127:438–453, 2017.
- [14] R.A. Messenger and J. Ventre. *Photovoltaic Systems Engineering*, chapter INTRODUCTION TO PV SYSTEMS, pages 47–110. Taylor & Francis, CRC Press LLC, 2000 N.W. Corporate Blvd., Boca Raton, Florida 33431, 2nd edition, 2005.
- [15] O. Kwon, S. . Lee, J. Kwon, H. Jo, and H. Cha. The deduction of generation efficiency coefficient of the floating pv systems compared to ground-mounted pv systems based on their operation-data analysis. *Transactions of the Korean Institute of Electrical Engineers*, 68:717–724, 2019.
- [16] V. B. Shalini, G. V. Goud, and C. R. Charan. Grid connected rooftop solar pv system: A pre-feasibility estimation using pvsol premium and system advisor model(sam). *International Journal of Scientific and Technology Research*, 8:1711–1716, 2019.
- [17] A. Ghosh. Potential of building integrated and attached/applied photovoltaic (bipv/bapv) for adaptive less energy-hungry building's skin: A comprehensive review. *Journal of Cleaner Production*, 276:123343, 2020.
- [18] R. Cazzaniga, M. Cicu, M. Rosa-Clot, P. Rosa-Clot, G.M. Tina, and C. Ventura. Floating photovoltaic plants: Performance analysis and design solutions. *Renewable and Sustainable Energy Reviews*, 81:1730–1741, 2018.

- [19] J. Prasanth Ram, Himanshu Manghani, Dhanup S. Pillai, T. Sudhakar Babu, Masafumi Miyatake, and N. Rajasekar. Analysis on solar pv emulators: A review. *Renewable and Sustainable Energy Reviews*, 81:149–160, 2018.
- [20] J. Su, Y. Zhang, C. Zhang, T. Gu, and M. Yang. Parameter extraction of photovoltaic single-diode model using integrated current-voltage error criterion. *Renewable Sustainable Energy*, 12:043704, 2020.
- [21] V. Chin, Z. Salam, and K. Ishaque. An accurate and fast computational algorithm for the two-diode model of pv module based on a hybrid method. *IEEE TRANSACTIONS ON INDUSTRIAL ELECTRONICS*, 64:6212–6222, 2017.
- [22] V. Khanna, B. Das, D. Bisht, Vandana, and P. Singh. A three diode model for industrial solar cells and estimation of solar cell parameters using pso algorithm. *Renewable Energy*, 78:105–113, 2015.
- [23] G. Petrone, C. A. Ramos-Paja, and G. Spagnuolo. *Photovoltaic Sources Modeling*. IEEE PRESS, 2017.
- [24] Idriss Hadj Mahammed, Amar Hadj Arab, Smail berrah, Yahia Bakelli, Messaouda Khennene, Samir Hamid Oudjana, Amor Fezzani, and Layachi Zaghba. Outdoor study of partial shading effects on different pv modules technologies. *Energy Procedia*, 141:81–85, 2017. Power and Energy Systems Engineering.
- [25] A. Zegaoui, M. Boutoubat, J.P. Sawicki, E.Z. Kessaissia, A. Djahbar, and M. Aillerie. Enhanced model of photovoltaic cell/panel/array considering the direct and reverse modes. *Technologies and Materials for Renewable Energy, Environment and Sustainability AIP Conf. Proc.*, pages 030015–1—030015–6, 1968. AIP Publishing.
- [26] Bonie Johana Restrepo-Cuestas, Mariana Durango-Flórez, Luz Adriana Trejos-Grisales, and Carlos Andrés Ramos-Paja. Analysis of electrical models for photovoltaic cells under uniform and partial shading conditions. *Computation*, 10(7), 2022.
- [27] Narasimhan Santhanam. Solar panels – a nice package to capture the sun! url <http://www.solarmango.com/scp/solar-panels-a-nice-package-to-capture-the-sun/>, 2021.
- [28] Xiangyun Qing, Hao Sun, Xiangsai Feng, and C. Y. Chung. Submodule-based modeling and simulation of a series-parallel photovoltaic array under mismatch conditions. *IEEE Journal of Photovoltaics*, 7(6):1731–1739, 2017.
- [29] Eloy Díaz-Dorado, José Cidrás, and Camilo Carrillo. Discrete i–v model for partially shaded pv-arrays. *Solar Energy*, 103:96–107, 2014.
- [30] Juan David Bastidas-Rodríguez, Luz Adriana Trejos-Grisales, Daniel González-Montoya, Carlos Andrés Ramos-Paja, Giovanni Petrone, and Giovanni Spagnuolo. General modeling procedure for photovoltaic arrays. *Electric Power Systems Research*, 155:67–79, 2018.
- [31] G. Petrone, G. Spagnuolo, and M. Vitelli. Analytical model of mismatched photovoltaic fields by means of lambert w-function. *Solar Energy Materials and Solar Cells*, 91(18):1652–1657, 2007.
- [32] R. Faranda, S. Leva, and V. Maugeri. Mppt techniques for pv systems: Energetic and cost comparison. In *2008 IEEE Power and Energy Society General Meeting - Conversion and Delivery of Electrical Energy in the 21st Century*, pages 1–6, 2008.
- [33] Dezso Sera. Series resistance monitoring for photovoltaic modules in the vicinity of mpp. pages 4506–4510, 01 2010.
- [34] D. C. Jordan and S. R. Kurtz. Photovoltaic degradation rates—an analytical review. *Progress in Photovoltaics: Research and Applications*, 21(1):12–29, 2013.
- [35] Mahmoud Dhimish and Ghadeer Badran. Photovoltaic hot-spots fault detection algorithm using fuzzy systems. *IEEE Transactions on Device and Materials Reliability*, 19(4):671–679, 2019.

- 
- [36] G. Petrone, G. Spagnuolo, and M. Vitelli. Analytical model of mismatched photovoltaic fields by means of lambert w-function. *Solar Energy Materials and Solar Cells*, 91(18):1652–1657, 2007.
- [37] Xiaoguang Liu and Yuefeng Wang. Reconfiguration method to extract more power from partially shaded photovoltaic arrays with series-parallel topology. *Energies*, 12(8):1439, 2019.
- [38] Tong Kang, Jiangang Yao, Min Jin, Shengjie Yang, and Thanhlong Duong. A novel improved cuckoo search algorithm for parameter estimation of photovoltaic (pv) models. *Energies*, 11:1060, 04 2018.
- [39] W. Gu, T. Ma, S. Ahmed, Y. Zhang, and J. Peng. A comprehensive review and outlook of bifacial photovoltaic (bpv) technology. *Energy Conversion and Management*, 223:113283, 2020.
- [40] Amir Mosavi, Bertalan Beszedes, Imre Felde, Nádai László, and Nima Gorji. Electrical characterization of cigs thin-film solar cells by two- and four-wire probe technique. *Modern Physics Letters B*, 02 2020.
- [41] P. Upadhyay, Subrahmanyam Pulipaka, R. Kumar, and Madhav Sharma. Parameter extraction of solar photovoltaic system using lambert-w function for different environmental condition. *2016 IEEE Region 10 Conference (TENCON)*, pages 1884–1888, 2016.
- [42] Huang Wei, Jiang Cong, Xue Lingyun, and Song Deyun. Extracting solar cell model parameters based on chaos particle swarm algorithm. *2011 International Conference on Electric Information and Control Engineering, ICEICE 2011 - Proceedings*, 04 2011.

# 1

## DEGRADATION IN PHOTOVOLTAIC PANELS

### 1.1. INTRODUCTION

Degradation may be defined as the process in which the solar cell components deteriorate through time, leading to a drop in the power delivered. Since it is a natural phenomenon, it is fundamental to consider the calculation of the lifetime of the PV array. This means that it is necessary to have a general idea of its causes, recognize the different types of methodologies or tools to identify them and finally, use a performance metric to estimate the power loss per year. In this way, this chapter describes the main aspects of degradation, introducing the most common degradation causes and modes, the detection methodologies, and the performance metrics to quantify the degradation mechanisms and the power loss. The information presented allows the definition of the key aspects for the development of this thesis.

### 1.2. DEGRADATION CAUSES AND MODES

The different degradation modes correspond to two main factors: the fabrication material of the solar cell, which includes the semiconductor material (e.g., Cd, Si, Ge, among others.) and the technology developed (e.g Thin-film, Bifacial, PERC, among others). The second factor is the installation place, where the environmental variables (e.g., wind velocity, temperature, and solar radiation) and the maintenance received during the PV system work time, have a considerable impact in the delivered power[1–3]. There are different causes of degradation, the most common are:

- **Corrosion:** Consists of the metal destruction caused by electrochemical reactions due to the environment around the PV panel. It relates to water intrusion (humidity) through the laminated material. This phenomenon is common in floating PV arrays, whether with mono or poli-crystalline PV panels, since these remain in the water [4]. Corrosion also affects the connecting line between the cells and the metal edge (commonly Aluminium), leading to delamination, as Figure 4.5a shows. The humidity retention in the PV panel increases the electrical conductivity of the presenting metals, causing current leakage. The degradation due to the corrosion usually relates to the parameters of the PV model, for this case, corrosion increases the series resistance of the PV module [5].



Figure 1.1: Corrosion in PV panel. Adapted from: [6]

- Potential Induced Degradation (PID):** The degradation associated with the presence of  $Na^+$  ions is then called PID, this is due to a voltage difference between cells and earth related to climate (i.e. temperature raise) and soiling. This effect is more likely to appear in large field installations of P-type PV panels and crystalline  $Si$  [7], especially if the PV cells are not PID resistant or have an ARC (i.e. Anti Reflective Coating) and, in hot and damp weather conditions. Figure 1.2 illustrates an example of a PV cell affected by PID. In the I-V curve, if the MPP presents a decrease, this might indicate PID in the early stage and, if the open-circuit voltage decreases, this represents an advanced stage. PID is a reversible failure and can be recovered through storage at room temperature, by applying a reversed potential or, by treatment with temperature and bias voltage [8].

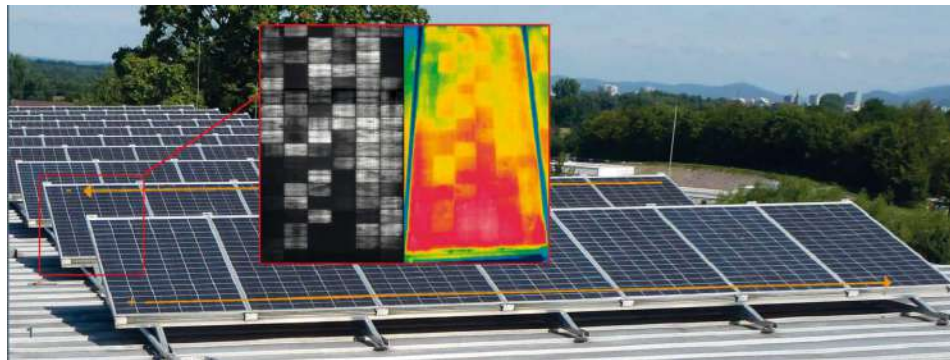


Figure 1.2: PID in PV panel. Adapted from: [9]

- Light Induced Degradation (LID):** It refers to degradation that occurs once during the first few hours of sunlight exposure, leading to an efficiency drop. It affects N-type emitter crystalline silicon and amorphous PV cells, nevertheless, it can be recovered by applying a forward bias current [10]. Regarding the PV parameters estimation, if this phenomenon is present, there is an initial rapid decay of all cell parameters (within a few minutes), followed by a slower degradation. LID increases the recombination current in the base of the PV cell which causes the diode saturation current increases [11].
- Ethylene Vinyl Acetate degradation (EVA)** EVA is an amorphous copolymer most commonly used as an encapsulant in PV panels of crystalline silicon. As Figure 1.3 shows, due to its composition, oxygen and water steam diffusivity is high, then oxidation in EVA can extend to other areas of the PV panel in which EVA is not present. EVA degradation is visually detected by browning or discoloration. This phenomenon

leads to a reduction in optical transmission, therefore decreasing the power output of a PV panel [12]. The principal causes of EVA degradation are UV rays combined with water under temperatures higher than 50 °C. By comparing the I-V curves of a new and a degraded PV panel under the same temperature and solar radiation conditions, it is noted that short circuit current decreases proportionally to EVA degradation level [13] considering that this parameter is related to PV optical properties.



Figure 1.3: EVA degradation in PV panel. Adapted from: [14]

- **Aging:** This is a direct indication that the output power of the PV panel is lower than the nominal value. Due to the P-N junction characteristics of the PV cell, is the short circuit current which changes dramatically [15]. It is also associated with exposure time since aging is a continuous process. In particular, sulfur or other pollutants, humidity, temperature, and solar radiation, can speed up the degradation process. The aging of PV panels causes the modification of the shape of the I-V curve near the  $V_{oc}$  zone and, it is therefore related to an increase in series resistance parameter of the PV model [16] or directly with a decrease in short circuit current. Figure 1.4 is an example of aged PV panels.

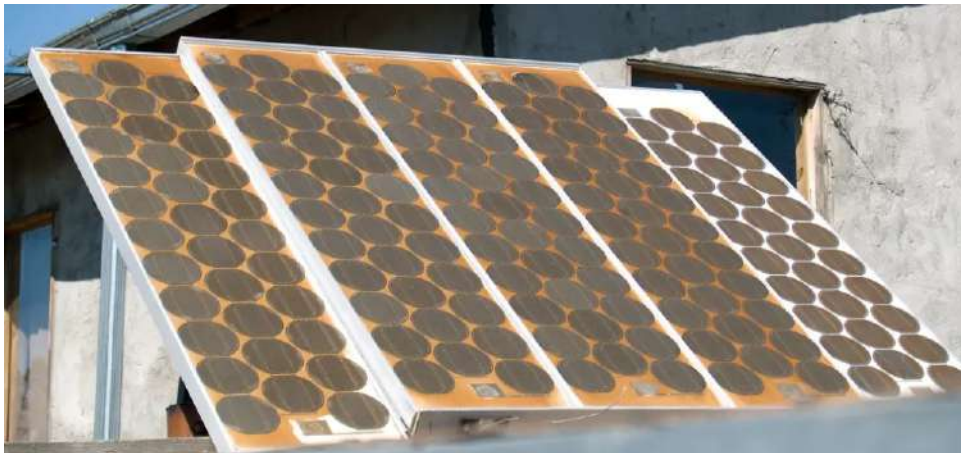


Figure 1.4: Aging in PV panels. Adapted from: [17]

- **Exposure time:** It is known that environmental factors such as temperature and season of the year affect the performance of a PV array. Hot and humid conditions usually drive the degradation of PV modules

more rapidly and severely than other environmental conditions, leading to an efficiency drop and lifetime reduction [18]. Several faults are due to exposure time to UV rays such as hot-spot, corrosion, delamination and, aging. Figure 1.5 shows some of these effects. After all, some of them are irreversible, then is imperative to perform fault diagnosis techniques to mitigate damages and avoid the increase in the maintenance costs of the PV array [19].



Figure 1.5: PV panel degraded due to exposure time. Adapted from: [20]

- Soiling:** Its principal cause is dust settlement or accumulation on the PV surface (as Figure 1.6 illustrates), which decreases the amount of solar energy collected and the amount of power generated. The amount of dust on the PV panel depends on wind velocity, PV surface properties (i.e. coating of the PV panel), and the orientation of the PV array, among others [21]. To overcome this drawback the PV array must be cleaned regularly; however, for isolated areas, researchers are developing anti-soiling and hydrophobic coatings to mitigate even more its effect on PV efficiency [22]. Soiling reduces glass transmittance, decreasing as well photocurrent generation depending on the weather conditions. Then, it can be detected by confirming the  $I_{ph}$  values for a given operating condition, or by visual inspection.



Figure 1.6: Soiling in PV panel. Adapted from: [23]

### 1.3. DETECTION METHODOLOGIES

The main objective of detection methodologies is to perform early identification of the failure so it can be fixed as soon as possible, avoiding structural damages to the PV array or a considerable loss in the delivered power. Regarding this, researchers employ different methods to detect or diagnose faults due to degradation, their use depends on the information or data available (e.g., images, I-V curve, among others). In addition, it is also important to define a proper computing tool to analyze the data, i.e. the application of intelligent algorithms such as random forest [24, 25] or analytical techniques such as non-linear regression [26]. This information enable the analysis by means of the methodologies explained as follows.

- I-V curve analysis:** In a PV array, it is common to employ an I-V curve tracer to obtain the I-V data and



calculate the delivered power, which is the variable to be maximized in the PV system [27]. Many researchers have recognized that the I-V or P-V curves are a useful and easy to use information to study the behavior of PV arrays. Fault diagnosis techniques frequently use this methodology to detect degradation. Considering the degradation modes explained above, with the I-V data, aging and corrosion can be detected by observing the slope in the I-V curve near  $V_{oc}$ . On the other hand, oxide and EVA degradation are related to the slope near  $I_{sc}$  as Fig 1.7 shows [8]. If the dark I-V curve of the PV panel is available [28] (i.e. this can be obtained if the PV panel is receiving no light), PID degradation relates with a distinct behavior of the linear I-V characteristics near  $V = 0V$  as Fig.1.8 illustrates.

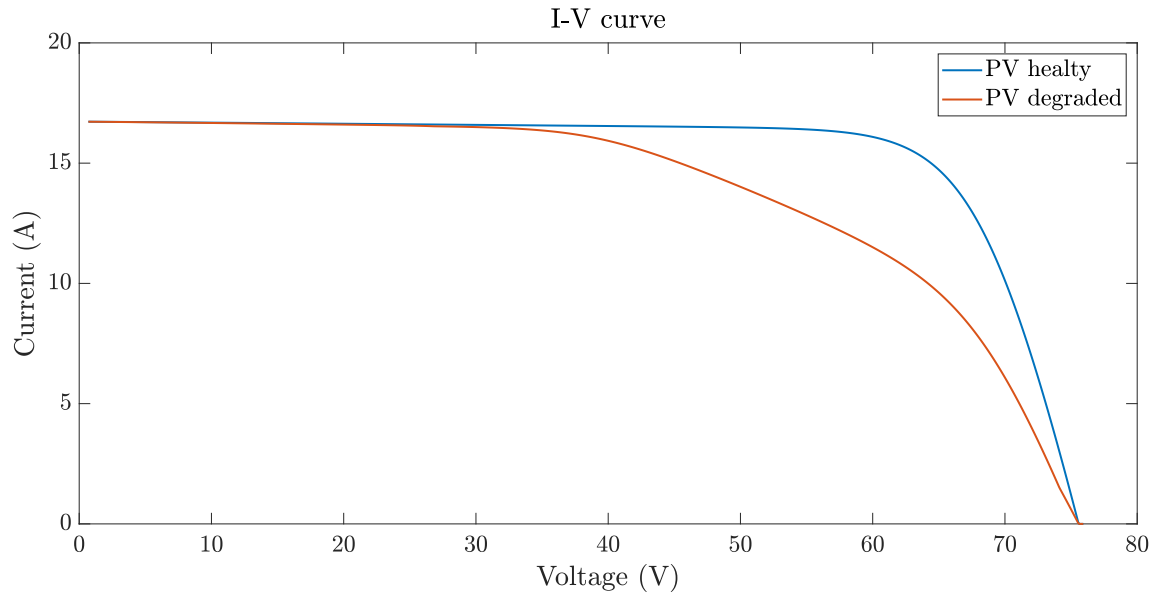


Figure 1.7: I-V curves of healthy and degraded PV panel

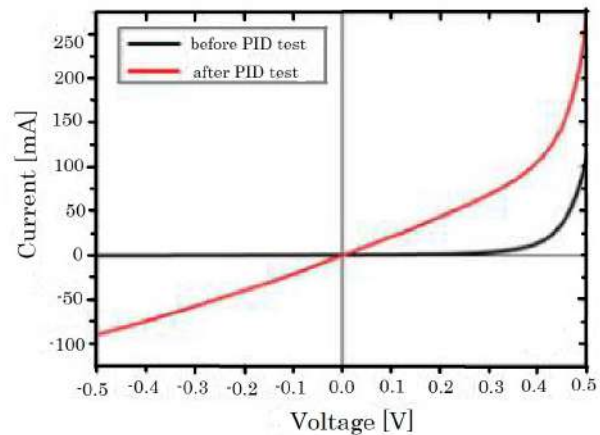


Figure 1.8: Dark I-V curve of solar cell before and after PID. Adapted from: [7]

With the I-V data it is possible to implement a parameter technique to identify the electrical parameters of the PV panel, based on the PV model (i.e., SDM, DDM, Bishop, among others). This technique links with

another detection methodology defined as the analysis of the PV model parameters, which is explained as follows.

- **Analysis of PV model parameters:** As it was introduced previously, there are different PV models to describe the electrical behavior of PV panels with different technologies [2, 29]. Each parameter of the PV model emulates a physical phenomenon inside the PV cell, hence, the relationship of the parameters with different degradation levels or modes it has become a popular method for its detection and quantification [30]. Considering the parameters in the SDM and DDM, the change in the parameters leads to the conclusion that there exists a mode of degradation related to each parameter: an increase in  $R_s$  is related to aging and a decrease in  $R_{sh}$  is related with oxide, moreover, an increase in  $\eta$  is related with the presence of corrosion and, the drop in  $V_{oc}$  or  $I_{sc}$  leads to recognizing a level of soiling on the PV panel [31]. Furthermore, using the DDM, PID and LID can be detected with an increase in  $I_{o2}$  and  $\eta_2$  [7].
- **Images:** It is a non-invasive visual inspection method commonly used to identify faults such as hot spots and PID. Due to the increase in the use of machine learning techniques, image processing is used to identify levels of dust or soiling [22, 32], browning, or EVA degradation, cell cracking, and delamination. With the different types of images such as Thermographic (IR), Scanning Electron Microscope (SEM), Electroluminescence (EL), so forth, it can be identified the anomalies associated with the different degradation modes (e.g., an irregular temperature which might lead to hot-spots as Fig. 1.9 shows) [33]. Generally, the main goal of the image analysis technique is to detect and prevent failures to minimize the power loss in the PV array.



Figure 1.9: PV panel with hot spot. Adapted from: [33]

#### 1.4. METHODOLOGIES FOR MEASURING DEGRADATION

As it was presented in the introduction, the goal of the methodologies to quantify degradation is to calculate the percentage of power decline in a certain amount of time, by considering the life time of the PV panel estimated by the manufacturer [34].

- **Performance ratio (PR):** Is a parameter to define the quality of the PV system performance. Based on its definition in the IEC 61724-1:2017 standard [35], PR is expressed as follows:

$$PR = \frac{\frac{E_{out,y}}{P_{rated}}}{\frac{G_{poa,y}}{G_0}} \quad (1.1)$$

where  $E_{out,y}$  is the amount of electricity produced from the PV array,  $P_{rated}$  is the rated peak capacity,  $G_{poa,y}$  is the amount of daily irradiance available on the plane of the PV array and,  $G_0$  is the reference irradiance, additionally, PR values are calculated on daily scales.

It is observed that, the PV arrays operates with lower PR than the actual PR. Weather parameters (i.e. temperature, wind velocity, solar radiation, so forth) are the primary reasons for lower PR. In addition, the weather parameters are responsible for the performance degradation in PV panel. Nowadays, degradation of different PV technologies is one of the major issues to increase their lifetime [36]. Manufacturers are developing new strategies to overcome the degradation effects on PV panels such as more resistant ARC (i.e. Anti-Reflective Coating) or high efficiency solar cells.

- **Analysis of change in PV model parameters:** As it was stated previously, PV parameters are associated with a specific physical behavior of degradation. By comparing the PV parameters, a degradation level can be quantified. The most employed parameters are  $R_s$ ,  $R_{sh}$ ,  $\eta$ ,  $I_{sc}$ ,  $V_{oc}$  and the MPP [37–39]. It is common to use I-V tracers in a PV array to observe its electrical behavior, then applying a parameter extraction technique with the I-V data, such as a metaheuristic algorithm, it is possible to obtain the parameters of the PV panels and estimate possible levels of degradation with the change of their parameters, this presents a preliminary stage for a deeper study and to indicate if the users must take preventive actions to avoid damages in the rest of the PV installation.
- **Degradation rate (RD):** is defined as the rate of maximum performance reduction over time and is denoted as a positive quantity commonly expressed in %/year. It also represents the reduction of  $P_{max}$  expected from a PV cell, panel, or array in the field [40]. Authors attributed high degradation rates and  $I_{sc}$  losses to delamination, oxide, and the ARC of the PV cells and front glass soiling. Different technologies might require different RD calculation methods due to the inherent differences in their seasonal components, temperature coefficients, and other physical parameters [41]. The degradation rate can be based on the comparison of the monitoring outdoor performance with the initial indoor measurements taken as references, or by applying LR (Linear Regression), a linear least square fitting method applied to the monthly effective peak power of the PV array [26] or, CSD (Classical Seasonal Decomposition) by taking into account temperature values. Authors [42] describe two models to calculate RD, Peck's model and Eyring models presented in Eq. (1.2) and (1.3).

$$R_{D, Peck} = A \exp\left(-\frac{E_a}{k_B T}\right) RH^n \quad (1.2)$$

$$R_{D, Eyring} = A \exp\left(\frac{-E_a}{k_B T} - \frac{b}{RH}\right) \quad (1.3)$$

Where RH is the relative humidity,  $E_a$  is the activation energy of the degradation process (eV), T the module temperature (K),  $k_B$  is the Boltzmann constant ( $8.62 \times 10^{-5} \frac{eV}{K}$ ), and RH is the relative humidity (%).  $A$ ,  $n$ ,  $b$ , and  $m$  are model parameters. RD is also calculated respect to the PV parameters such as Fill Factor (FF),  $V_{oc}$  and  $I_{sc}$  [43].

- **Power loss percentage:** It is related to the PR and the analysis of change in PV model parameters. The most common cause of lost power in PV panels is the exposure time, especially to solar radiation, the season of the year, since winter might cause drops in the delivered power [44] or, failures in the bypass diode [45]. Each degradation mode causes a given percentage of power decrease, the degradation mode with the highest loss percentage is EVA degradation [13]. Is necessary to consider the working conditions of the PV array for a proper power calculation if the PV array presents partial shading conditions and degradation, the GMPP can be calculated with the I-V experimental data, the comparison of the GMPP under STC ( $GMPP_{STC}$ ) with the GMPP of the experimental data ( $GMPP_{experimental}$ ) is a simple method for degradation quantification in which depending on the degradation level, for example by measuring  $R_s$ , it can be related with a particular degradation mode [46].
- **Year on year (YOY):** It is a long-term degradation rate and a modified daily performance index. The YOY degradation calculation can utilize different frequencies of time series (i.e. daily, or monthly), but it is common to use it with daily time series. It is commonly employed for soiling quantification [47]. This method calculates the rate of change between two points at the same time in subsequent years, this rate of change for all data points and all years results in a histogram of rates of change where the central tendency

will represent the overall system performance [48, 49]. For degradation studies, it can be used to estimate the lifetime of the PV array under the actual working conditions by performing a prediction based on the loss efficiency quantified by the YOY method.

- **Voltage and/or current drop:** Both parameters are directly related to environmental parameters (i.e. current is related with solar radiation and voltage with temperature) so these provide a first understanding of degradation mechanisms such as exposure time, on the other hand, aging might be related as well with  $I_{sc}$  and, the voltage and current drops in the strings of the PV array [15, 50]. If it is not possible to obtain the parameters of the PV panels, this presents a method of simple implementation as the first stage of fault identification. After discarding partial shading and failure with the wiring in the PV system, it can be done a degradation analysis employing the methodologies of section 1.3 according to the available data.

Fig. 1.10 illustrates the summary of the information described in this chapter.

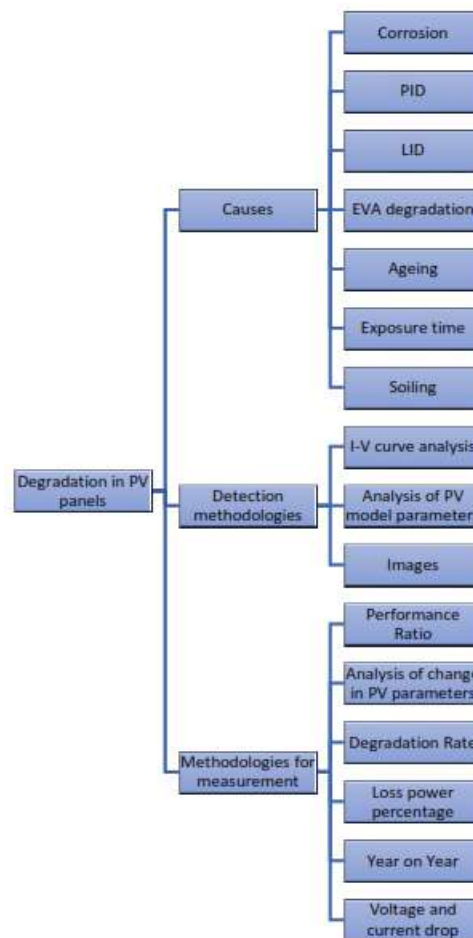


Figure 1.10: Summary of degradation in PV panels

## BIBLIOGRAPHY

- [1] H. Yang, F. Wang, H. Wang, J. Chang, D. Song, and C. Su. Performance deterioration of p-type single crystalline silicon solar modules affected by potential induced degradation in photovoltaic power plant. *Microelectronics Reliability*, 72:18–23, 2017.
- [2] W. Gu, T. Ma, S. Ahmed, Y. Zhang, and J. Peng. A comprehensive review and outlook of bifacial photovoltaic (bpv) technology. *Energy Conversion and Management*, 223:113283, 2020.
- [3] N.M. Kumar and M. Malvoni. A preliminary study of the degradation of large-scale c-si photovoltaic system under four years of operation in semi-arid climates. *Results in Physics*, 12:1395–1397, 2019.
- [4] A. Goswami and P.K. Sadhu. Degradation analysis and the impacts on feasibility study of floating solar photovoltaic systems. *Sustainable Energy, Grids and Networks*, 26:100425, 2021.
- [5] T. Hayashi, T. Nagayama, T. Tanaka, and Y. Inui. Influence of degradation in units of pv modules on electric power output of pv system. *Journal of International Council on Electrical Engineering*, 8:119–127, 2018.
- [6] Muhammad Noman, Shanshan Tu, Shahab Ahmad, Fahad Ullah Zafar, Haseeb Ahmad Khan, Sadaqat Ur Rehman, Muhammad Waqas, Adnan Daud Khan, and Obaid ur Rehman. Assessing the reliability and degradation of 10–35 years field-aged pv modules. *PLOS ONE*, 17(1):1–16, 01 2022.
- [7] D. Lausch, V. Naumann, O. Breitenstein, J. Bauer, A. Graff, J. Bagdahn, and C. Hagendorf. Potential-induced degradation (pid): Introduction of a novel test approach and explanation of increased depletion region recombination. *IEEE JOURNAL OF PHOTOVOLTAICS*, 4:834–840, 2014.
- [8] S. Sarikh, M. Raoufi, A. Bennouna, A. Benlarabi, and B. Ikken. Implementation of a plug and play i-v curve tracer dedicated to characterization and diagnosis of pv modules under real operating conditions. *Energy Conversion and Management*, 209:112613, 2020.
- [9] The Fraunhofer Institute for Solar Energy Systems. Evaluation pid – modules and power plants.
- [10] Bechara Nehme, Nacer K. M’Sirdi, Tilda Akiki, and Aziz Naamane. Contribution to the modeling of ageing effects in pv cells and modules. *Energy Procedia*, 62:565–575, 2014. 6th International Conference on Sustainability in Energy and Buildings, SEB-14.
- [11] B. Sopori, P. Basnyat, S. Devayajanam, S. Shet, V. Mehta, J. Binns, and J. Appel. Understanding light-induced degradation of c-si solar cells. *Conference Record of the IEEE Photovoltaic Specialists Conference*, pages 001115–001120, 2012.
- [12] A. Ndiaye, A. Charki, A. Kobi, Cheikh M.F. Kebe, PA Ndiaye, and V. Sambou. Degradations of silicon photovoltaic modules: A literature review. *Solar Energy*, 96:140–151, 2013.
- [13] M.T. Montero-Larocca, C.A. Cadena, and M.J.L. Tamasi. Degradación en módulos fotovoltaicos y su influencia en la pérdida de potencia. *Avances en Energías Renovables y Medio Ambiente*, 18:04.77–04.84, 2014. Trabajo seleccionado de Actas ASADES2014.
- [14] Sinovoltaics. Eva browning.
- [15] Yihua Hu, Jiangfeng Zhang, Peng Li, Dongsheng Yu, and Lin Jiang. Non-uniform aged modules reconfiguration for large-scale pv array. *IEEE Transactions on Device and Materials Reliability*, 17(3):560–569, 2017.
- [16] P. Manganiello, M. Balato, and M. Vitelli. A survey on mismatching and aging of pv modules: The closed loop. *IEEE TRANSACTIONS ON INDUSTRIAL ELECTRONICS*, 62:7276–7286, 2015.
- [17] Energy follower. How long do solar panels last? life-span explained.
- [18] A. Limmanee, S. Songtraï, N. Udomdachanut, S. Kaewniyompanit, Y. Sato, M. Nakaishi, S. Kittisontirak, K. Sriprapha, and Y. Sakamoto. Degradation analysis of photovoltaic modules under tropical climatic conditions and its impacts on lcoe. *Renewable Energy*, 102:199–204, 2017.

- [19] Y. Li, K. Ding, J. Zhang, F. Chen, and J. Wu. A fault diagnosis method for photovoltaic arrays based on fault parameters identification. *Renewable Energy*, 143:52–63, 2019.
- [20] David A. Quansah and Muyiwa S. Adaramola. Comparative study of performance degradation in poly- and mono-crystalline-si solar pv modules deployed in different applications. *International Journal of Hydrogen Energy*, 43(6):3092–3109, 2018.
- [21] W.J. Jamil, H.A. Rahman, S. Shaari, and Z. Salam. Performance degradation of photovoltaic power system: Review on mitigation methods. *Renewable and Sustainable Energy Reviews*, 67:876–891, 2017.
- [22] F. Lisco, F. Bukhari, S. Ulicná, K. Isbilir, K.L. Barth, A. Taylor, and J.M Walls. Degradation of hydrophobic, anti-soiling coatings for solar module cover glass. *Energies*, 13:3811, 2020.
- [23] César Martins. Power loss due to soiling on solar panel.
- [24] Z. Chen, F. Han, L. Wu, S. Cheng, P. Lin, and H. Chen. Random forest based intelligent fault diagnosis for pv arrays using array voltage and string currents. *Energy Conversion and Management*, 178:250–264, 2018.
- [25] Jun-Ming Huang, Rong-Jong Wai, and Geng-Jie Yang. Design of hybrid artificial bee colony algorithm and semi-supervised extreme learning machine for pv fault diagnoses by considering dust impact. *IEEE Transactions on Power Electronics*, 35(7):7086–7099, 2020.
- [26] Sofiane Kichou, Santiago Silvestre, Gustavo Nofuentes, Miguel Torres-Ramírez, Aissa Chouder, and Daniel Guasch. Characterization of degradation and evaluation of model parameters of amorphous silicon photovoltaic modules under outdoor long term exposure. *Energy*, 96:231–241, 2016.
- [27] A. Bouaichi, A.A. Merrouni, C. Hajjaj, H. Zitouni, A. Ghennioui, A.E. Amrani, and C. Messaoudi. In-situ inspection and measurement of degradation mechanisms for crystalline and thin film pv systems under harsh climatic conditions. In Elsevier, editor, *Energy Procedia*, volume 157, pages 1210–1219, Athens Greece, September 2019. Technologies and Materials for Renewable Energy, Environment and Sustainability, TMREES18, 19–21 September 2018, Athens, Greece.
- [28] Erees Q.B. Macabebe and E. Ernest Van Dyk. Parameter extraction from dark current–voltage characteristics of solar cells. *South African Journal of Science*, 104:401–404, 2008. Research letters.
- [29] S. Gulkowski, J.V Muñoz Diez, J. Aguilera Tejero, and G. Nofuentes. Computational modeling and experimental analysis of heterojunction with intrinsic thin-layer photovoltaic module under different environmental conditions. *Energy*, 172:380–390, 2019.
- [30] D.S. Pillai and N. Rajasekar. Metaheuristic algorithms for pv parameter identification: A comprehensive review with an application to threshold setting for fault detection in pv systems. *Renewable and Sustainable Energy Reviews*, 82:3503–3525, 2018.
- [31] E.L. Meyer and E.E van Dyk. Assessing the reliability and degradation of photovoltaic module performance parameters. *IEEE TRANSACTIONS ON RELIABILITY*, 53:83–, 2004.
- [32] J. Tanesab, D. Parlevliet, J. Whale, and T. Urmee. Seasonal effect of dust on the degradation of pv modules performance deployed in different climate areas. *Renewable Energy*, 111:105–115, 2017.
- [33] Giovanni Cipriani, Valeria Boscaino, Vincenzo Dio, Fabio Cardona, Gaetano Zizzo, S. Caro, and Jaser Sa’ed. Application of thermographic techniques for the detection of failures on photovoltaic modules. pages 1–5, 06 2019.
- [34] D. C. Jordan and S. R. Kurtz. Photovoltaic degradation rates—an analytical review. *Progress in Photovoltaics: Research and Applications*, 21(1):12–29, 2013.
- [35] IEC Standard. Photovoltaic system performance monitoring – guidelines for measurement, data exchange and analysis (iec 61724-1:2017). Technical report, IEC, 2017.

- [36] Pramod Rajput, Maria Malvoni, Nallapaneni Manoj Kumar, O. S. Sastry, and Arunkumar Jayakumar. Operational performance and degradation influenced life cycle environmental–economic metrics of mc-si, a-si and hit photovoltaic arrays in hot semi-arid climates. *Sustainability*, 12(3), 2020.
- [37] J.D. Bastidas-Rodriguez, E. Franco, G. Petrone, C.A. Ramos-Paja, and G. Spagnuolo. Quantification of photovoltaic module degradation using model based indicators. *Mathematics and Computers in Simulation*, 131:101–113, 2017. 11th International Conference on Modeling and Simulation of Electric Machines, Converters and Systems.
- [38] Arar Hemza, Haouam Abdeslam, Chenni Rachid, and Nouar Aoun. Simplified methods for evaluating the degradation of photovoltaic module and modeling considering partial shading. *Measurement*, 138:217–224, 2019.
- [39] Caio Meira Amaral da Luz, Fernando Lessa Tofoli, Paula dos Santos Vicente, and Eduardo Moreira Vicente. Assessment of the ideality factor on the performance of photovoltaic modules. *Energy Conversion and Management*, 167:63–69, 2018.
- [40] Alex Cronin, Stephen Pulver, Daniel Cormode, Dirk Jordan, Sarah Kurtz, and Ryan Smith. Measuring degradation rates of pv systems without irradiance data. *Progress in Photovoltaics: Research and Applications*, 22(8):851–862, 2014.
- [41] Alexander Phinikarides, Nitsa Kindyni, George Makrides, and George E. Georghiou. Review of photovoltaic degradation rate methodologies. *Renewable and Sustainable Energy Reviews*, 40:143–152, 2014.
- [42] Sascha Lindig, Ismail Kaaya, Karl-Anders Weiss, David Moser, and Marko Topic. Review of statistical and analytical degradation models for photovoltaic modules and systems as well as related improvements. *IEEE Journal of Photovoltaics*, 8(6):1773–1786, 2018.
- [43] Yoshiro Izumi and Yuzuru Ueda. Evaluation of pv module outdoor degradation rate by means of i-v curve fitting with de and linear interpolation method. In *2018 IEEE 7th World Conference on Photovoltaic Energy Conversion (WCPEC) (A Joint Conference of 45th IEEE PVSC, 28th PVSEC 34th EU PVSEC)*, pages 0409–0414, 2018.
- [44] R. Sundaramoorthy, John Delallo, J. Alexander, J. Wax, Kevin Sharpe, D. Taylor, D. Metacarpa, J. Lloyd, and P. Haldar. Correlation of power loss to string and module level performance for arrays of c-si and cigs technologies in the north east climate. *2015 IEEE 42nd Photovoltaic Specialist Conference (PVSC)*, pages 1–4, 2015.
- [45] Luigi Abenante, Francesco De Lia, Riccardo Schioppo, and Salvatore Castello. Non-linear continuous analytical model for performance degradation of photovoltaic module arrays as a function of exposure time. *Applied Energy*, 275:115363, 2020.
- [46] A. Trejos Grisales, A. Osorio Giraldo, D. Gonzalez Montoya, M. Durango Florez, and J. D. Bastidas Rodríguez. Análisis del comportamiento de arreglos fotovoltaicos con degradación operando bajo condiciones de sombreado parcial. *Revista EIA*, 17:1–10, 2020.
- [47] Michael G. Deceglie, Matthew Muller, Dirk C. Jordan, and Chris Deline. Numerical validation of an algorithm for combined soiling and degradation analysis of photovoltaic systems. In *2019 IEEE 46th Photovoltaic Specialists Conference (PVSC)*, pages 3111–3114, 2019.
- [48] Dirk C. Jordan, Chris Deline, Sarah R. Kurtz, Gregory M. Kimball, and Mike Anderson. Robust pv degradation methodology and application. *IEEE Journal of Photovoltaics*, 8(2):525–531, 2018.
- [49] Ernesto M. Solís-Alemán, Juan de la Casa, Irene Romero-Fiances, José Pedro Silva, and Gustavo Nofuentes. A study on the degradation rates and the linearity of the performance decline of various thin film pv technologies. *Solar Energy*, 188:813–824, 2019.
- [50] Christian Jones, Benjamin Ellis, Joshua Stein, and Joseph Walters. Comparative review of high resolution monitoring versus standard inverter data acquisition for a single photovoltaic power plant. pages 0715–0720, 06 2018.





# 2

## SHADOW IMPACT ON PV ARRAYS

### 2.1. INTRODUCTION

The most common effects of partial shading include power drop, changes in the MPP position in the P-V curve, system currents variations, and damage of the bypass diode. Moreover, since the PV panel is reversed biased under shading conditions, the rising temperature would delaminate the encapsulated materials and cause hot-spots [1], which leads to destructive effects such as cell or glass cracking, melting of solder or, degradation of the solar cell [2]. On the other hand, the amount of power delivered by the PV array is directly related to the geometry of the incident shadow and the number of shadowed panels.

Considering this, it is understood the relevance of an accurate irradiance measurement of the PV panel installation area and the optimal angle of its position. In this work, as part of the results, it was possible to work on a dome-type device consisting of 9 irradiance sensors including all site conditions (partial shading, reflected irradiance, etc.); this device is reported in [3] and details are given in appendix A.3.

In this way, to predict the power generated by a PV array considering real operating conditions, tools or/and procedures such as analytical techniques (e.g. Newton-Raphson) [4, 5], meta-heuristics (e.g. genetic algorithms) [6], or iterative techniques as Levenberg-Marquardt [7] are required. This chapter describes the most common shading patterns in PV arrays and the procedure selected for PV array power calculation considering a Series-Parallel configuration (i.e. PV panels are first connected in series to get a PV string, and then, these PV strings are connected in parallel to construct a PV array). In this chapter as well it is documented a genetic algorithm to perform the proper power calculation of any PV array size and technology.

### 2.2. PARTIAL SHADING PATTERNS

As it was stated previously, the shape and translucency of the incident shadow are directly related to the amount of power loss in the PV array. Therefore, there are different classifications in the literature for the most common shading patterns, such as long narrow, diagonal, short narrow and short wide. These classifications are cited in the following references [8–10]. These patterns are described as follows. Pictures of real cases are also presented in order to illustrate the patterns

- Long Narrow (LN): This case is so called as only a few of the columns in the PV array are subjected to partial shading and may appear anywhere in the array in the form of a group. Fig 2.1 shows an example of a real case of the pattern. In this case, the panels in the third columns (from left to right) and the three inferior panels in the second column are fully shadowed. The rest of the PV panels have a shade which affects a part of their surface.



Figure 2.1: Long Narrow: real case. Adopted from: [11]

- Diagonal (D): As Fig. 2.2 illustrates, the shadow is located in the panels forming any diagonal in the PV array. In the same way, the matrix for this case presents a diagonal pattern in which the shadow affects panels of the three columns.



Figure 2.2: Diagonal: real case. Adopted from: [12]

- Short narrow (SN): An example of this pattern is shown in Fig. 2.3. Generally, the shadow is on a few amount of PV panels in the array, considering a small amount of shading compared with long narrow pattern, less than half of the array.



Figure 2.3: Short narrow: real case. Adopted from: [13]

- Short Wide (SW): In this pattern (Fig. 2.4), the PV array is shaded only on one half of the array and it spreads with varying between four different irradiance levels. Commonly, there are more of the horizontally-placed PV panels shaded than the vertically-placed.



Figure 2.4: Short wide: real case. Adopted from: [14]

Different authors report other partial shading patterns, which are essentially a mix between the previously described patterns: according to [15] there is the column-wise (2 columns shaded with different irradiation levels) and row-wise (2 rows shaded with different irradiation levels) patterns. Authors in [16] defined a center-type pattern, in which the center of the PV array is shaded with different irradiation levels. For authors in [17] the classification is short broad (which is similar to row-wise and short-wide patterns) and long broad (which is similar to long narrow and column-wise patterns). In [18] horizontal shade pattern (similar to short wide), vertical shade pattern (similar to long narrow), and diagonal Shade Pattern are introduced. Additionally, in [19–21] the authors use a Puzzle pattern, similar to short narrow with 3 different levels of irradiance: Uniform irradiance of  $1000 \frac{W}{m^2}$ , uniform irradiance of  $700 \frac{W}{m^2}$  and non-uniform irradiance with both  $200$  and  $1000 \frac{W}{m^2}$ .

In order to quantify the losses with the shading patterns studied, it was performed a simulation test in Matlab-Simulink environment, considering a 6X3 PV array of JS65 Yingli PV panels. The voltage and current values of the PV array are  $V_{oc}=130.8633$  V and  $I_{sc}=15.0932$  A, with a maximum delivered power of 1.5417kW. This is considering a SP (series-parallel) configuration. The patterns of Figures 2.1 to 2.4 were recreated in a

Simulink simulation and the delivered power was calculated for every case. The procedure employed for power calculation is explained in the next subsection.

Fill factor (FF) is used to quantify the power loss caused by the described patterns. For the FF calculation for each of the shading patterns presented above, it is necessary to calculate the FF for the full illumination condition, i.e. without any shade present, to consider it as a base for power loss calculation, as expressed in Eqs. (2.1) and (2.2). Table 2.1 shows the results of each simulation.

$$FF_{full} = \frac{P_{max}}{V_{oc} \times I_{sc}} \quad (2.1)$$

$$FF_{shade} = \frac{GMPP}{V_{oc} \times I_{sc}} \quad (2.2)$$

	SW	SN	LN	D
$FF_{shade}$	0.65	0.431	0.697	0.807
$Loss\ Percentage_{shade}$ (%)	35	56.9	30.271	19.216

Table 2.1: FF percentage loss

According to Table 2.1 diagonal pattern presents the higher FF, this means that under the SP configuration, the delivered power is higher and the losses are the minimum among the patterns studied. Furthermore, the short narrow pattern is, in contrast to the diagonal pattern, in which the losses are most evident, presenting a 56.9 % drop in the delivered power.

Considering this information, in the next section a reconfiguration procedure is presented to calculate the delivered power with these shading patterns.

### 2.3. RECONFIGURATION OF PV ARRAYS TO MITIGATE SHADOW IMPACT

As was stated in the previous section, partial shading is one of the most common causes of power drop. To mitigate the effect of total or partial shading, researchers have developed several strategies in which, one of the most employed is reconfiguration. This process involves changing the physical or electrical connections of the panels in the PV array, using a switching matrix based on relays as in [22–24].

The different connections between the panels are known as configurations, which can be regular configurations following a defined pattern such as total-cross-tied (TCT), series-parallel (SP), bridge linked (BL), and honey comb (HC). Instead, irregular configurations do not follow any pattern. Depending on the shading pattern on the PV array, a given amount of power is delivered with each configuration, as it was shown in the previous section. Since the reconfiguration process aims to find the configuration which can extract the highest amount of energy, the problem of finding the correct configuration in minimal time can be addressed as an optimization problem. Considering this, the use of metaheuristic techniques in the reconfiguration process aims at the deployment of the optimum configuration for the working conditions of the PV array before the weather conditions change. In this matter, in contrast with techniques based on brute force or analytical methods, there are metaheuristic techniques such as Particle Swarm Optimization (PSO) [25], marine predator [17], Grasshopper Optimization Algorithm (GOA) [26], and Genetic Algorithm (GA) [27], which might require longer execution times to perform the reconfiguration of the PV array.

There also exists the drawback of the complexity of mathematical models used to solve the resulting equations of the PV array analysis. To address this problem, techniques such as Newton-Raphson, Lambert W, or Levenberg-Marquardt have been adopted; those techniques can lead to complex procedures to calculate the current and voltage of a PV array under a particular weather condition [28–30]. This problem has been simplified by assuming one single configuration. Some authors [27, 31] have faced the reconfiguration problem with GAs considering the TCT configuration as a static array, changing the physical position of the PV panels to disperse the shadow without changing its connection. Other authors use the SP configuration [32, 33] since it can simplify the equation system by not having a direct parallel connection between the PV strings. Nevertheless, not

considering all the configurations in the PV array decreases the versatility of the procedures, avoiding an analysis of the energy impact problem, which might lead to energy losses due to the implementation of improper configurations [34, 35].

The problem of the energy impact generated by partial shading has been a subject of study since it is one of the main sources of power losses, both for static shadows (e.g. those given by buildings) as well as dynamic shadows (e.g. those caused by clouds) [36, 37]. These studies often use metrics such as fill factor, percentage of power loss, and performance ratio [38, 39], which enable the quantification of the power loss due to shading or mismatching between PV panels characteristics. To address the reconfiguration as an optimization problem by considering the quantification of the energy impact of the partial shading conditions, the next sub-sections explain a reconfiguration procedure based on a GA to find the configuration with the maximum power. The performance of the GA is then compared with a traditional brute force algorithm to verify that the proposed solution overcomes the problem of long execution times. This procedure uses the work presented in [40] to calculate the maximum power. In this way, the current and voltage of the possible configurations of any PV array are calculated, which consider the modification of the electrical connection between the panels (i.e., dynamic reconfiguration) under partial shading conditions. Moreover, this sub-section analyzes the impact of different patterns of dynamic shading on the most common configurations, contrasting the data with those obtained by the GA using metrics such as FF to quantify the percentage of power lost due to weather conditions and the non-deployment of the appropriate configuration.

### 2.3.1. MATHEMATICAL PROCEDURE FOR PV LOSSES QUANTIFICATION

The modeling procedure presented in [40] calculates the current and voltage of any regular (e.g., SP, TCT, or BL) or irregular PV array of size  $M \times N$  ( $M$  rows,  $N$  columns) operating under uniform or partial shading conditions. The procedure is based on the single diode model (SDM) including the bypass diode [41]. Therefore, it requires seven parameters: PV current  $I_{ph}$ , saturation current  $I_{sat}$ , ideality factor  $\eta$ , series resistance  $R_s$ , parallel resistance  $R_{sh}$ , bypass diode saturation current  $I_{sat,db}$ , and bypass diode ideality factor  $\eta_{db}$  as it is shown in Equation (2.3).

$$I = I_{ph} - I_{sat} \left( e^{\frac{V + (I - I_{bd})R_s}{V_t}} - 1 \right) - \left( \frac{V + (I - I_{bd})R_s}{R_{sh}} \right) + I_{bd} \quad (2.3)$$

where  $V_t$  is the thermal voltage of the cell, which is expressed as follows:

$$V_t = \frac{\eta k T}{q} \quad (2.4)$$

In the previous expression,  $k$  is the Boltzmann's constant ( $1.3839e^{-23} J/K$ ),  $T$  is the cell temperature in Kelvin, and  $q$  is the electrical charge of electron ( $1.6e^{-19} C$ ). Moreover,  $I_{bd}$  is the current through the diode, and it is expressed as follows:

$$I_{bd} = I_{sat,db} \left( e^{\frac{-V}{V_{t,db}}} - 1 \right) \quad (2.5)$$

In partial shading conditions, parameter  $I_{ph}$  is related with the amount of solar radiation on the PV panels. Then, to express this relationship with the current of the PV array, the procedure uses a *mismatching profile*, that is, a representation of the percentage of  $I_{ph}$  under the operating conditions for each panel in the array. Equation (2.6) is an example of the mismatching profile for a  $2 \times 2$  PV array where there are 2 panels receiving 50% of solar radiation and 2 panels with full illumination (100%).

$$Mismatching_{profile} = \begin{bmatrix} 50 & 100 \\ 50 & 100 \end{bmatrix} \quad (2.6)$$

The model of the PV array is based on a SP configuration; therefore, one  $(M - 1) \times (N - 1)$  *connection matrix* ( $M_{conn}$ ) is used to represent the connections between the panels of the PV array. That matrix is filled with 0 or 1, where a 0 indicates no connection between strings and a 1 indicates connection. As an example, connection matrix corresponding to an irregular configuration is described in Figure 2.5 and the Equation (2.7) for a  $3 \times 3$  PV array.

$$M_{conn-Irregular} = \begin{bmatrix} 0 & 1 \\ 0 & 1 \end{bmatrix} \quad (2.7)$$

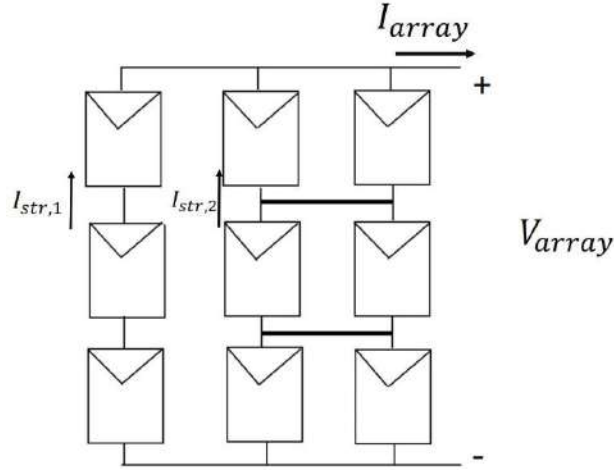


Figure 2.5: Example of connection matrix of a PV array.

Using the connection matrix and the mismatching profile, the reconfiguration process is explained as follows: the procedure adopted in [40] calculates the current for a given voltage for every possible configuration related to the PV array under analysis. Then, it calculates the delivered power and the I-V characteristics of all the configurations evaluated, deploying the configurations with the highest power. For large PV arrays, this might be a high-burden computational task due to the calculation of the I-V characteristics for all the possible configurations. In applications of energetic impact analysis, this might lead to a late reconfiguration process which implies power losses due to the shading on the PV array and could also lead to imbalances in the power supplied to the load [42]. To overcome this drawback, a GA is used for obtaining the connection matrices associated with the PV array (i.e., all the possible connections between the PV panels in the arrays), providing a faster reconfiguration process to calculate the configuration and maximizing the delivered power under a given mismatching profile, in comparison with the brute force (BF) approach explain as follows.

### 2.3.2. BF TECHNIQUE

This procedure also uses the technique of [40] for calculating the current and voltage of the PV array. Nevertheless, it calculates and evaluates the total number of possible configurations, regular and irregular, automatically for the PV array of size  $M \times N$ , finding globally the configuration that maximizes the power delivered under the given environmental conditions. For the configurations' identification, the algorithm described in [22] uses permutations between the connection matrices, that is, it permutes the position of the 0 and 1 for every configuration in the PV array. Equations (2.8) and (2.9) show the correspondent matrices of the example given in [22] for a  $3 \times 3$  array.

$$M_{conn-(1,1)} = \begin{bmatrix} 1 & 0 \\ 0 & 0 \end{bmatrix} \dashrightarrow M_{conn-(1,2)} = \begin{bmatrix} 0 & 1 \\ 0 & 0 \end{bmatrix} \quad (2.8)$$

$$M_{conn-(1,1;1,2)} = \begin{bmatrix} 1 & 1 \\ 0 & 0 \end{bmatrix} \dashrightarrow M_{conn-(1,1;2,1)} = \begin{bmatrix} 1 & 0 \\ 1 & 0 \end{bmatrix} \quad (2.9)$$

After performing all the permutations between the elements of the connection matrix, the algorithm calculates the power and current for each configuration, where the selected configuration will be the one with the maximum power under the particular environmental conditions.

Since this algorithm needs to calculate the power delivered by each configuration, this represents a computationally expensive task for large PV arrays, reflecting a high execution time. For real-time applications, it would not be an optimal option because, while the algorithm obtains the appropriate configuration, the weather conditions could change; therefore, the reconfiguration might not be effective. To overcome that problem, this work adopts a GA to perform the reconfiguration task, as explained below.

### 2.3.3. IDENTIFICATION OF THE OPTIMAL CONFIGURATION

The procedure explained in this chapter uses a GA to address the PV array's reconfiguration problem. The objective function and GA approach proposed will be explained as follows.

#### OBJECTIVE FUNCTION

PV array's reconfiguration expressed as an optimization problem implies power maximization. Based on the information given in Section 2.3.1, the objective function (OF) is given in the following equation:

$$OF = \max(I_{array} \times V_{array}) \quad (2.10)$$

In the previous function,  $I_{array}$  and  $V_{array}$  correspond to the current and voltage of the PV array, respectively.  $I_{array}$  is the summation of the string currents  $I_{str,n}$  as it is depicted in Figure 2.5.  $I_{array}$  depends on the *mismatching profile* and the number of strings of the PV array, while  $V_{array}$  depends on the number of panels connected in series to form the PV strings. As it is shown in Equation (2.10), the main target of the objective function is to calculate the maximum power generated by the configurations operating under a given set of environmental conditions, thus selecting the one with the highest power as the configuration to be deployed.

#### GENETIC ALGORITHM

Genetic algorithm was developed by [43] as an application of Darwin's natural selection theory to the artificial intelligence field. This algorithm performs its search by population analyses. Those involve creating bit chains that represent the chromosomes. The first step is to select individuals of the current population (parents) who will contribute their genes to the next generation (children). The objective function is evaluated with the current population. Then, the children with the highest objective function will pass to the next generation and, for the rest of the children, the mutation and crossover process will be applied. The chosen descendants, which are the more suitable ones, will pass to the next generation. The algorithm will continue creating descendants until a stop criterion is met (e.g., maximum number of iterations). Each of these stages is related to the objective function and the search space limits, which must be declared accurately to avoid falling into a local minimum.

#### RECONFIGURATION BASED ON GA

This procedure uses the connection matrix concept as population for the GA. After reshaping the population vector to a  $(M - 1) \times (N - 1)$  matrix, the GA evaluates the objective function for the current configuration. Equation (2.11) shows an example for the connection matrix of Equation (2.7), where [0011] is the bit chain or population created for evaluation in the GA.

$$[0011] = \begin{bmatrix} 0 & 1 \\ 0 & 1 \end{bmatrix} \quad (2.11)$$

After evaluating the objective function, as explained in sub-section 2.3.3, the GA approach selects the best individual or configuration evaluated so far, then performs the mutation and crossover processes. The objective function is evaluated for the new descendant or configuration created, and the procedure updates the best individual, which is the configuration with the highest objective function. The process repeats until the number of iterations is reached, then the GA returns the configuration with the maximum power, that is, with the highest objective function.

#### GA PARAMETERS TUNING

The type of crossover (uniform, single point, and double point) [44] was selected by performing multiple tests with the same configuration, the number of iterations, and population. Then, to choose the optimal crossover type, it was necessary to compare the execution times and the evaluation of the objective function for each test. Once the type of crossover was selected, several new tests were performed changing population size (from 20 to 80 individuals) to obtain a satisfactory trade-off between computation time and objective function value. Finally, the number of iterations was selected based on the performance of the objective function: Figure 2.6 shows that 10 iterations is the best value, since additional iterations do not improve the objective function. Following the previous procedure, the GA parameters reported in Table 2.2 were obtained, which includes a population size of 40 individuals and 10 iterations for each cycle. Moreover, a mutation of 0.01 was obtained, which means that 1%

of the individuals are subjected to mutation. Finally, the uniform crossover was selected from the results with a crossover probability equal to 1; thus, 100% of the parents genes are used in the crossover procedure.

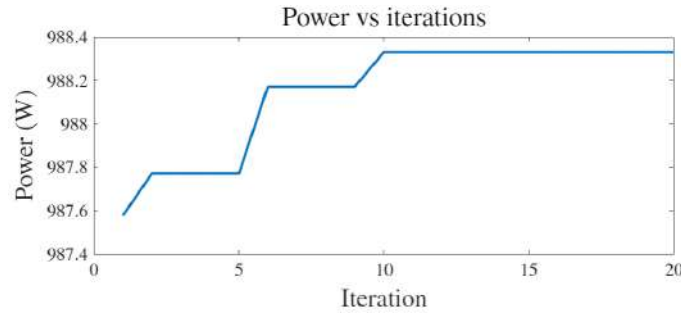


Figure 2.6: Objective function vs. iteration time.

Parameter	Value
Population	40
Iterations	10
Mutation probability	0.01
Uniform crossover	1

Table 2.2: GA parameters used for evaluation.

Then, the GA described in sub-section 2.3.3 was implemented using the parameters of Table 2.2. The GA procedure is described in Algorithm 1, where  $M$  is the number of rows of the PV array,  $N$  is the number of columns,  $nVar$  is an auxiliary variable used to simplify the pseudocode description, and  $\mu$  and  $P_c$  are the mutation and crossover values, respectively.

---

**Algorithm 1** Pseudocode of the proposed reconfiguration process

---

**Require:** Mismatching profile,  $M$ ,  $N$

**Ensure:** *Maximum power, Configuration*

- 1: Set  $nVar = (M - 1) \times (N - 1)$
  - 2: Set  $N$ ,  $t$ ,  $\mu$ ,  $P_c$
  - 3: Generate initial population
  - 4: Evaluate objective function
  - 5: Select best individual
  - 6: **for**  $i = 1$  to  $t$  **do**
  - 7:   Select parents
  - 8:   Generate descending population by using crossover and mutation
  - 9:   Evaluate objective function
  - 10:   Update best individual
  - 11:   Set Configuration = best individual and Maximum power = highest values of objective function
  - 12:   Set  $t = t + 1$
  - 13: **end for**
  - 14: **return** *Maximum power, Configuration*
- 

### 2.3.4. STUDY CASES FOR EVALUATION

The cases used to evaluate the performance of the proposed methodology were carried out at simulation level, using different irradiance profiles. Those tests consider 18 JS65 Yingli panels forming a  $6 \times 3$  PV array, and the simulations were executed using MATLAB/Simulink software on a computer with an Intel(R) Xeon(R) CPU E5-



2667@2.90 GHz 2.90 GHz (dual processor), 48 GB RAM, and Windows 10 PRO. The metrics adopted for comparison between the GA reconfiguration results and other common configurations such as SP are the execution time and maximum power. Moreover, this section presents an application case with several sizes of PV arrays, under a dynamic shading condition, to compare the proposed technique with the BF approach in terms of execution time.

Table 2.3 shows the first case corresponding to the reported mismatching matrix, along with the configurations found by the BF approach and the proposed GA. As Table 2.4 shows, the maximum power obtained for both algorithms is the same. Nevertheless, the proposed GA is 98.86% faster than the BF

**Mismatching Matrix 1**

$$\begin{bmatrix} 50 & 50 & 100 \\ 50 & 50 & 100 \\ 50 & 50 & 100 \\ 50 & 100 & 100 \\ 50 & 100 & 100 \\ 50 & 100 & 100 \end{bmatrix}$$

BF Configuration Result	GA Configuration Result	Irregular Configuration
$\begin{bmatrix} 1 & 1 \\ 1 & 1 \\ 1 & 1 \\ 1 & 0 \\ 1 & 0 \end{bmatrix}$	$\begin{bmatrix} 0 & 1 \\ 1 & 1 \\ 1 & 1 \\ 1 & 0 \\ 0 & 0 \end{bmatrix}$	$\begin{bmatrix} 0 & 0 \\ 0 & 0 \\ 0 & 0 \\ 1 & 0 \\ 0 & 1 \end{bmatrix}$

Table 2.3: First case study.

	Time (s)	Maximum Power (W)
GA	$6 \times 10^{-5}$	1075.785
BF	$5.3 \times 10^{-3}$	1075.785

Table 2.4: Algorithm data.

Figure 2.7 illustrates the power vs. voltage (P-V) curves of the GA result along with the irregular configuration given in Table 2.3 and a SP configuration. This comparison exhibits a power loss of 37.631 W between the SP, which is a commonly-used configuration, and the configuration given by the GA, while the irregular configuration exhibits a loss of 19.132 W.

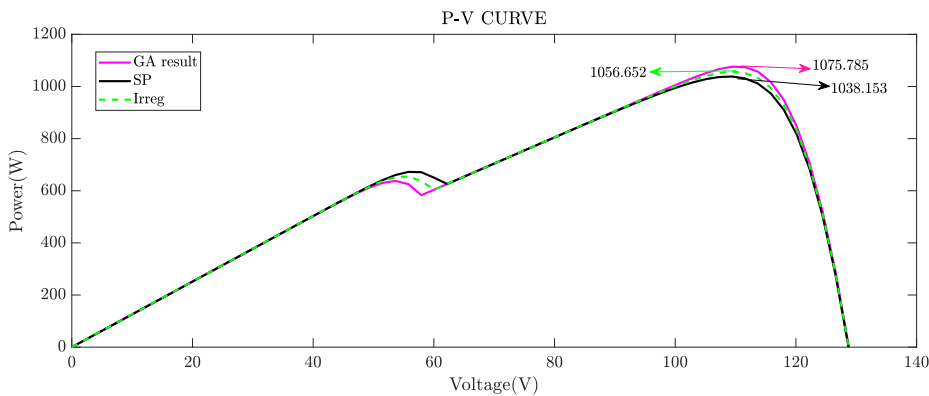


Figure 2.7: P-V curves for irradiance matrix of Table 2.3.

Tables 2.5 and 2.6 report the second case. As it was stated for the first case, the maximum power delivered is the same for both algorithms, but the proposed GA provides an improvement of 99.913% in the execution time.

### Mismatching Matrix 2

$$\begin{bmatrix} 100 & 100 & 100 \\ 100 & 100 & 100 \\ 100 & 100 & 50 \\ 100 & 50 & 50 \\ 50 & 50 & 50 \\ 50 & 50 & 50 \end{bmatrix}$$

BF Configuration Result	GA Configuration Result	Irregular Configuration
$\begin{bmatrix} 1 & 1 \\ 1 & 1 \\ 1 & 1 \\ 1 & 1 \\ 1 & 0 \end{bmatrix}$	$\begin{bmatrix} 0 & 1 \\ 1 & 1 \\ 1 & 1 \\ 1 & 1 \\ 1 & 0 \end{bmatrix}$	$\begin{bmatrix} 0 & 1 \\ 0 & 0 \\ 0 & 0 \\ 1 & 0 \\ 0 & 0 \end{bmatrix}$

Table 2.5: Second case study.

	Time (s)	Maximum Power (W)
GA	$4.02 \times 10^{-5}$	847.119
BF	$46.5 \times 10^{-3}$	847.119

Table 2.6: Algorithm data.

Figure 2.8 reports the P-V curves corresponding to the mismatching profile of Table 2.5. For this case, the SP configuration has a loss of 20.712 W, while the irregular configuration presents a loss of 15.293 W compared with the maximum power given by the proposed GA, according to the values of Table 2.6.

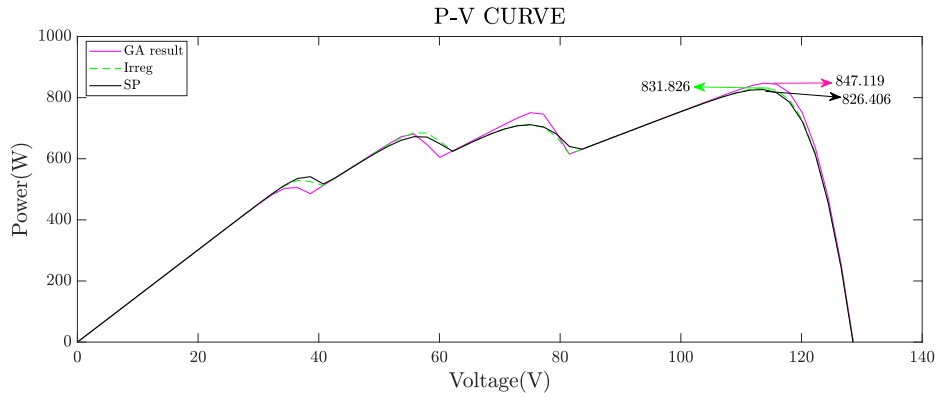


Figure 2.8: P-V curves for irradiance matrix of Table 2.5.

Table 2.7 shows the percentage of power loss for the shading scenarios previously described. First, it is necessary to calculate the FF for the full illumination condition, i.e., without any shade present, to consider that value as a base for power loss calculation. This result is obtained using the datasheet data of the JS65 Yingli and the size of the PV array, which has a maximum delivered power of 1.5417 kW. Then, using Equation (4.1), the FF of the PV array is calculated as  $FF_{full} = 0.7805$ .

As Table 2.7 shows, the SP configuration provides the highest percentage of power losses for both mismatching profiles; therefore, the configuration found by the proposed GA provides a better performance during the partial shading conditions under analysis: the GA shows an improvement of 7.493% for mismatching matrix 1 and 3.855% for mismatching matrix 2.

	Mismatching Matrix 1	Mismatching Matrix 2
$FF_{GA-result}$	0.5447	0.4289
$FF_{SP}$	0.5256	0.4184
$Loss_{GA}$ (%)	30.2114	45.0480
$Loss_{SP}$ (%)	32.6586	46.8546

Table 2.7: FF percentage loss.

The following results imply an energy impact analysis of different shadow patterns.

Figures 2.9 and 2.10 show two patterns of dynamic shadows during a day, which are used to simulate the array power production with the proposed GA. Such a performance is contrasted with the results obtained with other known configurations such as SP, TCT, and an irregular one.

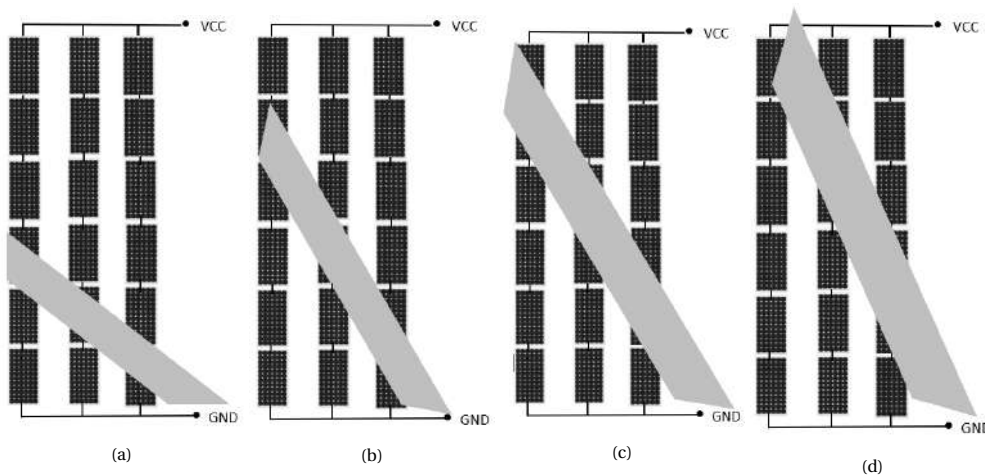


Figure 2.9: Diagonal shading pattern. (a) Shading pattern 1; (b) shading pattern 2; (c) shading pattern 3; (d) shading pattern 4.

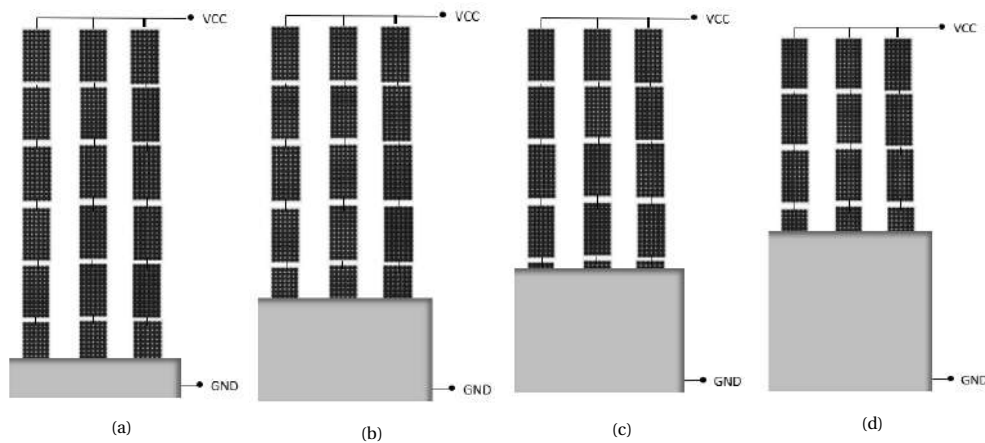


Figure 2.10: Rectangular shading pattern. (a) Shading pattern 1; (b) shading pattern 2; (c) shading pattern 3; (d) shading pattern 4.

Figure 2.11 shows a summary of the results obtained from those simulations. In the case of the diagonal pattern, the GA obtained the optimum configuration for maximizing the generated power with an irregular configuration. Comparing the power calculated by GA (i.e., irregular 2) with an SP configuration, there exists a power loss of 314 W daily, while for the irregular configuration 1 is a power loss of 100 W daily, approximately. In the case of rectangular patterns, the configuration found (i.e., SP) was also the optimum along with an irregular configuration and TCT.

According to this information, it is necessary to highlight that not adopting shading mitigation techniques might lead to a reduction in the lifetime of the PV array, economic losses, and unbalance in the loads due to the power losses produced by the shading profiles of the installation zone.

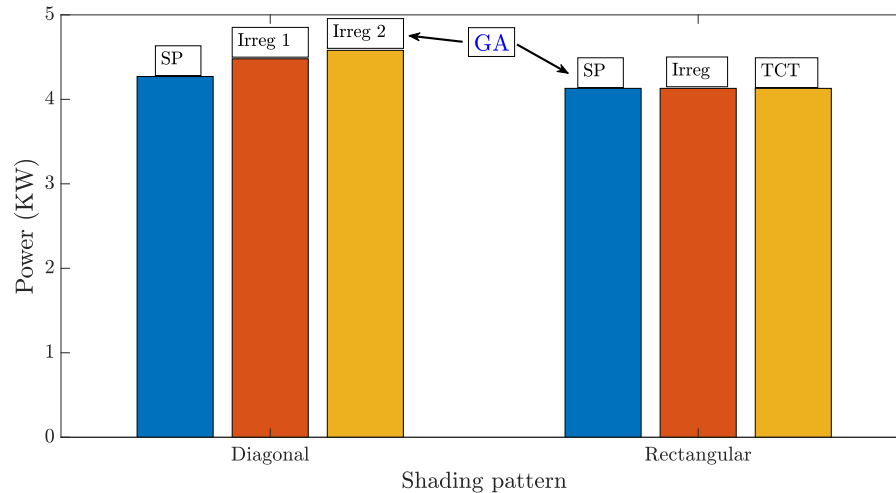


Figure 2.11: Shadow pattern vs. power production.

Figure 2.12 reports that the GA was 963% faster than the BF for the evaluation of the diagonal pattern, and the GA was 1542% faster than the BF for the rectangular pattern. Considering the execution time, the proposed procedure requires a much shorter processing time; therefore, if there exists a shading profile on the PV array daily already established, the algorithm can deploy faster the optimal configuration minimizing the power losses.

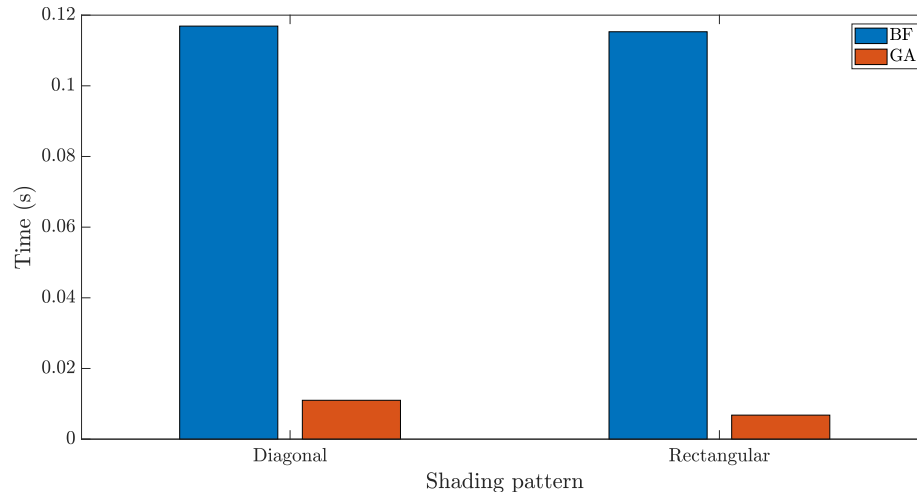


Figure 2.12: Shading pattern vs. execution time.

## BIBLIOGRAPHY

- [1] Yating Zhang, Youlin Yu, Fanying Meng, and Zhengxin Liu. Experimental investigation of the shading and mismatch effects on the performance of bifacial photovoltaic modules. *IEEE Journal of Photovoltaics*, 10(1):296–305, 2020.
- [2] Photovoltaics Education Website, howpublished = <https://www.pveducation.org/pvcdrom/welcome-to-pvcdrom/instructions>, note = Accessed: 2021-09-30.
- [3] J.S. Botero-Valencia, E. Ospina-Rojas, M. Mejia-Herrera, D. Gonzalez-Montoya, M. Durango-Flórez, and C.A. Ramos-Paja. Low-cost system for sunlight incidence angle measurement using optical fiber. *HardwareX*, 11:1–13, 2022.
- [4] Li Zhu, Qingxiang Li, Mengdong Chen, Kaiyue Cao, and Yong Sun. A simplified mathematical model for power output predicting of building integrated photovoltaic under partial shading conditions. *Energy Conversion and Management*, 180:831–843, 2019.
- [5] Guangyu Liu, Sing Kiong Nguang, and Ashton Partridge. A general modeling method for iâ€v characteristics of geometrically and electrically configured photovoltaic arrays. *Energy Conversion and Management*, 52(12):3439–3445, 2011.
- [6] Revuru Prasad and Rathinam Thiyagarajan. Kinetic gas molecular optimization method for pv system under partial shaded condition. *International Journal of Intelligent Engineering and Systems*, 13:33–43, 08 2020.
- [7] Pallavi Bharadwaj and Vinod John. Subcell modeling of partially shaded photovoltaic modules. *IEEE Transactions on Industry Applications*, 55(3):3046–3054, 2019.
- [8] S. Malathy and R. Ramaprabha. Reconfiguration strategies to extract maximum power from photovoltaic array under partially shaded conditions. *Renewable and Sustainable Energy Reviews*, 81:2922–2934, 2018.
- [9] Shubhankar Niranjana Deshkar, Sumedh Bhaskar Dhale, Jishnu Shekar Mukherjee, T. Sudhakar Babu, and N. Rajasekar. Solar pv array reconfiguration under partial shading conditions for maximum power extraction using genetic algorithm. *Renewable and Sustainable Energy Reviews*, 43:102–110, 2015.
- [10] Juan Ramón Camarillo-Peñaranda, Fabio Andrés Ramírez-Quiroz, Daniel González-Montoya, Freddy Bolaños-Martínez, and Carlos Andrés Ramos-Paja. Reconfiguration of photovoltaic arrays based on genetic algorithm. *Revista Facultad de Ingeniería Universidad de Antioquia*, pages 95 – 107, 06 2015.
- [11] Celdares. ¿cómo afectan las sombras a los paneles solares ?
- [12] Build it solar. Some more pv shading tests.
- [13] Adobe stock. Energías renovables y desarrollo sostenible.
- [14] Green Efficient Living. What is solar shading and how can you deal with it?
- [15] Mihir B. Chaudhari and Indrajit N. Trivedi. Effect of different shading patterns on photovoltaic array setups. In *2019 3rd International Conference on Recent Developments in Control, Automation Power Engineering (RDCAPE)*, pages 413–418, 2019.
- [16] B.L.r Meerimatha, G.and Rao. Genetic algorithm based pv array reconfiguration for improving power output under partial shadings. *Int. J. Renew. Energy Res*, 10:803–812, 2020.
- [17] Dalia Yousri, Thanikanti Sudhakar Babu, Eman Beshr, Magdy B. Eteiba, and Dalia Allam. A robust strategy based on marine predators algorithm for large scale photovoltaic array reconfiguration to mitigate the partial shading effect on the performance of pv system. *IEEE Access*, 8:112407–112426, 2020.

- [18] Nikesh Sharma, Smita Pareek, and Ratna Chaturvedi, Nitin Dahiya. Multiple solutions for reconfiguration to address partial shading losses in solar photovoltaic arrays. *IOP Conference Series Materials Science and Engineering*, 331:1–16, 2018.
- [19] Xiaoguang Liu and Yuefeng Wang. Reconfiguration method to extract more power from partially shaded photovoltaic arrays with series-parallel topology. *Energies*, 12(8), 2019.
- [20] Sai G. Krishna and Tukaram Moger. Optimal sudoku reconfiguration technique for total-cross-tied pv array to increase power output under non-uniform irradiance. *IEEE Transactions on Energy Conversion*, 34(4):1973–1984, 2019.
- [21] H. Heidari and M. Tarafdar Hagh. Optimal reconfiguration of solar photovoltaic arrays using a fast parallelized particle swarm optimization in confront of partial shading. *IJE TRANSACTIONS B Applications*, 32(8):1177–1185, 2019.
- [22] M Durango-Florez, Luz Adriana Trejos-Grisales, and D Gonzalez-Montoya. Matlab/simulink interface design and implementation for pv arrays reconfiguration. In *In: Zamboni W, Petrone G. (eds) ELECTRIMACS 2019. Lecture Notes in Electrical Engineering*, pages 473–486. Springer, 2020.
- [23] Mohammad Nor Rafiq Nazari, Mohammad Faridun Naim Tajuddin, Thanikanti Sudhakar Babu, Azralmukmin Azmi, Maria Malvoni, and Nallapaneni Manoj Kumar. Firefly algorithm-based photovoltaic array reconfiguration for maximum power extraction during mismatch conditions. *Sustainability*, 13(6), 2021.
- [24] Juan David Bastidas-Rodriguez, Carlos Andres Ramos-Paja, and Andres Julian Saavedra-Montes. Reconfiguration analysis of photovoltaic arrays based on parameters estimation. *Simulation Modelling Practice and Theory*, 35:50–68, 2013.
- [25] Thanikanti Sudhakar Babu, J. Prasanth Ram, Tomislav Dragičević, Masafumi Miyatake, Frede Blaabjerg, and Natarajan Rajasekar. Particle swarm optimization based solar pv array reconfiguration of the maximum power extraction under partial shading conditions. *IEEE Transactions on Sustainable Energy*, 9(1):74–85, 2018.
- [26] Ahmed Fathy. Recent meta-heuristic grasshopper optimization algorithm for optimal reconfiguration of partially shaded pv array. *Solar Energy*, 171:638–651, 2018.
- [27] Aidha Muhammad Ajmal, Vigna K. Ramachandaramurthy, Amirreza Naderipour, and Janaka B. Ekanayake. Comparative analysis of two-step ga-based pv array reconfiguration technique and other reconfiguration techniques. *Energy Conversion and Management*, 230:113806, 2021.
- [28] Fei Yu, Ying Liang, Xiaofang Sun, Gongyi Huang, and Chuanzhong Xu. Modelling solar cells' s-shaped i-v characteristics with an analytical solution to lumped-parameter equivalent circuit model. *Solar Energy*, 202:498–506, 2020.
- [29] Sid ali Blaifi, Samir Moulahoum, Bilal Taghezouit, and Abdelhakim Saim. An enhanced dynamic modeling of pv module using levenberg-marquardt algorithm. *Renewable Energy*, 135:745–760, 2019.
- [30] Kanimozhi G. and Harish Kumar. Modeling of solar cell under different conditions by ant lion optimizer with lambertw function. *Applied Soft Computing*, 71:141–151, 2018.
- [31] G. Meerimatha and B. L. Rao. Genetic algorithm based pv array reconfiguration for improving power output under partial shadings. *International Journal of Renewable Energy Research*, 10(2):803–812, 2020.
- [32] Hongmei Tian, Fernando Mancilla–David, Kevin Ellis, Eduard Muljadi, and Peter Jenkins. Determination of the optimal configuration for a photovoltaic array depending on the shading condition. *Solar Energy*, 95:1–12, 2013.
- [33] Luz Adriana Trejos-Grisales, Juan David Bastidas-Rodríguez, and Carlos Andrés Ramos-Paja. Mathematical model for regular and irregular pv arrays with improved calculation speed. *Sustainability*, 12(24), 2020.

- [34] Mohammadreza Akrami and Kazem Pourhossein. A novel reconfiguration procedure to extract maximum power from partially-shaded photovoltaic arrays. *Solar Energy*, 173:110–119, 2018.
- [35] Marco Balato, Luigi Costanzo, and Massimo Vitelli. Reconfiguration of pv modules: A tool to get the best compromise between maximization of the extracted power and minimization of localized heating phenomena. *Solar Energy*, 138:105–118, 2016.
- [36] R. Venkateswari and N. Rajasekar. Power enhancement of pv system via physical array reconfiguration based lo shu technique. *Energy Conversion and Management*, 215:112885, 2020.
- [37] Ahmed Fathy. Butterfly optimization algorithm based methodology for enhancing the shaded photovoltaic array extracted power via reconfiguration process. *Energy Conversion and Management*, 220:113115, 2020.
- [38] Dirk C. Jordan, Chris Deline, Sarah R. Kurtz, Gregory M. Kimball, and Mike Anderson. Robust pv degradation methodology and application. *IEEE Journal of Photovoltaics*, 8(2):525–531, 2018.
- [39] Ernesto M. Solís-Alemán, Juan de la Casa, Irene Romero-Fiances, José Pedro Silva, and Gustavo Nofuentes. A study on the degradation rates and the linearity of the performance decline of various thin film pv technologies. *Solar Energy*, 188:813–824, 2019.
- [40] Juan David Bastidas-Rodriguez, Luz Adriana Trejos-Grisales, D. Gonzalez-Montoya, Carlos Andrés Ramos-Paja, G Petrone, and G Spagnuolo. General modeling procedure for photovoltaic arrays. Electric Power Systems Research. *Journal of Renewable and Sustainable Energy*, 155:67–79, 2018.
- [41] Daniel Gonzalez Montoya, Juan David Bastidas-Rodriguez, Luz Adriana Trejos-Grisales, Carlos Andres Ramos-Paja, Giovanni Petrone, and Giovanni Spagnuolo. A procedure for modeling photovoltaic arrays under any configuration and shading conditions. *Energies*, 11(4), 2018.
- [42] Kamalesh Tripathy and S. Gupta. Comparative analysis of dc-dc converters for tracking mpp for roof-top pv power systems with and without partial shading condition. In *2019 International Conference on Communication and Electronics Systems (ICCES)*, pages 1125–1130, 2019.
- [43] J. Holland. *Adaptation in Natural and Artificial Systems*. Complex Adaptive Systems. 1975.
- [44] Xin-She Yang. *Nature-Inspired Optimization Algorithms*. Elsevier Insights. Elsevier, 2014.





# 3

## PARAMETER IDENTIFICATION PROCEDURE AND P-V CURVE CALCULATION

### 3.1. INTRODUCTION

This chapter presents the algorithms employed for the parameter identification and the P-V profile calculation for degradation impact in 3 panels of different technology: mono-crystalline (hybrytec qm5-85/12), poly-crystalline (solar plus S090), and half cell (JKM400M-72H-V). In this work, the PV panel is considered as a PV cell array, which can be connected in series and/or parallel as authors in [1, 2] define.

The degradation modes studied were oxide, soiling, and aging. Soiling and aging can contribute to the reverse polarization of the PV panel since they have a similar effect on the P-V curve as shading, depending on the soiling density. These degradation modes can activate bypass diodes and then provoke the appearance of several MPPs on the P-V curve, as [3] explains. This phenomenon is perceived as a mismatching effect where there is a difference between the electrical characteristics of the PV cells in the panel (e.g. shading, soiling or fabrication defects).

In this work, the procedure to find the P-V curve for each panel under study was performed with 3 techniques: a genetic algorithm (GA) to estimate the parameters from the I-V curve obtained experimentally and a previously analyzed analytical method presented in [4] that involves the Lambert W function, to calculate the parameters in real and ideal conditions, i.e., without any shadow or fault. The last method is based on P-V curves obtained experimentally considering the soiling scenarios. These curves are used along with the GA to obtain the 5 parameters of the SDM, and an additional parameter  $\delta$  is introduced to achieve a matching between the curves obtained by the algorithm and the obtained experimentally. This process will be explained as follows.

### 3.2. GENETIC ALGORITHM (GA)

This algorithm will be applied to estimate the parameters of the SDM stated in equation (3.1) considering the number of cells connected in series  $N_s$  and the number of cells connected in parallel  $N_p$ .

$$I_{pv} = N_p * I_{ph} - N_p * I_{sat} \left( e^{\left( V_{pv} + I_{pv} * \frac{N_s}{N_p} * R_s \right) / \eta V_T} - 1 \right) - \frac{(V_{pv} + I_{pv} * \frac{N_s}{N_p} * R_s)}{\frac{N_s}{N_p} * R_{sh}} \quad (3.1)$$

To apply this algorithm is necessary to define the objective function, this will be explained as follows.

#### OBJECTIVE FUNCTION

The objective function (*OF*) selected for this study, is the minimization of the root mean square error (*RMSE*) between the PV panel current measured in the experimental tests ( $I_{pvm}$ ) and the value estimated with the optimization technique ( $I_{pve}(\phi)$ ), as shown in Eq. (3.2).  $N$  represents the number of samples.

$$\min [OF(\varphi)] = \min [RMSE(I_{pve}(\varphi), I_{pvm})] = \min \left[ \sqrt{\frac{1}{N} \sum_{i=1}^N (I_{pve}(\varphi) - I_{pvm})^2} \right] \quad (3.2)$$

$I_{pve}(\varphi)$  results from evaluating the implicit equation (3.1) using the Newton Raphson method of equation (3.3) [5] and the estimated parameters (i.e  $[I_{ph}, I_{sat}, \eta, R_s, R_{sh}]$ ).  $\varphi$  is the solution vector, which includes the unknown parameters of the model to be identified and  $N$  is the number of samples.

$$\overline{x_{k+1}} = \overline{x_k} - \frac{\overline{x_k}}{J(\overline{x_k})} \quad (3.3)$$

Where  $x_k$ ,  $x_{k+1}$ ,  $f(x_k)$  and  $Jx_k$  represent the initial and updated parameter vectors, the vector of values from the residual equations(f), and the Jacobian matrix respectively.

#### PROBLEM CONSTRAINS

The constraints of the optimization problem correspond to the search ranges of the parameters to be estimated, which are defined in equations (3.4), (3.5), (3.6), (3.7) and (3.8). Those parameters correspond to the SDM model, where the search ranges should be respected to ensure a correct estimation of the parameters [2, 6].

$$\eta_{min} \leq \eta \leq \eta_{max} \quad (3.4)$$

$$R_{smin} \leq R_s \leq R_{smax} \quad (3.5)$$

$$R_{shmin} \leq R_{sh} \leq R_{shmax} \quad (3.6)$$

$$I_{satmin} \leq I_{sat} \leq I_{satmax} \quad (3.7)$$

$$I_{phmin} \leq I_{ph} \leq I_{phmax} \quad (3.8)$$

Algorithm 2 describes the pseudocode of the GA employed.

---

**Algorithm 2** Pseudocode of GA applied to PV cell parameter estimation.

---

**INPUT:** Experimental  $I - V$  data,  $p$ ,  $itermax$ , search ranges

**OUTPUT:**  $\varphi$  iter=1

1. Generate initial population
  2. Evaluate the fitness function and constrains
  3. Select the best solution
  4. **While**  $iter = 2 : itermax$ 
    - 4.1 **For**  $i = 1 : p$  Select  $r$  vectors of initial population  
Create  $p - r$  vectors randomly  
Generate the new population combining selected and created vectors  
Select two parents randomly from the new population  
Create offspring by recombining parents  
Mutate offspring  
Select the best offspring
    - 4.2 **End For** Generate offspring population  
Evaluate fitness function and constrains  
New population= [initial population; offspring population]  
Initial population= the best p solution vectors  
Select the best solution  $\varphi$
  5. **End While**
- 

### 3.3. P-V CURVE CALCULATION USING $\delta$ PARAMETER

After evaluating the parameters estimated by the GA and comparing the P-V curves obtained with the experimental data, a small error was detected between the data as Figures 3.1b, 3.2b, and 3.3b show. Then to adjust

the estimation of the parameters, it was necessary to perform an additional algorithm in which the values of  $R_s$  and  $R_{sh}$  were modified in an iterative cycle since they are the parameters which correspond to the degradation modes explained in Section 1.3. The algorithm evaluates the equation 3.1 with the 5 parameters with the Newton-Raphson method as it was explained previously, this taking into account the iterative loop for  $R_s$  using values from  $0.1\Omega$  to  $0.5\Omega$  and for  $R_{sh}$  values from  $10\Omega$  to  $50\Omega$  [7–9]. The additional value found by the algorithm to fit the P-V curve was named  $\delta_{R_s}$  and  $\delta_{R_{sh}}$ . In each evaluation of equation 3.1 the following was considered: perform a subtraction between the value of  $R_s$  inside the loop and  $\delta_{R_s}$  (i.e.,  $R_s - \delta_{R_s}$ ) and perform an add between the value of  $R_{sh}$  inside the loop and  $\delta_{R_{sh}}$  (i.e.,  $R_{sh} + \delta_{R_{sh}}$ ), this for the three PV panels. The parameter  $\delta$  might be considered as an auxiliary value for evaluating degradation in PV panels. Table 3.1 shows the values of the 5 parameters and the corresponding  $\delta$  values for each PV panel under study. The tests were executed using MATLAB/Simulink software on a computer with an Intel(R) Xeon(R)CPU E5-2667@2.90 GHz 2.90 GHz (dual processor), 48 GB RAM, and Windows 10 PRO.

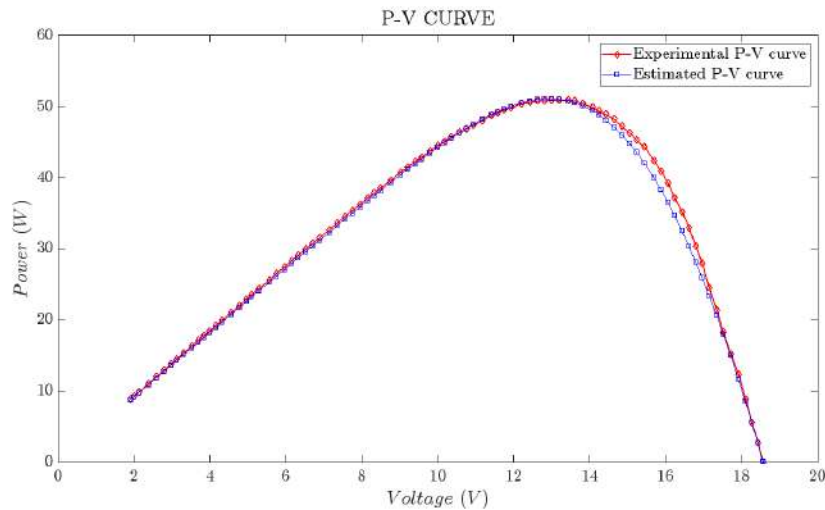
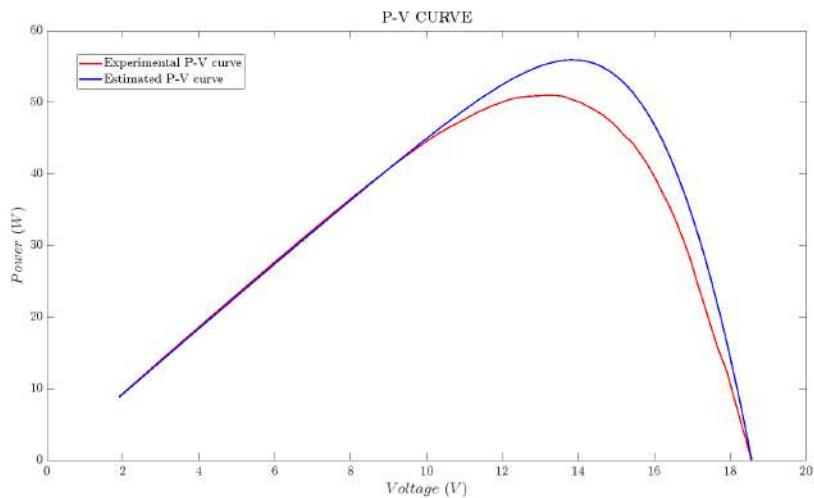
(a) P-V curve with  $\delta$ (b) P-V curve without  $\delta$ 

Figure 3.1: Parameter estimation for Hybrytec qm5-85/12 solar panel

From Figures 3.1a, 3.2a and 3.3a it can be seen how the  $\delta$  values improve the parameter estimation of the PV panels. Considering that these PV panels present some degradation especially aging, this correction parameter

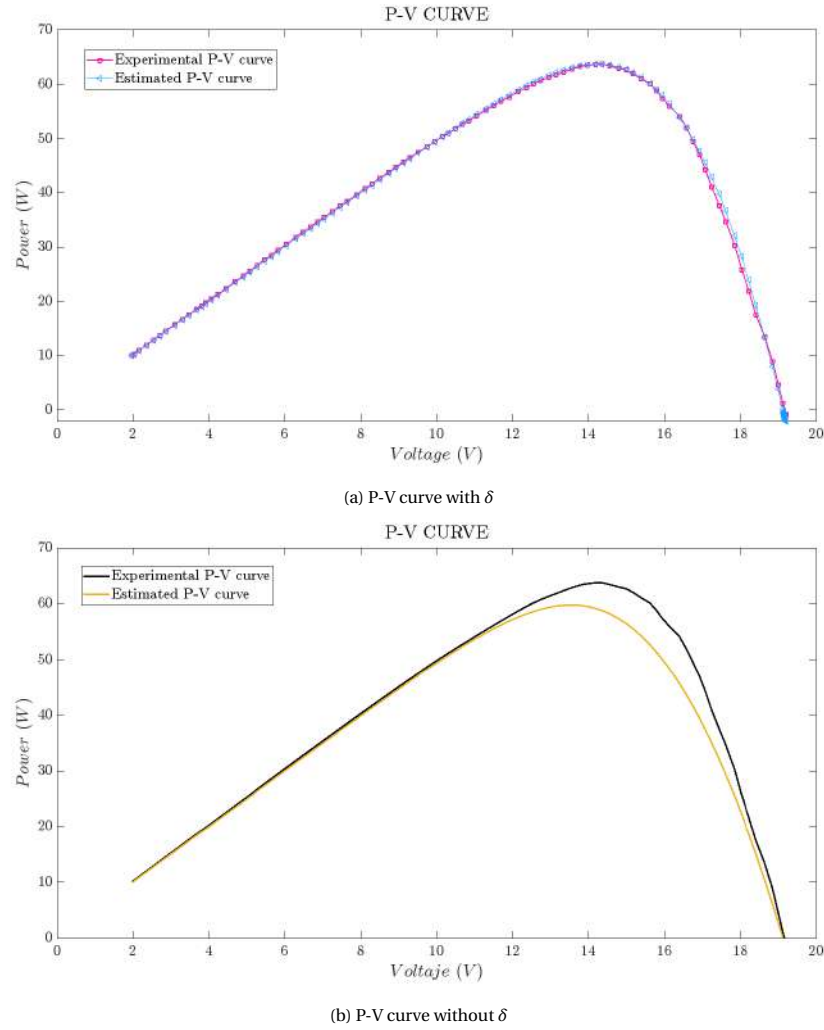


Figure 3.2: Parameter estimation for SP090 solar panel

allows quantifying the level of degradation in terms of  $R_s$  and  $R_{sh}$  [10].

### 3.3.1. ANALYTICAL TECHNIQUE FOR IDEAL PV PARAMETERS

As it was stated previously, GA and an analytical technique were used to estimate the parameters of the PV panels under study, with GA the parameter estimation was for the P-V curves obtained experimentally, and the analytical method for calculating the parameters from the datasheet values. Such a process was carried out to make a fair comparison between the ideal or without degradation values and the PV data obtained from the PV panels with degradation.

According to the procedure described in [11], it is necessary first, to calculate  $\eta$  with equation (3.9):

$$\eta = \frac{\alpha_v - \frac{V_{OC,STC}}{T_{STC}}}{N_s \cdot V_{t,STC} \cdot \left( \frac{\alpha_i}{I_{ph,STC}} - \frac{3}{T_{STC}} - \frac{E_{gap}}{k \cdot T_{STC}^2} \right)} \quad (3.9)$$

Where  $\alpha_v$  is the voltage temperature coefficient,  $V_{OC,STC}$  is the voltage in open circuit conditions,  $\alpha_i$  is the current temperature coefficient,  $E_{gap}$  is the energy gap established as  $1.8 \cdot 10^{-19}$ .

In order to calculate  $I_{sat}$ , the open circuit conditions can be used as well, using equation (3.10):

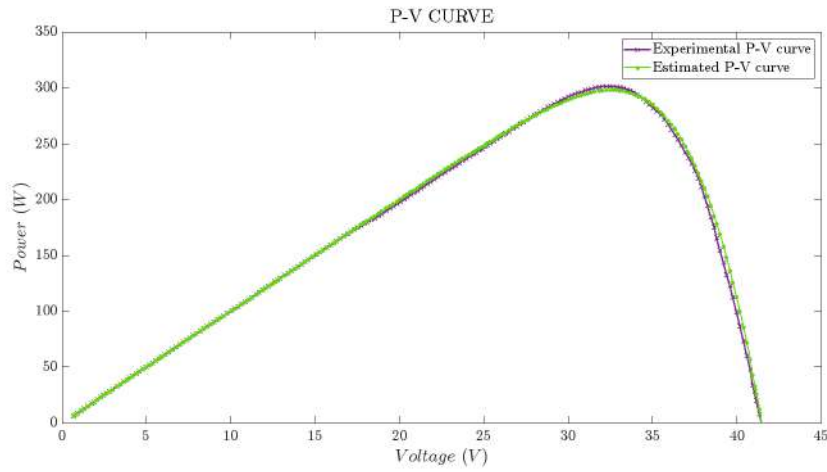
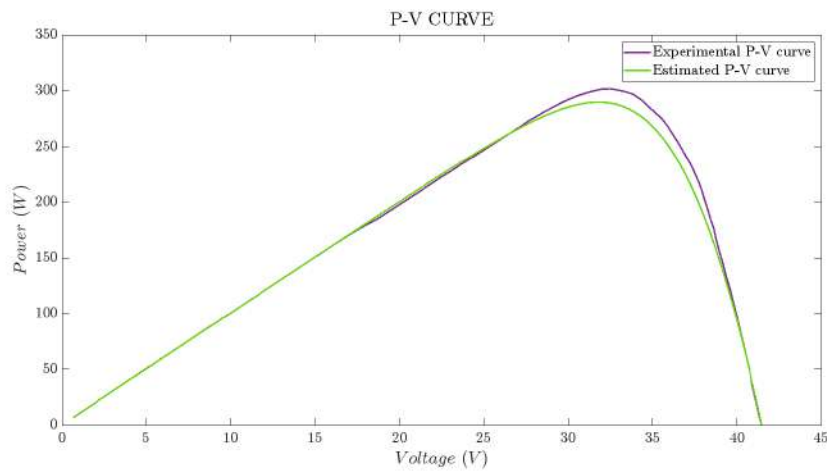
(a) P-V curve with  $\delta$ (b) P-V curve without  $\delta$ 

Figure 3.3: Parameter estimation for JKM400M-72H-V solar panel

$$I_{sat,STC} \approx I_{ph,STC} \cdot e^{-\frac{V_{OC,STC}}{\eta \cdot N_s \cdot V_t,STC}} \quad (3.10)$$

Where  $V_{t,STC}$  is the thermal voltage and it is described as follows:

$$V_t = \frac{k \cdot T}{q} \quad (3.11)$$

With  $k = 1.3806503 \cdot 10^{-23}$  J/K is the Boltzmann constant,  $q = 1.60217646 \cdot 10^{-19}$  C is the electron charge and T is the junction temperature, which  $T_{STC} = 25^\circ\text{C}$ .

The temperature coefficient C can be evaluated and  $I_{sat}$  can be calculated according to the value of the temperature T with equation (3.12).

$$C = \frac{I_{sat,STC}}{T_{STC}^3 \cdot e^{-\frac{E_{gap}}{k \cdot T_{STC}}}} \quad (3.12)$$

For the resistors  $R_s$  and  $R_{sh}$  calculations is necessary a change of variable as equation (3.13) shows.

Hybrytec qm5-85/12			
Parameters	Parameters estimated	Parameters adjusted	$\delta$
$\eta$	1.415	-	-
$R_s[\Omega]$	0.3598	0.6598	0.3
$R_{sh}[\Omega]$	101.335	101.235	0.1
$I_{sat}[A]$	$9.9541 \cdot 10^{-6}$	-	-
$I_{ph}[A]$	4.64	-	-
Solar plus S090			
Parameters	Parameters estimated	Parameters adjusted	$\delta$
$\eta$	1.4411	-	-
$R_s[\Omega]$	0.3554	0.5554	0.2
$R_{sh}[\Omega]$	785.9382	785.6382	0.3
$I_{sat}[A]$	$9.5699 \cdot 10^{-6}$	-	-
$I_{ph}[A]$	5.01	-	-
JKM400M-72H-V			
Parameters	Parameters estimated	Parameters adjusted	$\delta$
$\eta$	0.7084	-	-
$R_s[\Omega]$	0.20303	0.30303	0.1
$R_{sh}[\Omega]$	395.0934	-	-
$I_{sat}[A]$	$4.9637 \cdot 10^{-6}$	-	-
$I_{ph}[A]$	10.09	-	-

Table 3.1: Results of parameter estimation for the PV panels under study

$$x = \frac{V_{MPP} + R_s \cdot I_{MPP}}{N_s \eta V_t} \quad (3.13)$$

Where  $V_{MPP}$  and  $I_{MPP}$  are the voltage and current in the maximum power point (MPP) respectively.  $N_s$  stands for the number of cells in series connection.

Then,  $R_s$  can be expressed as equation (3.14):

$$R_s = \frac{x N_s \eta V_t - V_{MPP}}{I_{MPP}} \quad (3.14)$$

With help of equation (3.13) it is possible to express  $R_{sh}$  with equations (3.15) and (3.16):

$$R_{sh} = \frac{V_{MPP} + I_{MPP} \cdot R_s}{I_{ph} - I_{MPP} - I_{sat} \cdot \left( e^{\frac{V_{MPP} + I_{MPP} \cdot R_s}{N_s \eta V_t}} - 1 \right)} \quad (3.15)$$

$$R_{sh} = \frac{x N_s \eta V_t}{I_{ph} - I_{MPP} - I_{sat} \cdot (e^x - 1)} \quad (3.16)$$

Considering the MPP conditions, it results in equations (3.17) and (3.18):

$$\left. \frac{\partial(V \cdot I)}{\partial V} \right|_{MPP} = 0 \rightarrow I_{MPP} + V_{MPP} \cdot \left. \frac{\partial I}{\partial V} \right|_{MPP} = 0 \quad (3.17)$$

$$\left. \frac{\partial I}{\partial V} \right|_{MPP} = - \frac{\frac{1}{R_p} + \frac{I_{sat}}{N_s \eta V_t} \cdot e^{\frac{V_{MPP} + I_{MPP} \cdot R_s}{N_s \eta V_t}}}{1 + \frac{R_s}{R_p} + \frac{R_s \cdot I_{sat}}{N_s \eta V_t} \cdot e^{\frac{V_{MPP} + I_{MPP} \cdot R_s}{N_s \eta V_t}}} \quad (3.18)$$

Then, replacing equation (3.18) in (3.17), it can be obtained equation (3.19):

$$I_{MPP} - V_{MPP} \cdot \frac{\frac{1}{R_p} + \frac{I_{sat}}{N_s \eta V_t} \cdot e^{\frac{V_{MPP} + I_{MPP} R_s}{N_s \eta V_t}}}{1 + \frac{R_s}{R_p} + \frac{R_s \cdot I_{sat}}{N_s \eta V_t} \cdot e^{\frac{V_{MPP} + I_{MPP} R_s}{N_s \eta V_t}}} = 0 \quad (3.19)$$

For the solution of the non-linear equation, Lambert W function is employed as follows:

$$x = W \left[ \frac{V_{MPP} (2I_{MPP} - I_{ph}) e^{\frac{V_{MPP}(V_{MPP} - 2N_s \eta V_t)}{N_s \eta^2 V_t^2}}}{N_s \eta I_{sat} V_t} \right] + 2 \frac{V_{MPP}}{N_s \eta V_t} - \frac{V_{MPP}^2}{N_s \eta^2 V_t^2} \quad (3.20)$$

Using the equation previously described, the parameters  $I_{ph}$ ,  $I_{sat}$ ,  $\eta$ ,  $R_s$ ,  $R_{sh}$  are calculated.

To construct the P-V profile, the 5 parameters are replaced in equation (3.1), and the value of  $N_s$  and  $N_p$  depends on the PV panel, for solar plus S090 and hybrytec qm5-85/12 PV panels  $N_s=36$  and  $N_p=1$ , while for the JKM400M-72H-V PV panel  $N_s=24$  and  $N_p=6$ . This evaluation is performed in a loop from 1 until  $V_{oc}$  value to calculate the current point for each voltage point.

### 3.3.2. GRAPHICAL INTERFACE FOR USERS

An application for PV array sizing was developed. The GUIDE was developed in *Python* with several PV panel power options (4 types of PV panels) and two PV array calculation options, that is, taking into account the available installation area or considering the amount of energy to be supplied with the PV array. The results given by the GUIDE are: PV panel efficiency, energy delivered by day by the PV array, number of PV panels required (according to the energy required) and, the area occupied by these PV panels. This GUIDE has the option of exporting the obtained data to a txt file when finished the calculation of the PV array designed by the user. There is also a basic guide on how to download the solar radiation data from the NREL and IDEAM web pages, as well as the elements and values to be taken into account to continue with the calculations of the storage system. This interface functions as a basis for microgrid calculations: you can perform the calculations for the PV with the GUIDE, and provide a basis for the storage system (e.g. choose the proper inverter, battery bank, DC bus). The full description of the GUIDE can be found in the appendix section (A).

In the next chapter, the results of these evaluations will be illustrated and analyzed for each case of study.

## BIBLIOGRAPHY

- [1] Giovanni Petrone, Carlos Andrés Ramos-Paja, and Giovanni Spagnuolo. *Photovoltaic sources modeling*. John Wiley & Sons, 2017.
- [2] Tong Kang, Jiangang Yao, Min Jin, Shengjie Yang, and ThanhLong Duong. A novel improved cuckoo search algorithm for parameter estimation of photovoltaic (pv) models. *Energies*, 11(5), 2018.
- [3] A. Trejos Grisales, A. Osorio Giraldo, D. Gonzalez Montoya, M. Durango Florez, and J. D. Bastidas Rodríguez. Análisis del comportamiento de arreglos fotovoltaicos con degradación operando bajo condiciones de sombreado parcial. *Revista EIA*, 17(22):1–110, 2020.
- [4] Juan David Bastidas-Rodriguez, Luz Adriana Trejos-Grisales, D. Gonzalez-Montoya, Carlos Andrés Ramos-Paja, G Petrone, and G Spagnuolo. General modeling procedure for photovoltaic arrays. *Electric Power Systems Research. Journal of Renewable and Sustainable Energy*, 155:67–79, 2018.
- [5] Chapra C. S. *Métodos Numéricos Para Ingenieros*. McGraw Hill, MTufts University, 5 edition, 2007.
- [6] J.D. Bastidas-Rodriguez, G. Petrone, C.A. Ramos-Paja, and G. Spagnuolo. A genetic algorithm for identifying the single diode model parameters of a photovoltaic panel. *Mathematics and Computers in Simulation*, 131:38–54, 2017. 11th International Conference on Modeling and Simulation of Electric Machines, Converters and Systems.
- [7] Jhoan Sebastian Parra Quiroga. Procedure for detection of potential-induced degradation in photovoltaic panels when they are part of a photovoltaic system. Master's thesis, School of Electrical and Electronics Engineering. Universidad del Valle, June 2020.
- [8] F.J. Sánchez-Pacheco, J.R. Heredia-Larrubia, G. Petrone, and M. Sidrach-de Cardona. Pv panels parasitic resistance degradation estimation by means of the mppt controller modified operation: the m-factor calculation. *Electronics Letters*, 56(22):1194–1197, 2020.
- [9] Jialei Su, Yunpeng Zhang, Chen Zhang, Tingkun Gu, and Ming Yang. Parameter extraction of photovoltaic single-diode model using integrated current-voltage error criterion. *Journal of Renewable and Sustainable Energy*, 12(4):043704, 2020.
- [10] J.D. Bastidas-Rodriguez, E. Franco, G. Petrone, C.A. Ramos-Paja, and G. Spagnuolo. Quantification of photovoltaic module degradation using model based indicators. *Mathematics and Computers in Simulation*, 131:101–113, 2017. 11th International Conference on Modeling and Simulation of Electric Machines, Converters and Systems.
- [11] J. Accarino, G. Petrone, C. A. Ramos-Paja, and G. Spagnuolo. Symbolic algebra for the calculation of the series and parallel resistances in pv module model. In *2013 International Conference on Clean Electrical Power (ICCEP)*, pages 62–66, 2013.



# 4

## EXPERIMENTAL TESTS AND RESULTS

### 4.1. INTRODUCTION

This chapter details the workbench used and the results obtained from each experimental scenario considered in this work to analyze soiling. As stated in Chapter 3, the degradation modes considered are artificial soiling, cracking and corrosion which is present in SP090 PV panel, and advanced aging which is present in hybrytec qm5-85/12 PV panel. The cases studied in this work are random artificial soiling patterns for each PV panel. Then, it is necessary to compare the MPP of the PV panel without any shadow or degradation (i.e ideal) with the one obtained experimentally (i.e real). Using fill factor (FF) [1] and the loss power percentage as a measure for the difference in the delivered power it is possible to quantify the loss power.

### 4.2. EXPERIMENTAL TEST PLATFORM

For the experimental tests, two scenarios were employed: one clean PV panel, that is without an artificial soiling condition, and one panel with an artificial soiling condition on it to compare the delivered power by each panel to quantify the losses.

The experimental platform to perform the acquisition of the I-V curves of the solar panel under study is formed by:

- Two electronic loads BK precision 8514
- One oscilloscope tektronix MDO 3024
- One oscilloscope ROHDE&SCHWARZ RTE1204
- Two solar panels 90W solar plus S090 poly-crystalline
- Two solar panels 85W hybrytec qm5-85/12 mono-crystalline
- One solar panel 400W JKM400M-72H-V half cell

Table 4.1 describes the datasheet data of the PV panels worked.

Data	solar plus S090	hybrytec qm5-85/12	JKM400M-72H-V
$P_{max}$ [W]	90	85	400
$I_{mpp}$ [A]	5	4.81	9.60
$V_{mpp}$ [V]	18	17.84	41.7
$I_{sc}$ [A]	5.410	5.17	10.61
$V_{oc}$ [V]	22.50	21.74	49.8

Table 4.1: Datasheet values for the PV panels

Figure 4.1 illustrates the scheme of the experimental setup, and the connection is shown in Figure 4.2. The electronic load was programmed to perform a voltage sweep to the PV panels, starting at 0.1.V and finishing in the corresponding value of  $V_{oc}$  for each PV panel. The oscilloscope works as an acquisition and visualization tool for the voltage and current data to be processed finally in Matlab software on a computer.

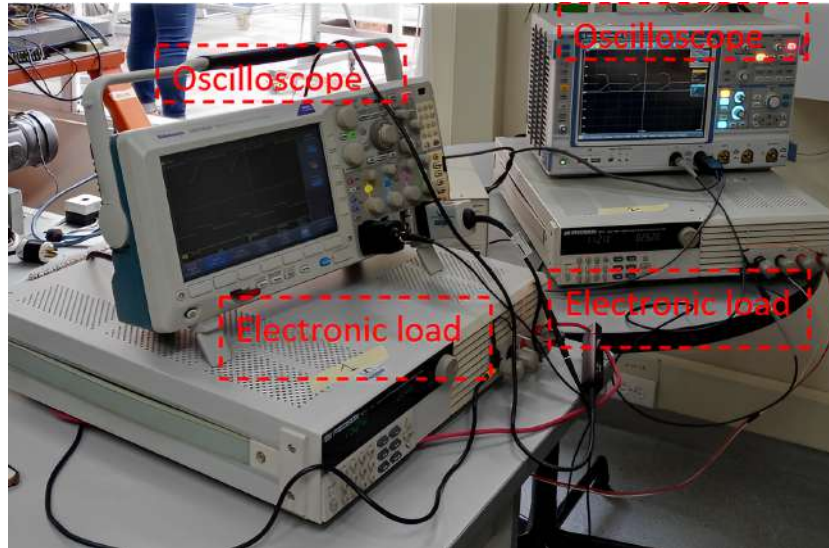


Figure 4.1: Experimental setup

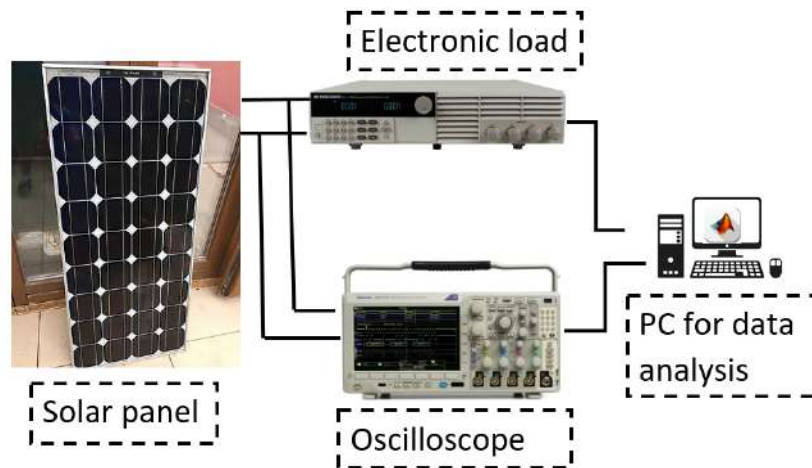


Figure 4.2: Connection scheme of the experimental setup

Figures 4.3a and 4.3b shows the first case of study employed: two solar panels 85W hybrytec qm5-85/12 where Figure 4.3a is the clean panel and Figure 4.3b is the dirty panel, simulating soiling conditions. All the experimental tests were performed with solar radiation of  $1000/m^2$  and a measured temperature of  $43^\circ$ .



(a) First Test

(b) Second Test

Figure 4.3: Experimental test for hybrytec qm5-85/12 PV panel

The hybrytec qm5-85/12 PV panel has a considerable aging, then it presents aging in addition to the artificial soiling of Figure. 4.3b.



(a) Third Test

(b) Fourth Test

Figure 4.4: Experimental test for 90W solar panel

The SP090 solar panel besides presenting artificial soiling, as Figures 4.4a, 4.4b presents cracking and corrosion as Figures 4.5a, 4.5b.

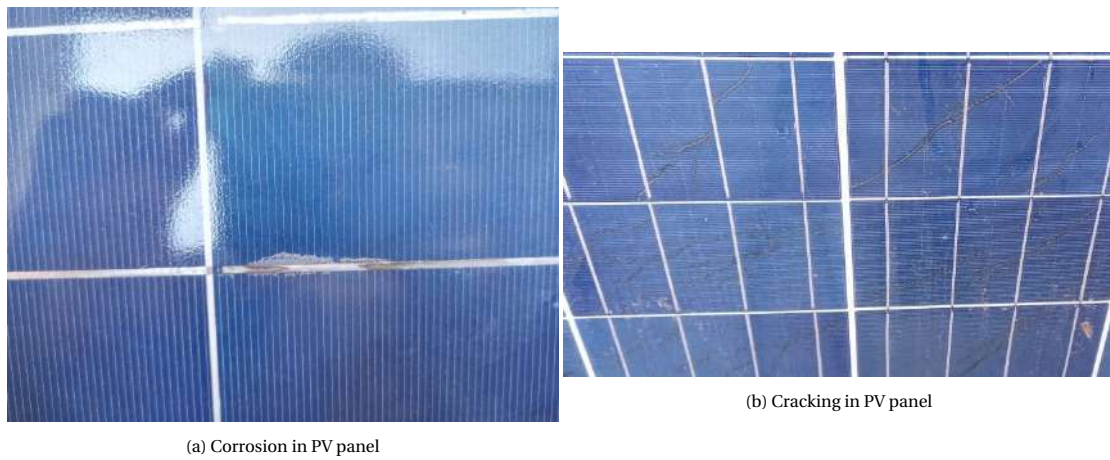


Figure 4.5: Faults present in 90W solar panel



Figure 4.6: Experimental test for JKM400M-72H-V solar panel

The JKM400M-72H-V PV panel is a PV panel with no faults, in this case, the only fault is the artificial soiling.

In the next section, the P-V curves obtained with these test scenarios will be presented and compared with the P-V curve obtained with the analytical procedure mentioned in section 3.3.1. To present the power losses and the performance metrics and quantify the impact of the soiling patterns in the generated power.

### 4.3. SOILING IMPACT ON PV PANELS

Two PV profiles were obtained for each experimental test corresponding to Figures 4.3a, 4.4a and 4.6 but without the soiling condition: the PV profile considered as ideal, that is, with no faults, which might correspond to the profile of a new PV panel without soiling, cracking, aging or corrosion.

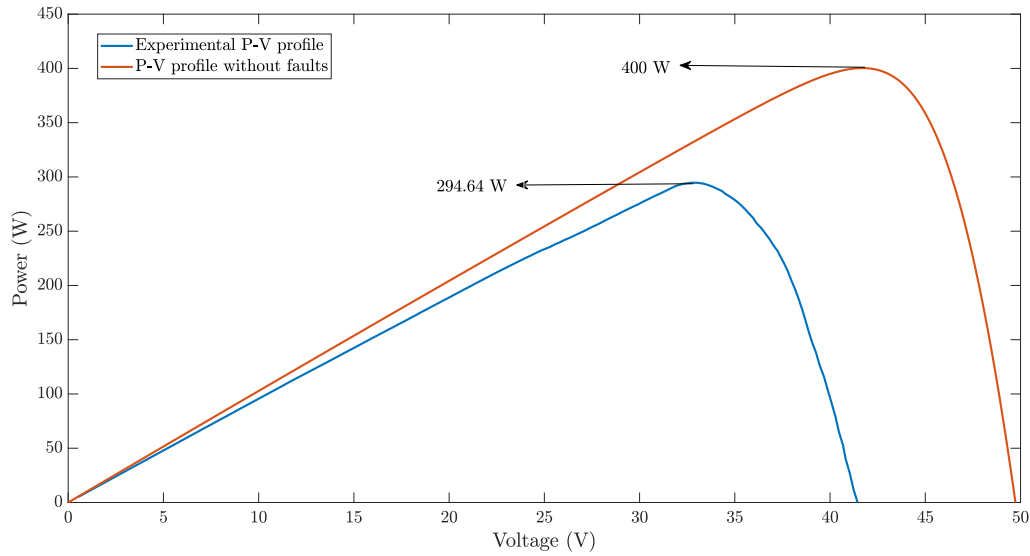


Figure 4.7: P-V curve of JKM400M-72H-V panel

Figure 4.7 shows the P-V curves of JKM400M-72H-V panel without faults (orange curve) obtained with the analytical technique in section 3.3.1 and the P-V curve obtained experimentally without soiling (blue curve). It is evident that the curve without faults (soiling) exhibits a higher MPP than the curve with soiling.

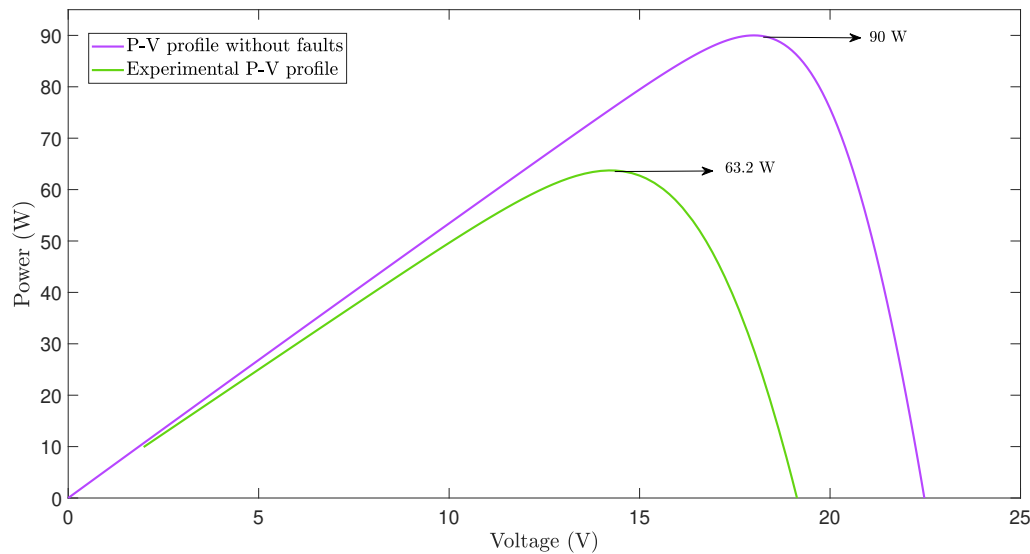


Figure 4.8: P-V curve of SP090 panel

Figure 4.8 shows the drop in the power delivered due to cracking and corrosion in the SP090 panel which are present in the PV panel. The purple curve is the curve without faults obtained with the analytical technique and the green curve was obtained experimentally without soiling.

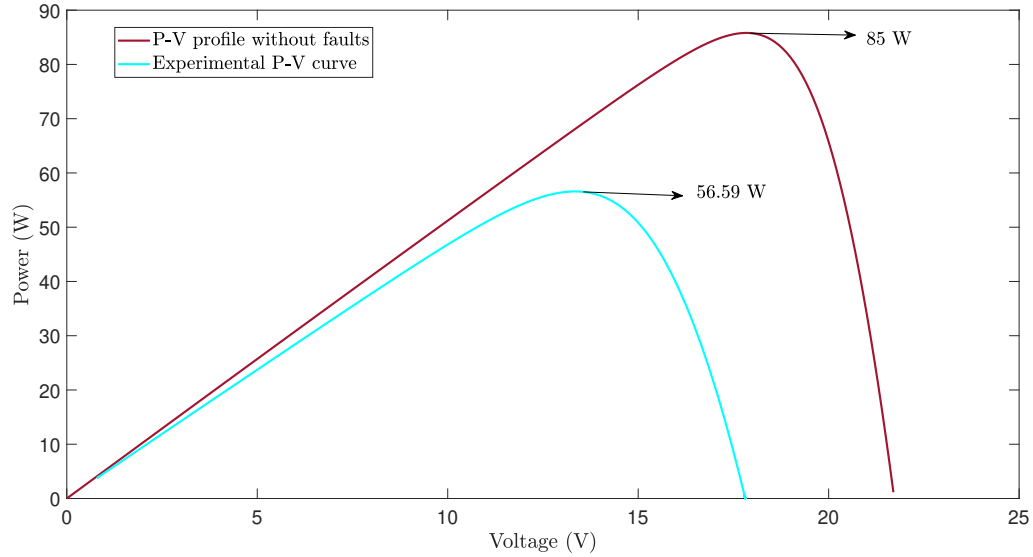


Figure 4.9: P-V curve of hybrytec qm5-85/12 panel

Figure 4.9 shows the MPP difference between the P-V curves of the hybrytec qm5-85/12 panel, this drop is caused by the aging present in this PV panel. The red curve is the curve without faults obtained with the analytical technique and the aquamarine blue curve was obtained experimentally without soiling.

It is important to highlight the drop in  $V_{oc}$  in Figures 4.7, 4.8 and 4.9, as it was presented in chapter 1 this might be due to aging and corrosion.

Based on Figures 4.7, 4.8 and 4.9 and, applying equations (4.1), (4.4) and (4.3), the FF and the loss power percentage can be calculated for each test scenario. Table 4.2 shows the results for the power quantification.

$$FF_{full} = \frac{P_{max,ideal}}{V_{oc,ideal} \times I_{sc,ideal}} \quad (4.1)$$

$$FF_{REAL} = \frac{P_{max,real}}{V_{oc,real} \times I_{sc,real}} \quad (4.2)$$

$$Losspower = \left( \frac{P_{real} \times 100}{P_{full}} \right) - 100 \quad (4.3)$$

Table 4.2: FF percentage loss.

	SP090	Hybrytec qm5-85/12	JKM400M-72H-V
$FF_{full}$	0.74	0.75	0.77
$FF_{REAL}$	0.66	0.66	0.69
Loss power (%)	29.77	33.42	26.34

According to data in Table 4.2, the FF decrease a 10.81% in SP090 panel, a 12% in hybrytec qm5-85/12 panel, and 10.38% in JKM400M-72H-V panel regarding the value of a new PV panel. This drop in FF is related to aging and cracking in hybrytec qm5-85/12 and SP090 PV panels, and the exposure time in the JKM400M-72H-V PV panel since this data corresponds to the test without soiling. As it is also explained in Table 4.2, the highest power drop was presented in Hybrytec qm5-85/12 panel, which corresponds to the state of the PV panel.

To analyze the impact of artificial soiling considering the P-V curves for the scenarios of section 4.2 (i.e Figures 4.10, 4.11 and 4.12) some performance metrics such as FF and the percentage of loss power ( $Losspower_x(\%)$ ) area used between the P-V curves of the panels with soiling and without soiling. It is important to highlight that besides the artificial soiling scenarios there exists aging in hybrytec qm5-85/12 panel, cracking, and corrosion in SP090 panel.

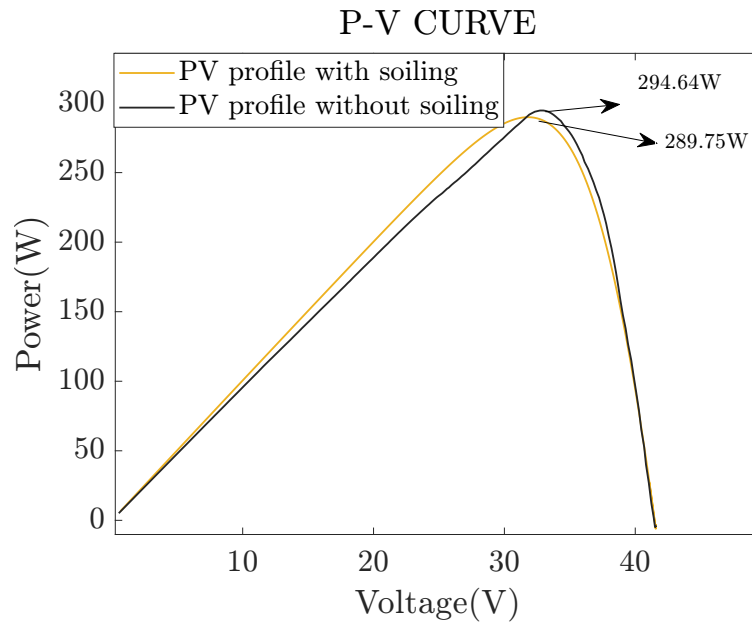


Figure 4.10: P-V curves of JKM400M-72H-V panel with and without soiling

Figure 4.10 shows the P-V curves for JKM400M-72H-V panel with and without artificial soiling. This PV panel does not present another type of degradation, then the power drop is due to soiling. The P-V curve with soiling does not show any deformation from the P-V curve without soiling..

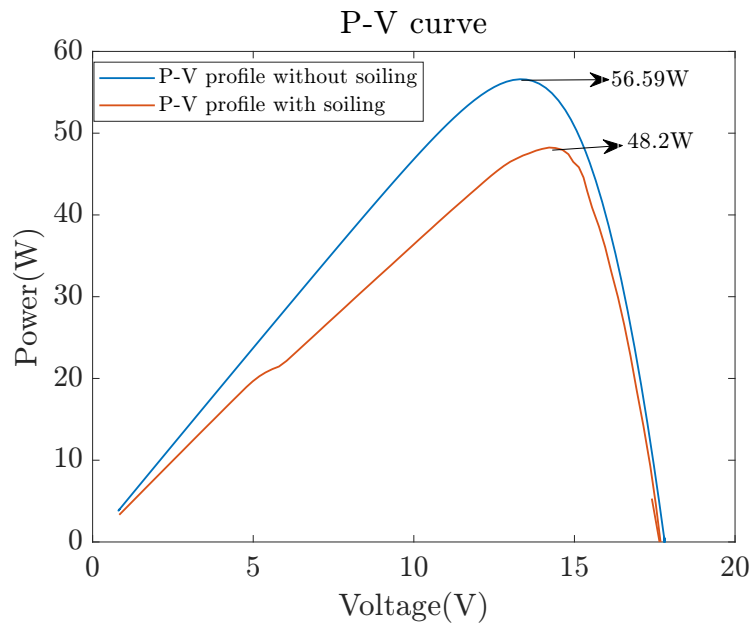


Figure 4.11: P-V curves of hybrytec qm5-85/12 panel with and without soiling

Figure 4.11 shows the P-V curves of hybrytec qm5-85/12 considering that this panel is under the artificial soiling condition and aging. It can be seen a small deformation around the MPP and an inflection point due to the soiling scenario used being compared with the PV panel without soiling. Additionally, it shows as well a larger power drop than the half-cell technology.

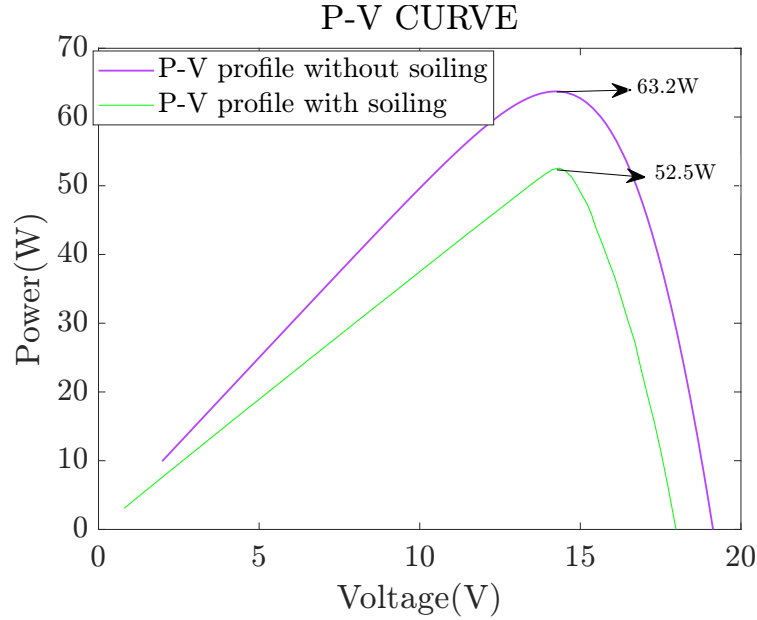


Figure 4.12: P-V curves of S090 panel with and without soiling

Figure 4.12 shows the P-V curves of SP090 considering that the panel with artificial soiling also has corrosion, and cracking. The P-V curve with artificial soiling shows a deformation in the MPP and the slope near the  $V_{oc}$  zone according to the corrosion and soiling effect in the P-V curve.

For the case of hybrytec qm5-85/12 panel, since there is an inflection point, which means that, one of the bypass diodes of the PV panel got activated, it is more notable that this type of degradation is similar to partial shading on the PV panel. According to this information, there exists one global maximum power point (GMPP) and one local maximum power point (LMPP) then the expression applied to calculate the FF considering the GMPP is described in equation (4.4):

$$FF_{shade} = \frac{GMPP}{V_{oc} \times I_{sc}} \quad (4.4)$$

Table 4.3 shows the performance metrics (FF and power loss percentage) based on the data of Table 4.2, where  $Powerloss_{real}$  corresponds to the computation of the power obtained experimentally without the artificial soiling condition and,  $Powerloss_{ideal}$  corresponds to the ideal values, i.e., the power of the PV panel without faults.

Table 4.3: FF loss percentage

	Solar plus S090	Hybrytec qm5-85/12	JKM400M-72H-V
$FF$	0.431	0.43	0.55
$Powerloss_{real}$ (%)	16.82	14.9	1.64
$Powerloss_{ideal}$ (%)	41.58	43.24	27.55

According to Table 4.3 as it is expected there is a higher power drop, for S090 panel is 16.82% higher than the power marked in Figure 4.8, for Hybrytec qm5-85/12 panel is 14.9% higher than the power marked in Figure 4.9



and for JKM400M-72H-V panel is 1.64% higher than the power marked in Figure 4.7. The artificial soiling produces a 41.58% power drop in the S090 PV panel considered as new and without faults or shading, for Hybrytec qm5-85/12 it can be quantify a power loss of 43.24% and for JKM400M-72H-V a power loss of 27.55%.

It is important to highlight that the half cell technology for this experimental tests is the type of technology with less power drop under the scenarios studied [2, 3], followed by poly-crystalline and lastly mono-crystalline.

## BIBLIOGRAPHY

- [1] D. Prince Winston, G. Karthikeyan, M. Pravin, O. JebaSingh, A.G. Akash, S. Nithish, and S. Kabilan. Parallel power extraction technique for maximizing the output of solar pv array. *Solar Energy*, 213:102–117, 2021.
- [2] Jiadong Qian, Andrew Thomson, Andrew Blakers, and Marco Ernst. Comparison of half-cell and full-cell module hotspot-induced temperature by simulation. *IEEE Journal of Photovoltaics*, 8(3):834–839, 2018.
- [3] Zewei Yang, Kailin Liao, Jun Chen, Lei Xia, and Xuetao Luo. Output performance analysis and power optimization of different configurations half-cell modules under partial shading. *Optik*, 232:166499, 2021.

# 5

## CONCLUSIONS

From the literature review, it was possible to identify degradation aspects such as its different causes, detection methods, and measurement methodologies, with which it was possible to determine that this work will address mainly the aging and soiling, as well as cracking since the available panels in the university laboratory (Laboratorio de Electrónica y energías renovables) present these characteristics. As for the detection method, 3 main methods were identified: thermal image analysis, parameter estimation and I-V curve analysis. Considering the laboratory instruments and the expertise in parameter estimation and curve analysis, these were defined as the methods to be used in this work. The measurement methodology was the loss power percentage and fill factor, although this is not present in the classification.

In terms of the impact of different shading patterns, the most commonly used patterns in the literature are SN, LN, SW, and LW. To calculate their impact on the delivered power, experimental tests were performed by reproducing these patterns on each of the panels worked (i.e. mono-crystalline (hybrytec qm5-85/12), polycrystalline (solar plus S090), and half cell (JKM400M-72H-V)). The study demonstrated that the diagonal shading pattern generates the lower power loss with a FF of 0.807 and a percentage of lost power of 19.216% while the SN pattern generates the highest power loss with a FF of 0.65 and a percentage of lost power of 56.9%. These results can be used in PV system installation methodologies in order to avoid SN shading pattern which, according to the results obtained, has the highest impact.

Regarding the identification of the SDM parameters of the experimental I-V curve, it was shown that an adjustment in the parameters found is necessary, especially in  $R_s$  and  $R_{sh}$ , since as mentioned in chapter 1 these parameters are directly related to the types of degradation studied. The adjustment was performed by using a brute force approximation with a Newton-Raphson method by reducing the mismatch between the estimated and experimental P-V curves. The half-cell technology panel had the lowest fit, only having an additional value of 0.1  $\Omega$  in its  $R_s$ , while the polycrystalline and monocrystalline technologies had an additional value in both resistances: polycrystalline an additional value in  $R_s$  of 0.2 while for monocrystalline an additional value in  $R_s$  of 0.3.

Considering the test scenarios with cracking, corrosion, and aging, which were already present in SP090 and hybrytec qm5-85/12 PV panels respectively, a comparison was made between the P-V curves obtained experimentally without artificial soiling and the ideal P-V curves, i.e the curve obtained from a new PV panel or without any fault. The quantification of the power loss indicates that the SP090 and the hybrytec qm5-85/12 present a higher degradation (aging, hot-spot, cracking) than the half-cell technology, since the JKM400M-72H-V PV panel has the lowest power loss with 26.34%, the SP090 presents a power loss of 29.77% and the Hybrytec qm5-85/12 presents a power loss of 33.42%; These percentages are the result of comparing the fault P-V curve with the P-V curve obtained from the analytical methods when calculating the SDM parameters with the datasheet data with uniform solar radiation.

On the other hand, the quantification of power loss for the degradation test scenarios (i.e artificial soiling) also showed that the half-cell technology has the lowest power loss at 27.55%, this considering the power loss of the SP090 with 41.58% and for the hybrytec qm5-85/12 a power loss of 43.24%. In this way, the procedures proposed in this work allow versatility for the calculation of PV modeling and PV array sizing since it considers the major causes of power loss, i.e., shading and degradation, and how they affect each PV technology. The algorithms proposed in this work are thus a tool to analyze PV systems considering shading and degradation which are the effects that most affect energy production.

Partial shading and degradation are not comparable phenomena since they have different effects on the PV panels, however, this study indicates which type of phenomena should be considered when analyzing a PV array. In this work, with the results of power loss found with the different shading patterns and degradation modes, it is possible to prioritize in the analysis of the PV array which is the phenomenon that has more effect on the delivered power, and thus take actions and in case of occurrence seek methodologies to mitigate it.

**Future work:** From this work further studies on degradation modes. use and/or modify the PV sizing GUIDE made for agrovoltaic applications.

# A

## APPENDIXES

### A.1. PYTHON APP FOR PV ARRAY SIZING

Figure A.1 illustrates the main window of the sizing GUIDE. Figures A.2 and A.3 show respectively the secondary windows which correspond to the computation by area and by energy.

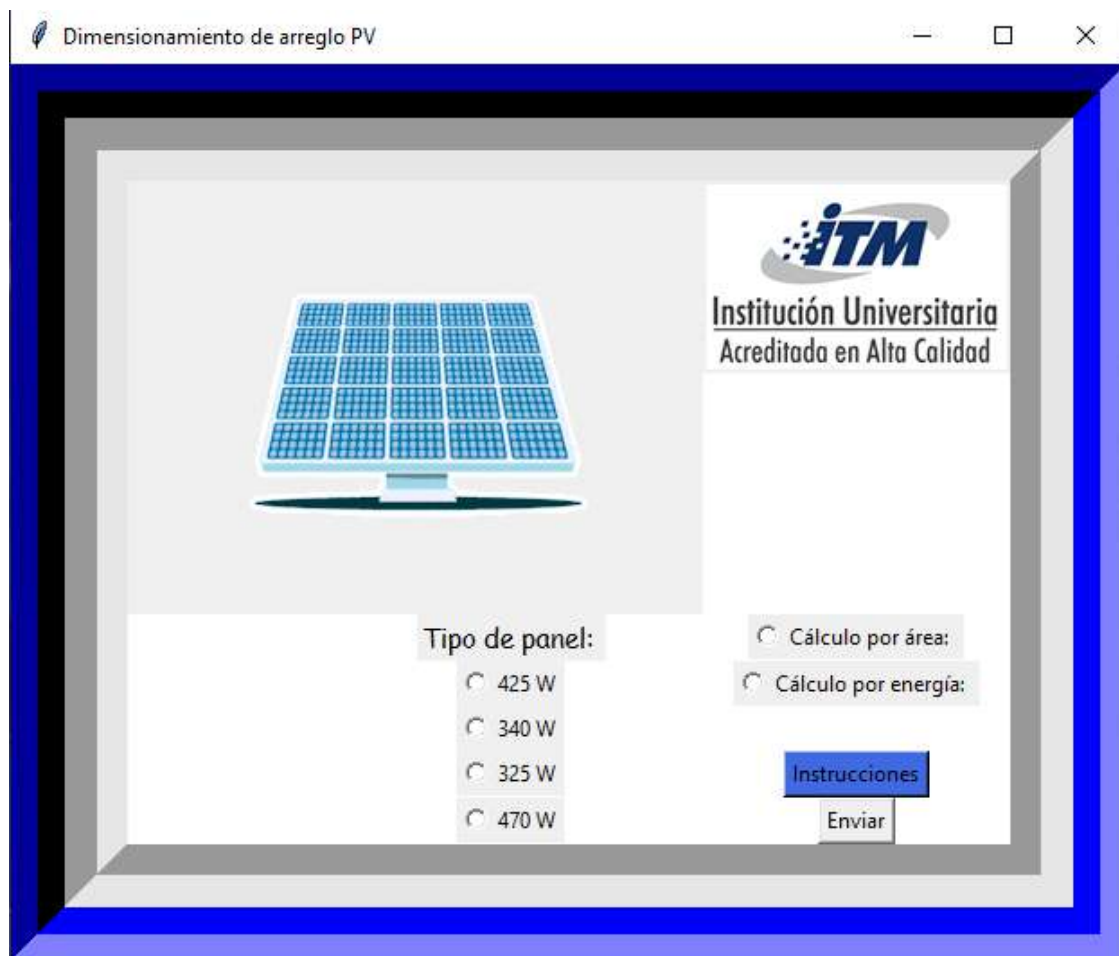


Figure A.1: Main window

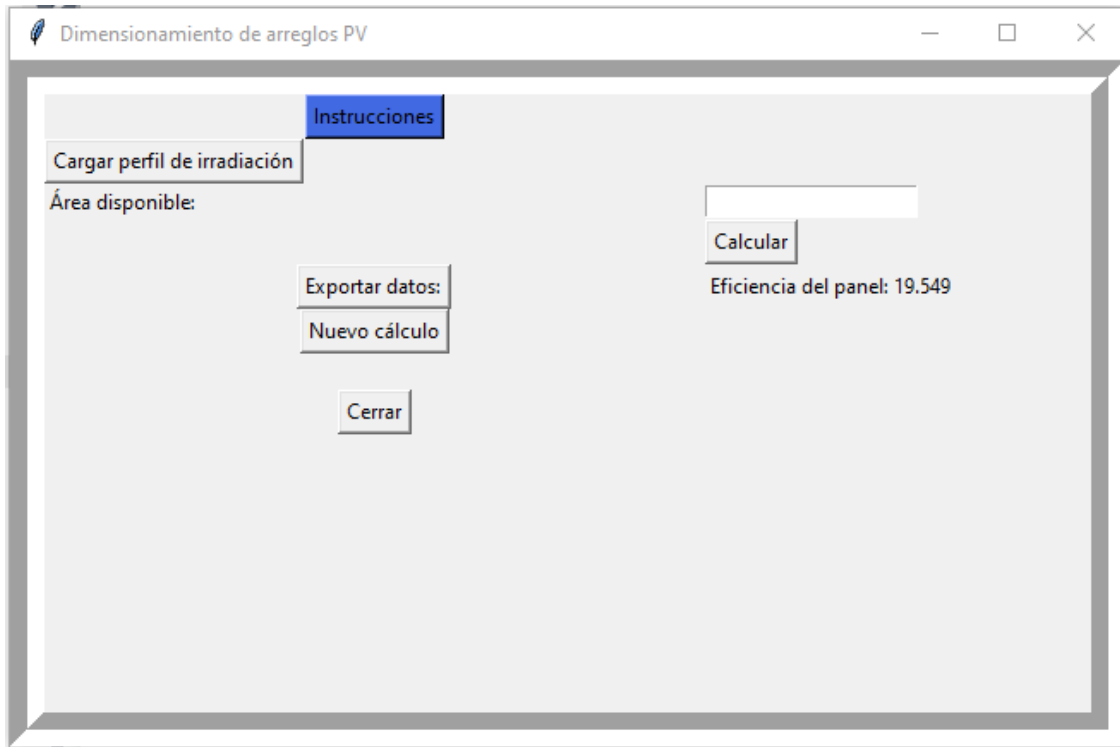


Figure A.2: Secondary window for computation by area

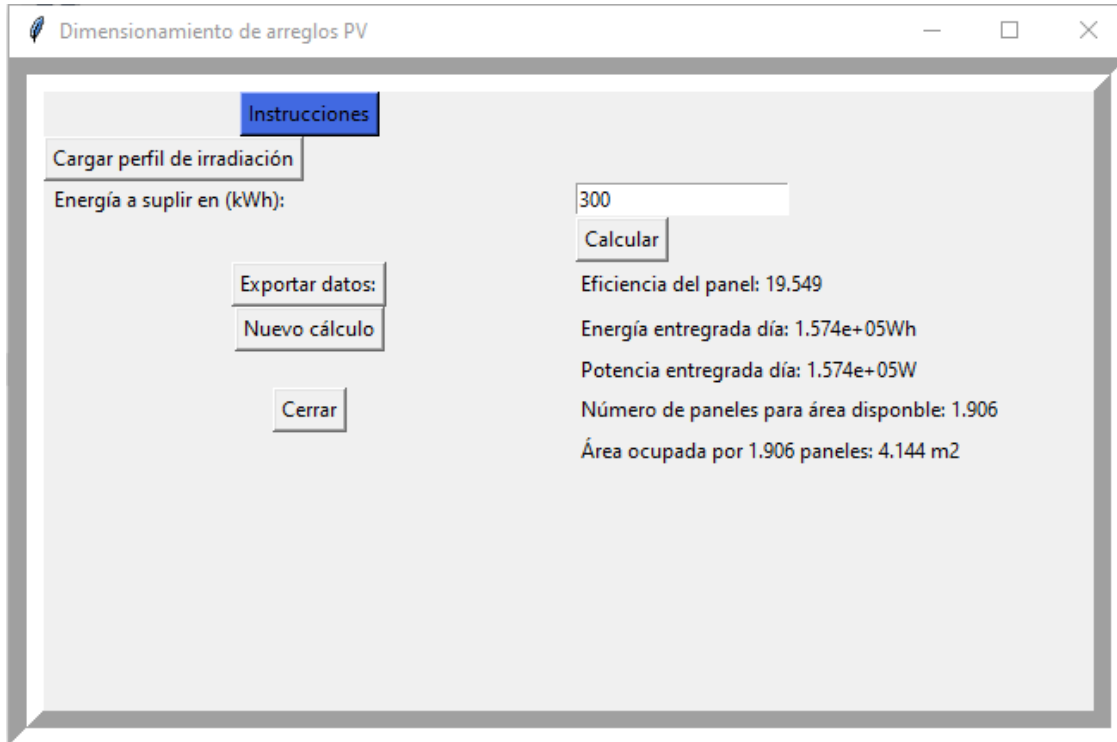


Figure A.3: Secondary window for computation by energy

### A.1.1.1. BUTTONS FUNCTIONALITY

Next will be described the function for every button and GUIDE window, for both the main window and the sub-window.

**Instructions for the GUIDE use:** This button deploys the instructions that is to say, the button in the main window deploys the next emergent window.

Instrucciones

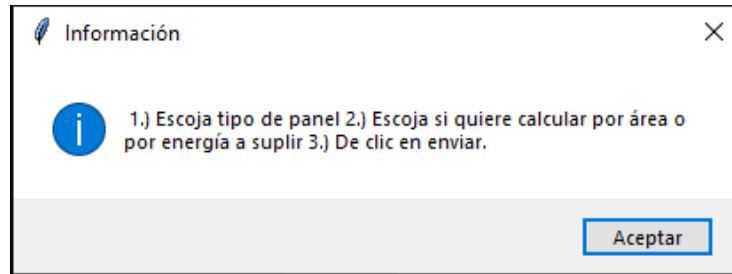


Figure A.4: Instructions for main window use

Figures A.5 and A.6 show respectively the secondary window case for the computation by area and by energy with the corresponding instructions.

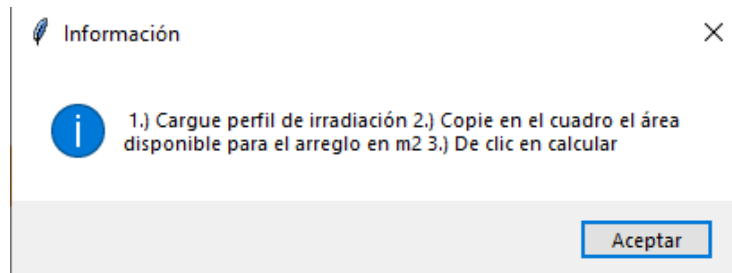


Figure A.5: Instructions for computation by area

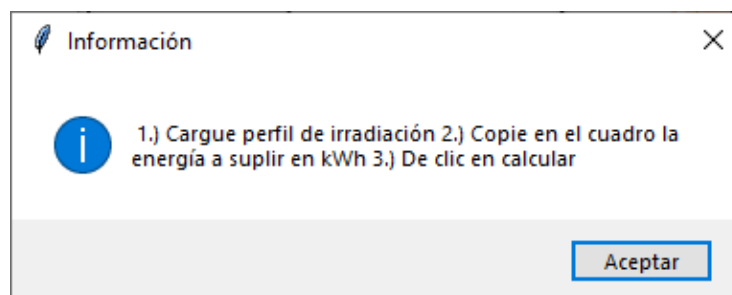


Figure A.6: Instructions for computation by energy to supply

**Computation options:** This checkbox shows the options available to perform the sizing computation of the PV array, the calculation by area is performed when the user has a data of area (in  $m^2$ ) to make the installation. On the other hand, the computation by energy is performed when the user has the data of the energy (in KWh)

- Cálculo por área:
- Cálculo por energía:



that needs to supply with the PV array. Each option will lead to a different secondary window, the data obtained will be explained further in the document.

Tipo de panel:

425 W

340 W

325 W

470 W

**Type of PV panel:** This checkbox shows the options of PV panels available for the sizing calculation categorized for their nominal power. Once the computation is already exported, the GUIDE shows the brand of the PV panel used. The procedure to export the data will be explained further.

Enviar

**Send button:** Clicking this button, the user enters to the secondary window depending on the data selected, that is to say, to perform the computation by area or by energy to supply.

Next buttons are in the secondary window for both choices.

Cargar perfil de irradiación

**Load the solar radiation profile:** This button allows to load the profile of the solar radiation of the installation zone, which must be in *.csv* format, and the data of 24 hours, that is to say, acquired every hour.

Calcular

**Compute:** This button allows to compute the area that the panels will fill, the energy these panels will supply and, the number of panels according to the option selected.

Exportar datos:

**Export data:** This button allows to save the computed data in a text file, the user needs to write the name of the file along with the *.txt* extension and search the location of the folder to save the data.

Nuevo cálculo

**New computation:** This button allows to perform a new computation, returns to the main window to start from scratch with a new PV sizing computation.

Cerrar

**Close:** With this button the user closes the app.

#### COMPUTATION BY AREA

Área disponible:

**Area available:** In this panel the available installation area is written in  $m^2$ .

After pushing the button **Calcular**, in this type of computation it can be obtained the following results:

- Efficiency of the chosen PV panel
- Power and energy delivered by day, according to the loaded solar radiation profile in W and Wh, respectively.
- Number of PV panels for the available area given by the user.
- Supplied energy by the computed PV array, in Wh.

## COMPUTATION BY ENERGY

Energía a suplir en (kWh):

**Energy to supply:** In this panel the amount of energy to be delivered by the PV array is written, this data must be given in kWh. .

After pushing the button **Calcular**, in this type of computation it can be obtained the following results:

- The efficiency of the chosen PV panel
- Power and energy delivered by day, according to the loaded solar radiation profile, in W and Wh, respectively.
- Number of panels for the computed available area according to the amount of energy given by the user.
- Occupied area by the PV panels computed by the GUIDE in  $m^2$ .

### A.1.2. PV ARRAY SIZING COMPUTATION

This section will show an example of the use of the app.

It is required to perform basic computing for a PV installation that generates 300kWh. The solar radiation profile of the area is shown in Fig. A.7, where the solar radiation data were acquired from 7:00 am until 18:00 pm. To start with the computation the PV panels chosen are **425 W** and the option **cálculo por energía**, next, the user click on **Enviar** button, as Fig. A.8 shows.

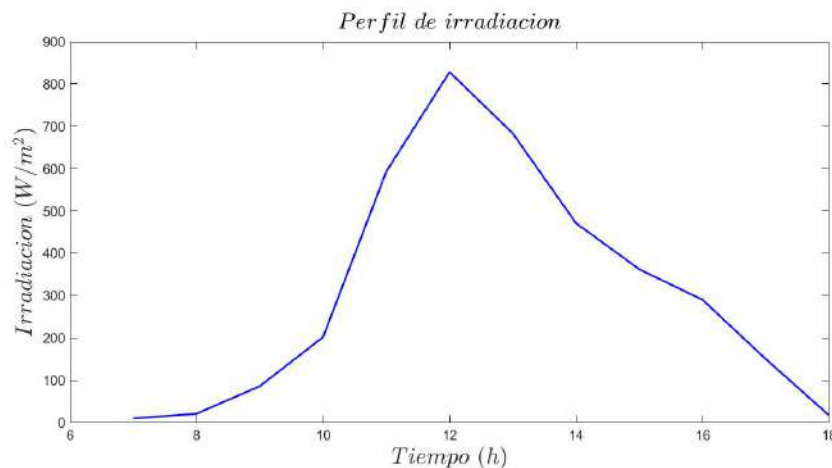


Figure A.7: Solar radiation profile used in the example

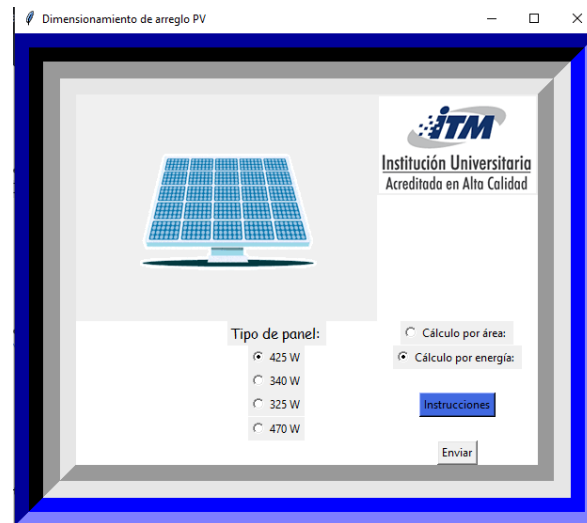


Figure A.8: Computation by energy example

As Figure A.9 illustrates, while the second window is deployed, the user must follow the instructions as Figure A.6 illustrates, that is to say, the user loads the solar radiation profile clicking on **Cargar perfil de irradiación**, next the user types the energy value in kWh, in this case 300, in the panel **Energía a suplir en (kWh)**, lastly the user click on the button **Calcular**. Figure A.9 shows the computed data which correspond to the data described in section A.1.1. If the user wants, the data can be exported to be saved in a *.txt* file clicking on the button **Exportar datos**. The file generated named as *datos.txt*

When the app opens the second window as it is shown in Figure A.9, the user needs to follow the instructions as Figure A.6 shows, that is to say, it is necessary to upload the solar radiation profile, next, write the energy value in kWh, in this case, 300, in the **Energía a suplir en (kWh)** box and for last, click on button **Calcular**. Figure A.9 shows the computed data which correspond to the described in section A.1.1. The user can export the data and save them in a *.txt* file by clicking on **Exportar datos** button. The file generated named *datos.txt* has the data shown in Figure A.10, with this file can be decided to recalculate the PV array by clicking on **Nuevo cálculo** button or, continue with the computation of the storing system as it will be shown further.

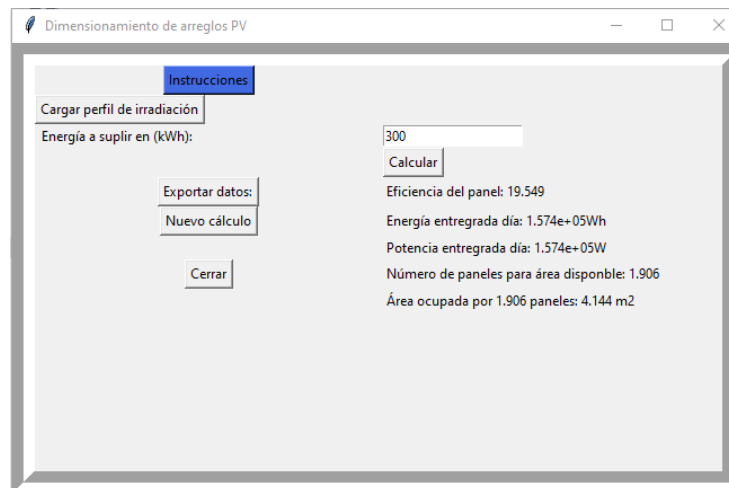


Figure A.9: Example of computed data by energy option

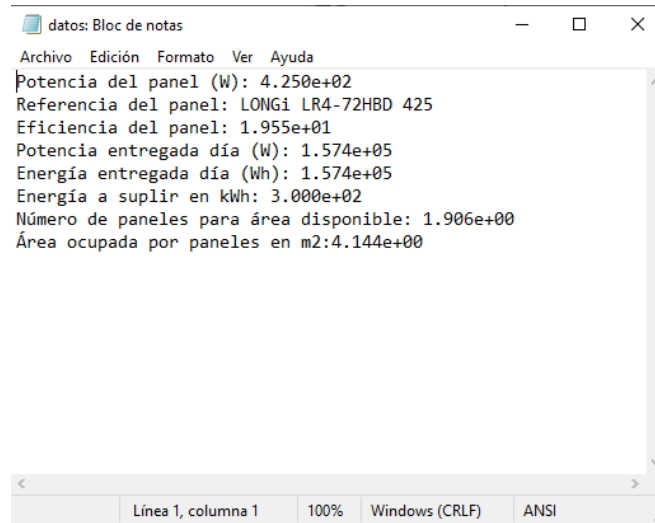


Figure A.10: Exported data of computation by energy option

### A.1.3. APPENDIX

#### DOWNLOAD DATA FROM DATABASES OF SOLAR RADIATION IN THE WEB

As it was explained previously, the GUIDE needs solar radiation data from the area where the PV array is going to be installed, in some occasions, it is not a simple task to perform measurements by its own, then it exist some web pages which have meteorological stations that acquired the temperature and solar radiation data and then, the users can download this information. In this section, this process will be explained, there will be used the data from the web page of *National Renewable Energy Laboratory* (NREL) in the international case and the *Instituto de Hidrología, Meteorología y Estudios Ambientales* (IDEAM) for the national case.

#### NREL

The first step is to access to the main page of the NSRDB Data Viewer with the following link: <https://maps.nrel.gov/nsrdb-viewer/>, where it can be seen the page shown in Fig. A.11.

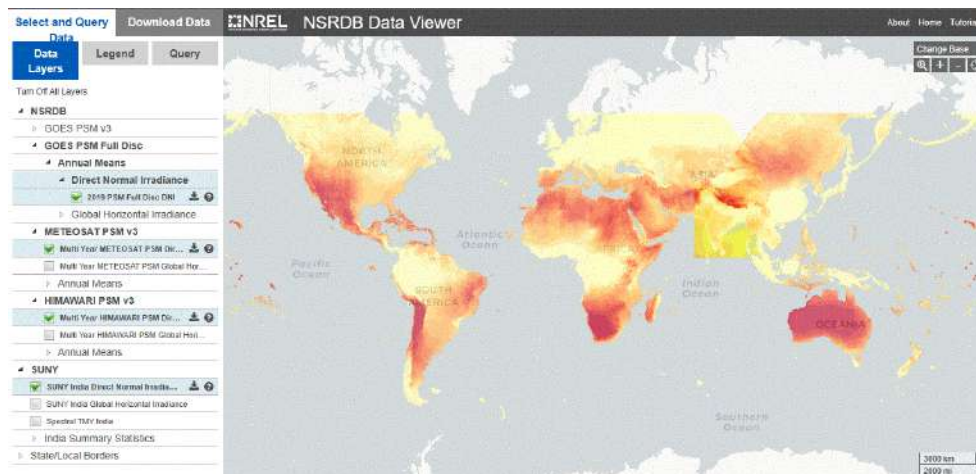


Figure A.11: Main data of the NSRDB Data Viewer

Exploring each section, in *Data Layers* it is necessary to select the data of solar radiation to download, depending on the database source (i.e GOES PSM, METEOSAT, HIMAWARI), and if it is normal direct solar radiation

or horizontal global solar radiation. Figure A.12 shows this section.

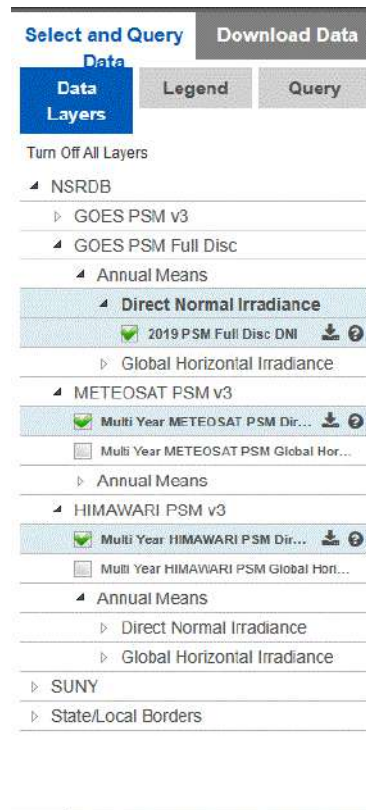


Figure A.12: Data Layers view

In *Legend* section, as Figure A.13 expose, there are defined the spectrum for each type of data base.

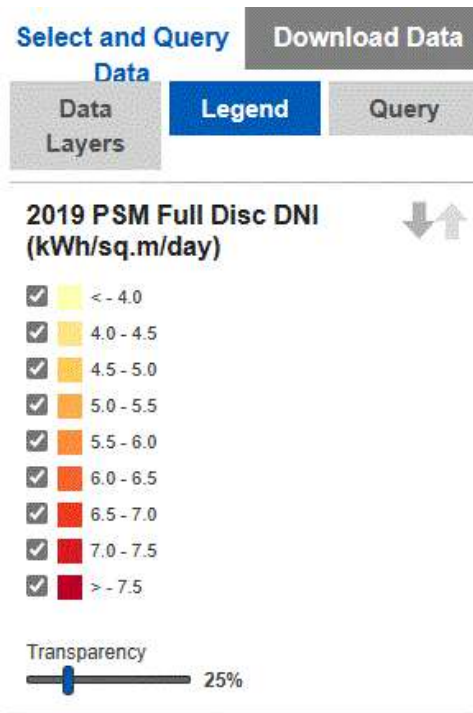


Figure A.13: Legend view

In *Query* section, it can be seen the types of area to select, that is to say, a portion of the area corresponds to *Region Query* or a punctual zone corresponds to *Point Query*. As Figure A.14 illustrates, by choosing a *Point Query*, the average DNI (Direct Normal Irradiance) is shown in the punctual zone.

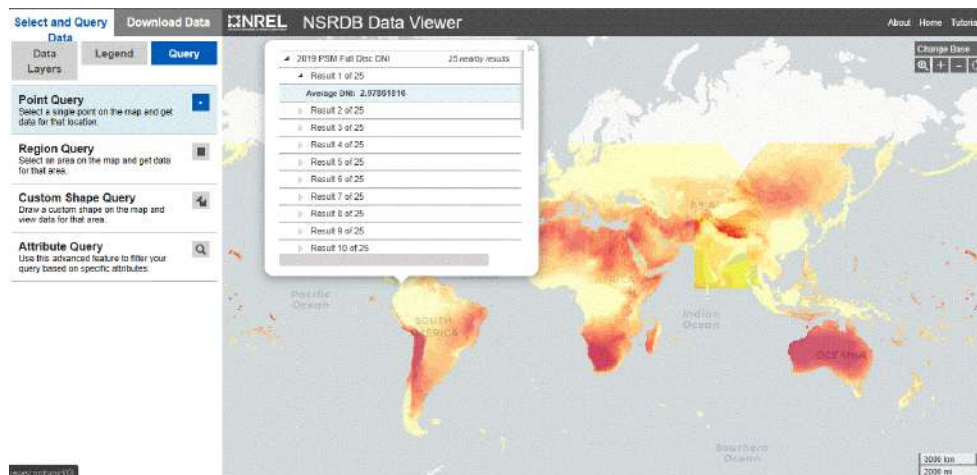


Figure A.14: Query view

Fig. shows the general view of the *Download Data* section where it can be selected a specific point in the zone (*Point*) or a square of area (*Box*), in this case, the option *Point* is selected.

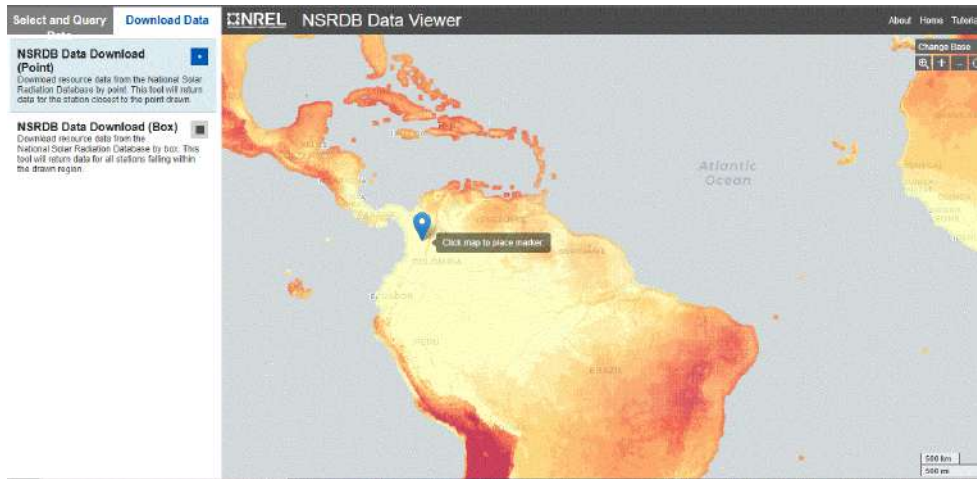


Figure A.15: View to download data with Point

After choosing the area to download the data, it pops up the window of Figure A.16 in which is necessary to write the requested data, then the user clicks on *Continue*.

 The image shows a "Data Download Information Form" window. It contains the following fields and elements:
 

- A heading: "Data Download Information Form"
- Text: "Please fill out the following information in order to utilize the data download tool. This information helps us to justify improvements to the tool."
- Note: "Note: All fields are required."
- Form fields:
  - Full Name: [text input]
  - Email: [text input]
  - Organization/Affiliation: [text input]
  - Planned Use: [text input]
- Checkbox: "Please keep me informed of future releases and publications." (unchecked)
- Button: "Continue" (bottom right)

Figure A.16: Form to download data

After filling out the form, the window in Figure A.17 opens where the user selects the data to be downloaded and the database. The available databases it can be found in the top of the window and these are *Full Disc*, *Spectral On-demand*, *PSM v3* and *PSM v3 TMY*, in this case, it is selected *PSM v3*. By choosing the database, it is necessary to choose the year of the data to be downloaded, the attributes such as DNI, Global Horizontal Irradiance (GHI), Diffuse Horizontal Irradiance (DHI), wind speed, the albedo of the surface, etc. The last option to select is the time base, in this case, half-hour intervals and convert UTC to the local hour. The last step in the web page is to click on *Download Data*.

**Data Download Wizard**

Asia/Pacific Himawari Solar Data    Himawari 2011-15 PSM v3    MSG IODC: PSM v3

Spectral TMY India    PSM v3 5 Minute    Puerto Rico SHR    **PSM v3**    PSM v3 TMY

SUNY India    **Full Disc**    SUNY India TMY    Spectral On-demand

**Physical Solar Model (PSM3)**

measurements of solar radiation—global horizontal, direct normal, and diffuse horizontal irradiance—and meteorological data. These data have been collected at a sufficient number of locations and temporal and spatial scales to accurately represent regional solar radiation climates.

Supported by the U.S. Department of Energy's SunShot Initiative, the NSRDB is a widely used and relied-upon resource. The database is managed and updated using the latest methods of research by a specialized team of forecasters at the National Renewable Energy Laboratory (NREL).

[Documentation](#)

Dr. Manoj L. Sengupta  
National Renewable Energy Lab  
Contact

**Select Years**    [Select All](#)    [Clear All](#)

2004     2005     2006     2007     2008     2009  
 2010     2011     2012     2013     2014     2015  
 2016     2017     2018     2019     2020

**Select Attributes**    [Select All](#)    [Clear All](#)

The minimum required attributes for the SAM PV and CSP modes have been selected by default.

DHI     DNI     GHI  
 Clearsky DHI     Clearsky DNI     Clearsky GHI  
 Cloud Type     Dew Point     Solar Zenith Angle  
 Fill Flag     Surface Albedo     Wind Speed

**Select Download Options**    [Select All](#)    [Clear All](#)

Include Leap Day     Convert UTC to Local Time     Half Hour Intervals

Download Limit Indicator

[Edit User Info](#)    [Download Data](#)

Figure A.17: Window of data selection for download

Fig. A.18 shows the data selection to download for the database *Full Disc*.

**Select Years**    [Select All](#)    [Clear All](#)

2019     2020

**Select Attributes**    [Select All](#)    [Clear All](#)

Dew Point     DNI     Fill Flag  
 GHI     Ozone     Relative Humidity  
 Solar Zenith Angle     Surface Albedo     Pressure  
 Precipitable Water     Wind Direction     Wind Speed

**Select Download Options**    [Select All](#)    [Clear All](#)

Include Leap Day     Convert UTC to Local Time     Select Interval (Minutes) 60

Download Limit Indicator

[Edit User Info](#)    [Download Data](#)

Figure A.18: Data selected with Full Disc option

After clicking in *Download Data*, it pops up an informative window from Figure A.19 where the user is informed that the link to download his data will be sent by email.



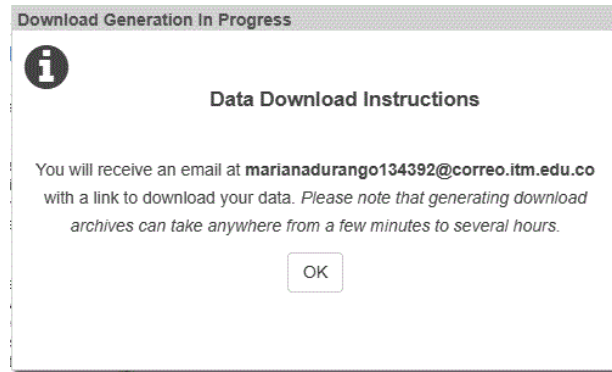


Figure A.19: Data download information

Figure A.20 illustrates the view of the email sent by NREL. After clicking on the link, the download will start in a .zip file.

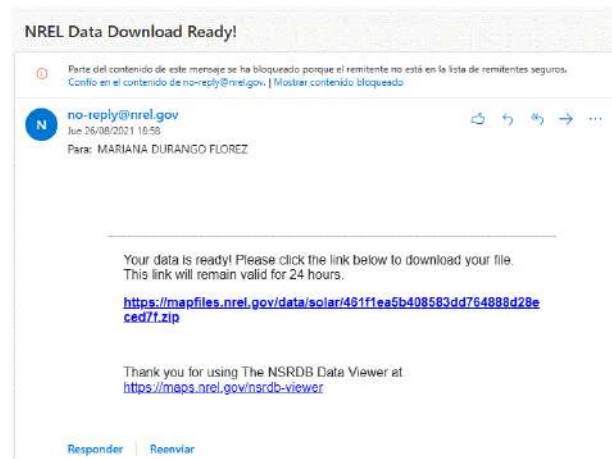


Figure A.20: View of the email for data downloading

After finishing the download and unzip the file, there is a .csv file with the data chosen in the web page, as Figure A.21 shows with the downloaded data from the database *Full Disc*. This type of files can be displayed and processed in *Matlab*®. The most important data are DHI, DNI and GHI which correspond to solar radiation.

Year	Month	Day	Hour	Minute	DHI	Temperature	DNI	GHI	SurfaceAtt...	VarName11	VarName12	VarName13	VarName14	VarName15	VarName16	VarName17	VarName18	
1	Source	LocationID	City	State	Country	Latitude	Longitude	Time Zone	Elevation	Local Time...	Cloudy D...	Cloudy D...	Cloudy S...	Dew Point...	DHI Units	DNI Units	GHI Units	Solar Zi...
2	NSRDB	4851468			Arizkoaipia	Colombia	5.62	-75.15	-3	1356	-5	w/m2						
3	Year	Month	Day	Hour	Minute	DHI	Temperature	DNI	GHI	Surface Att...								
4	2020	1	1	0	0	0	18.5	0	0	0.16								
5	2020	1	1	1	0	0	18.2	0	0	0.16								
6	2020	1	1	2	0	0	18	0	0	0.16								
7	2020	1	1	3	0	0	17.8	0	0	0.16								
8	2020	1	1	4	0	0	17.6	0	0	0.16								
9	2020	1	1	5	0	0	17.4000000...	0	0	0.16								
10	2020	1	1	6	0	0	17.4000000...	0	0	0.16								
11	2020	1	1	7	0	15	18.2	0	15	0.16								
12	2020	1	1	8	0	38	18.9000000...	0	38	0.16								
13	2020	1	1	9	0	145	20.3	1	146	0.16								
14	2020	1	1	10	0	226	22.4000000...	13	236	0.16								
15	2020	1	1	11	0	243	23.7000000...	15	256	0.16								
16	2020	1	1	12	0	351	24.5	19	317	0.16								
17	2020	1	1	13	0	180	24.5	8	196	0.16								
18	2020	1	1	14	0	57	24.2000000...	0	57	0.16								
19	2020	1	1	15	0	387	21.5	215	440	0.16								
20	2020	1	1	16	0	194	22.5	222	290	0.16								
21	2020	1	1	17	0	11	21.1	0	11	0.16								
22	2020	1	1	18	0	0	20	0	0	0.16								

Figure A.21: View example of the data downloaded from Full Disc option

## IDEAM

The first step is to access the main website of "Consulta y Descarga de Datos Hidrometeorológicos" in the following link: <http://dhime.ideam.gov.co/atencionciudadano/>, where the user can observe the page of Figure A.22.

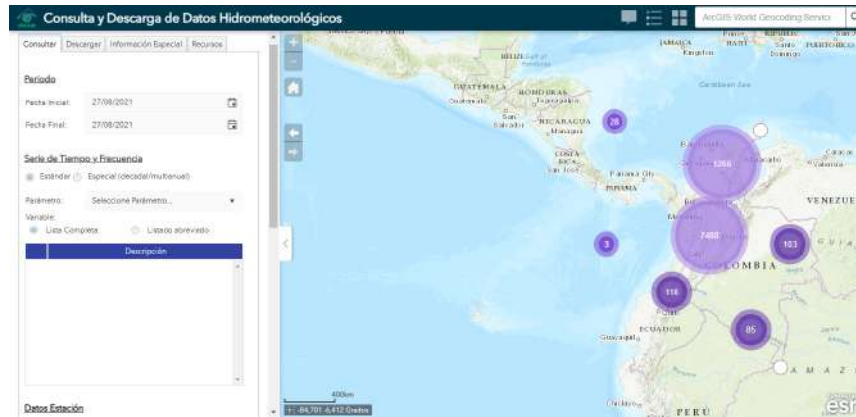


Figure A.22: Main view of *Consulta de datos hidrometeorológicos*

Double-clicking on the map or using the icon + to maximize, it is possible to identify the different weather stations in the zone, such as Figure A.23 illustrates delimited by red icons in the map.

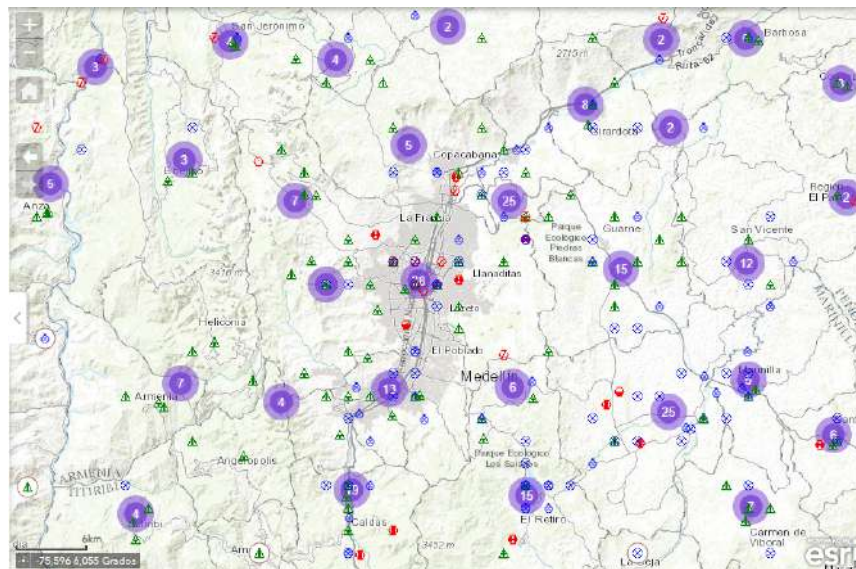


Figure A.23: Weather stations view

Once the map is recognized, it is necessary to select the weather stations closest to the zone of interest. Clicking on the station, it pops up the date and exact area of installation as Figure A.24 shows .

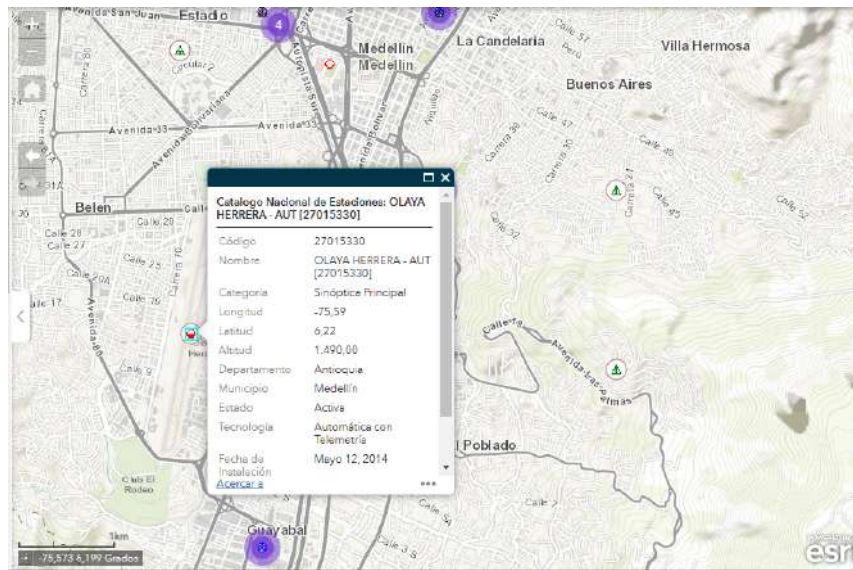



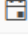
Figure A.24: Weather station information

Identifying the options presented in the menu of the left part of the web page, as Figure A.25 shows, in the tab *consultar* first it as to be chosen the starting and ending dates for obtaining the information. It is recommended as starting date, the date of the installation of the station. Next, in *Serie de tiempo y Frecuencia* the user chooses the *Estándar* option, then it is selected the search parameter, as in Figure A.25 it is selected *RAD SOLAR*, and from the description menu, it can be selected *Radiación solar global horaria VALIDADA*.

Consultar Descargar Información Especial Recursos

**Periodo**

Fecha Inicial: 12/05/2014 

Fecha Final: 27/08/2021 

**Serie de Tiempo y Frecuencia**

Estándar  Especial (decadal/multianual)

Parámetro: RAD SOLAR ▼

Variable:

Lista Completa  Listado abreviado

	Descripción	
<input type="radio"/>	Radiación solar global cada dos minutos VALIDADA...	▲
<input checked="" type="radio"/>	Radiación solar global horaria VALIDADA	
<input type="radio"/>	Radiación solar global diaria VALIDADA	
<input type="radio"/>	Radiación solar global acumulada diaria	
<input type="radio"/>	Radiación solar global acumulada diaria mínima men...	
<input type="radio"/>	Radiación solar global acumulada diaria máxima men...	
<input type="radio"/>	Radiación solar global media mensual	▼

Figure A.25: Data consultation



Figure A.26: Solar radiation parameter selection

In the final part of the *Consulta* menu, the user needs to select the district, department, and station from which the solar radiation data will be obtained. Finally, the user click on *Agregar a la consulta*.

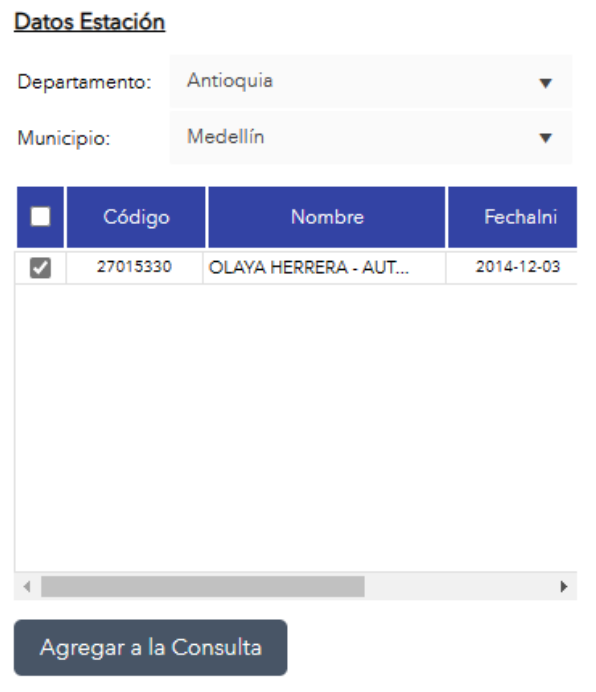


Figure A.27: Selection of the weather station for consult

After *Agregar a la consulta*, the next step is in the tab *Descargar* where it can be observed the data to download,

lastly, the user clicks on *Descargar* and download will start, the data will be downloaded in a .zip file.

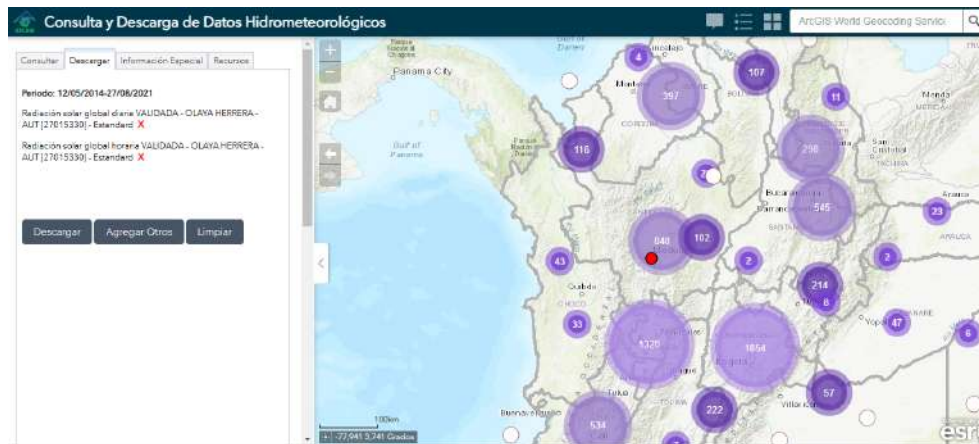


Figure A.28: Download of the selected solar radiation data

After finishing the download and unzipping the file, it can be found a .csv file with the selected data on the web page, as Figure A.29 shows. This type of file can be visualized and processed in *Matlab*<sup>®</sup>, the most important data are in the *Valor* column which corresponds to solar radiation.

Est.	NombreEst.	Latitud	Longitud	Altitud	Categoría	Entidad	AreaOperat.	Departam.	Municipio	FechaInstal.	FechaSup.	IdParametro	Etiqueta	Descripción	Frecuencia	Fecha	Valor
77	30	OLAYA HE.	6.22	-75.59	1490	Sinóptica P.	INSTITUTO	Area Opera.	Antioquia	Medellin	12/05/2014	...	RAD SOLAR	RSIVAL_A...	Radiación s...	Horaria	2014-12-06 ... 12.1
78	30	OLAYA HE.	6.22	-75.59	1490	Sinóptica P.	INSTITUTO	Area Opera.	Antioquia	Medellin	12/05/2014	...	RAD SOLAR	RSIVAL_A...	Radiación s...	Horaria	2014-12-06 ... 0
79	30	OLAYA HE.	6.22	-75.59	1490	Sinóptica P.	INSTITUTO	Area Opera.	Antioquia	Medellin	12/05/2014	...	RAD SOLAR	RSIVAL_A...	Radiación s...	Horaria	2014-12-06 ... 0
80	30	OLAYA HE.	6.22	-75.59	1490	Sinóptica P.	INSTITUTO	Area Opera.	Antioquia	Medellin	12/05/2014	...	RAD SOLAR	RSIVAL_A...	Radiación s...	Horaria	2014-12-06 ... 0
81	30	OLAYA HE.	6.22	-75.59	1490	Sinóptica P.	INSTITUTO	Area Opera.	Antioquia	Medellin	12/05/2014	...	RAD SOLAR	RSIVAL_A...	Radiación s...	Horaria	2014-12-06 ... 0
82	30	OLAYA HE.	6.22	-75.59	1490	Sinóptica P.	INSTITUTO	Area Opera.	Antioquia	Medellin	12/05/2014	...	RAD SOLAR	RSIVAL_A...	Radiación s...	Horaria	2014-12-06 ... 0
83	30	OLAYA HE.	6.22	-75.59	1490	Sinóptica P.	INSTITUTO	Area Opera.	Antioquia	Medellin	12/05/2014	...	RAD SOLAR	RSIVAL_A...	Radiación s...	Horaria	2014-12-07 ... 0
84	30	OLAYA HE.	6.22	-75.59	1490	Sinóptica P.	INSTITUTO	Area Opera.	Antioquia	Medellin	12/05/2014	...	RAD SOLAR	RSIVAL_A...	Radiación s...	Horaria	2014-12-07 ... 0
85	30	OLAYA HE.	6.22	-75.59	1490	Sinóptica P.	INSTITUTO	Area Opera.	Antioquia	Medellin	12/05/2014	...	RAD SOLAR	RSIVAL_A...	Radiación s...	Horaria	2014-12-07 ... 0
86	30	OLAYA HE.	6.22	-75.59	1490	Sinóptica P.	INSTITUTO	Area Opera.	Antioquia	Medellin	12/05/2014	...	RAD SOLAR	RSIVAL_A...	Radiación s...	Horaria	2014-12-07 ... 0
87	30	OLAYA HE.	6.22	-75.59	1490	Sinóptica P.	INSTITUTO	Area Opera.	Antioquia	Medellin	12/05/2014	...	RAD SOLAR	RSIVAL_A...	Radiación s...	Horaria	2014-12-07 ... 0
88	30	OLAYA HE.	6.22	-75.59	1490	Sinóptica P.	INSTITUTO	Area Opera.	Antioquia	Medellin	12/05/2014	...	RAD SOLAR	RSIVAL_A...	Radiación s...	Horaria	2014-12-07 ... 0
89	30	OLAYA HE.	6.22	-75.59	1490	Sinóptica P.	INSTITUTO	Area Opera.	Antioquia	Medellin	12/05/2014	...	RAD SOLAR	RSIVAL_A...	Radiación s...	Horaria	2014-12-07 ... 0
90	30	OLAYA HE.	6.22	-75.59	1490	Sinóptica P.	INSTITUTO	Area Opera.	Antioquia	Medellin	12/05/2014	...	RAD SOLAR	RSIVAL_A...	Radiación s...	Horaria	2014-12-07 ... 41.9
91	30	OLAYA HE.	6.22	-75.59	1490	Sinóptica P.	INSTITUTO	Area Opera.	Antioquia	Medellin	12/05/2014	...	RAD SOLAR	RSIVAL_A...	Radiación s...	Horaria	2014-12-07 ... 130.2
92	30	OLAYA HE.	6.22	-75.59	1490	Sinóptica P.	INSTITUTO	Area Opera.	Antioquia	Medellin	12/05/2014	...	RAD SOLAR	RSIVAL_A...	Radiación s...	Horaria	2014-12-07 ... 328.4
93	30	OLAYA HE.	6.22	-75.59	1490	Sinóptica P.	INSTITUTO	Area Opera.	Antioquia	Medellin	12/05/2014	...	RAD SOLAR	RSIVAL_A...	Radiación s...	Horaria	2014-12-07 ... 606.5
94	30	OLAYA HE.	6.22	-75.59	1490	Sinóptica P.	INSTITUTO	Area Opera.	Antioquia	Medellin	12/05/2014	...	RAD SOLAR	RSIVAL_A...	Radiación s...	Horaria	2014-12-07 ... 252.8
95	30	OLAYA HE.	6.22	-75.59	1490	Sinóptica P.	INSTITUTO	Area Opera.	Antioquia	Medellin	12/05/2014	...	RAD SOLAR	RSIVAL_A...	Radiación s...	Horaria	2014-12-07 ... 205.6
96	30	OLAYA HE.	6.22	-75.59	1490	Sinóptica P.	INSTITUTO	Area Opera.	Antioquia	Medellin	12/05/2014	...	RAD SOLAR	RSIVAL_A...	Radiación s...	Horaria	2014-12-07 ... 514.4
97	30	OLAYA HE.	6.22	-75.59	1490	Sinóptica P.	INSTITUTO	Area Opera.	Antioquia	Medellin	12/05/2014	...	RAD SOLAR	RSIVAL_A...	Radiación s...	Horaria	2014-12-07 ... 506
98	30	OLAYA HE.	6.22	-75.59	1490	Sinóptica P.	INSTITUTO	Area Opera.	Antioquia	Medellin	12/05/2014	...	RAD SOLAR	RSIVAL_A...	Radiación s...	Horaria	2014-12-07 ... 175.8

Figure A.29: View of the downloaded data of the IDEAM web page

#### A.1.4. STORING SYSTEM COMPUTATION

For the storing system computation it is necessary the following procedure:

- **Autonomy day definition:** It must be defined the amount of days on which the user wants the system to operate autonomously with the stored energy in the batteries. It should be considered that there is three times more energy in the batteries than is consumed: the three days of autonomy can be spent in one day with a consumption three times higher than usual or the user can have six days of autonomy spending half of it.
- **Batteries capacity:** The first step is to have the consumption data of the system to be supplied with the PV array in Wh/day. Then, the user multiplies this consumption by the autonomy days defined by the user. With the information of power requirement, this value has to be double (i.e.  $P_{battery} * 2$ ), as it is not recommended to lower the depth of discharge of batteries below 50%. Now, to calculate the capacity of the batteries, this total power is divided by the voltage at which the system will work, that is, the DC bus

voltage, which is generally 24V or 48V. Next, there is an example illustrated in [? ], reporting a house with a total consumption of 5100 Wh/day. The mathematical operation with the autonomy days is developed as follows:

$$P_{battery} \text{ (For three autonomy days)} = 5100 \frac{Wh}{día} \times 3 \text{ días} = 15300W$$

Now, considering the double of the battery capacity:

$$P_{battery} = P_{battery} \times 2 \text{ (50\% of depth of discharge)} = 30600 W$$

Computing the battery capacity ( $C_{battery}$ ) for a DC bus of 24 V:

$$C_{battery} = \frac{30600W}{24V} = 1275 \text{ Ah for 24 V system}$$

- Battery options: Once the storage capacity of the batteries has been calculated, then there are presented some battery models commonly used in PV installations.
  - Stationary Lead Acid Batteries
  - Monoblock batteries
  - Li-Ion batteries
- Power inverter selection: It is related to the type of connection of the PV system (i.e. off-grid or on-grid) and with the DC bus (i.e. 24 V or 48 V). Additionally, it needs to be considered the DC input voltage, maximum current, and frequency range. Its efficiency regards the AC output and the nominal power output. The power of the inverter is chosen regarding the installed power in the PV array, with a security factor of 10%.
- Regulator selection: To choose a regulator it must be considered the maximum power delivered by the PV system, the maximum voltage of the PV input, the voltage of the DC bus, output voltage levels, short circuit current, protections, alarm indicators, and battery state. Additionally, to consider possible peaks of solar radiation or temperature changes, it is recommended to choose a regulator with a 15-25% short circuit current higher than the generated for the PV system. The most common type of regulators are named below:
  - MPPT
  - PWM
  - Dual Battery

## A.2. ANALYSIS OF ELECTRICAL MODELS FOR PHOTOVOLTAIC CELLS UNDER UNIFORM AND PARTIAL SHADING CONDITIONS

This section describes the published paper named "Analysis of Electrical Models for Photovoltaic Cells under Uniform and Partial Shading Conditions" which is a result of the thesis.

### A.2.1. INTRODUCTION

When analyzing the behavior of PV arrays, aspects such as power generation, shading impact, MPPT controller design [1], and degradation are examined. However, power generation is one of the most important aspects because it is associated with performance and reliability. The power output in PV systems is mainly affected by partial shading, a condition that forces the shaded cells to consume power rather than produce it [2]. This condition imposes a negative voltage on its terminals, making the cell operate in the second quadrant  $Q_2$  (negative cell voltage and positive cell current, thus consuming power). Figure A.30 shows the experimental I-V curve of a monocrystalline cell with short-circuit current  $I_{sc} = 0.43A$  and open-circuit voltage  $V_{oc} = 0.5V$ . Such a figure shows both the first and second quadrants  $Q_1$  and  $Q_2$ , respectively, where  $Q_1$  exhibits positive cell voltage and current, hence producing power. Finally, the operation of the cell in  $Q_2$  is also known as reverse mode.

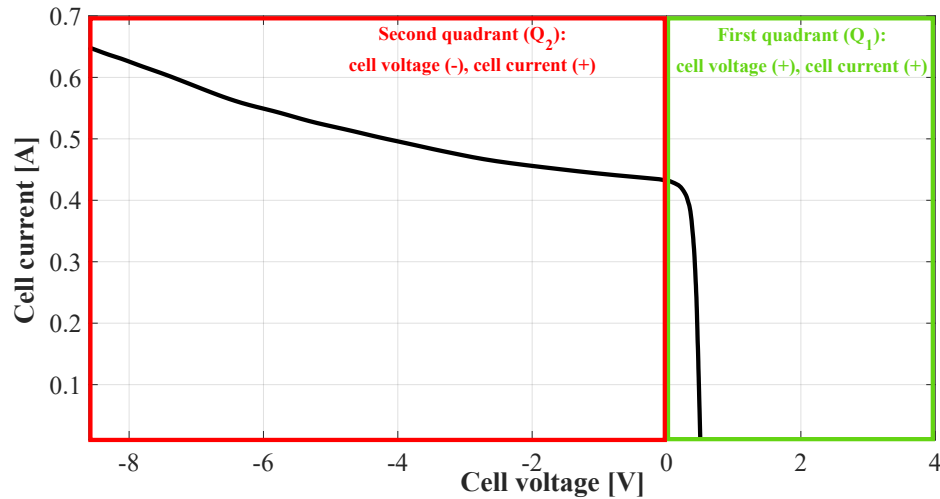


Figure A.30: The electrical characteristic of a PV cell

The first step in performing a proper analysis of PV arrays is to represent the operation of the PV cells and modules using circuit models such as the SDM, which is widely used due to its tradeoff between complexity and accuracy [3], or the Double Diode Model (DDM), which is more accurate to represent the p–n junction at low irradiance levels [4]. The Bishop model [5], for its part, aims to represent the behavior of a PV cell operating under partial shading conditions, which requires considering the second quadrant ( $Q_2$ ). Another model designed to study the behavior of PV cells under partial shading conditions is the Direct Reverse Model (DRM). This model is able to reproduce the operation of cells in either direct or reverse biasing modes to account for the influence of variations in temperature and solar irradiance [6].

The previous mathematical models require the accurate identification of a set of parameters to obtain a high-performance in the reproduction of the cell behavior. Several parameter estimation techniques have been reported in the literature for the different PV cell models. Those techniques can be divided into three categories: analytical, metaheuristic and hybrid techniques [7]. Each of these techniques require some initial data, which can be obtained from the manufacturer's datasheet or from experimental tests.

Analytical techniques use a series of mathematical equations for parameter extraction, which, in some cases, can result in a high computational burden and complex mathematical operations, which increases the computational time [7]. Metaheuristic techniques define the parameter identification problem as an optimization problem [3]. These are a promising alternative because they do not require an accurate mathematical model; instead, they need an objective function and a parameter search range, which can be more effective and less time consuming. Furthermore, those techniques evolve several individuals for the problem, which reduces the procedure's sensitivity to the initial guess and provides a strong ability to jump out of local optima [7]. Finally, hybrid techniques extract some of the initial parameters using analytical approaches, while the rest of the parameters are estimated by means of optimization algorithms.

However, Genetic Algorithms (GA) are the most widely adopted solution for parameter estimation in PV systems. For example, the work reported in [8] proposes a new variant of the GA, which integrates a new crossover operation to maintain a good balance between the intensification of the best solutions and the diversification of the search space; such a solution was designed to identify the electrical parameters of different PV cell models (SDM and DDM). Similarly, in [9] the authors extract the solar cell parameters for a Kyocera panel (KC200GT) using GA. In [10], an inverse modeling method for PV panel is proposed, which is based on parameter identification through GA. Such a process generates random groups of 5 parameters which are entered into the SDM; then, the parameters that generate a power output most similar to the experimental value are selected. On the other hand, [11] proposes an algorithm for datasheet parameter extraction of photovoltaic modules using the SDM, where the extracted parameters are obtained by approximation using a GA. Authors in [12] present the implementation of a continuous population genetic optimization algorithm (CGA) as a solution method for the parameter estimation of the diode model (SDM) in a PV panel from experimental data. Such a procedure was



validated with four different panels: Solarex MSX60, SOLAR SJ65, KYOCERA KC200GT, and STP245S.

Although the Bishop model is one of the most cited and used models to represent a PV cell operating under partial shading conditions [2, 13–15], there is not a clear procedure to estimate its parameters; instead, authors typically use parameters already reported in the literature. A similar situation occurs for the DRM [16]. Given the importance of having an accurate model for PV power generation analysis under partial shading conditions, there is a need for procedures to identify the parameters of the models. Moreover, procedures with a good relationship between complexity and accuracy, and the ability to be applied for different PV models, are also needed.

Therefore, this paper presents a behavior comparison between three models (SDM, Bishop, DRM) when the estimation of the current vs. voltage (I-V) curve in both  $Q_1$  and  $Q_2$  is needed. For this analysis, the first stage consists in estimating the parameters of the SDM, the Bishop model, and the DRM using genetic algorithms and Simulink simulations. Thus, the parameters to be estimated, the objective function, and the set of restrictions considered in the mathematical formulation for each model, are proposed. This study was validated by comparing two error measures (RMSE and MAPE) obtained from the I-V curve reconstruction of an experimental PV cell for each model, i.e. in both the first ( $Q_1$ ) and second ( $Q_2$ ) quadrants. Also, the result of the estimation of some points of interest, such as short-circuit current ( $I_{sc}$ ), open-circuit voltage ( $V_{oc}$ ), and voltage and current at the maximum power point ( $V_{mpp}$ ,  $I_{mpp}$ ) were evaluated and analyzed for each model. Finally, this work provides an estimation guide for modeling the behavior in the first and second quadrants, which is essential for evaluating power losses in photovoltaic systems under partial shadowing.

### A.2.2. MODELS' MATHEMATICAL REPRESENTATION

This section highlights the parameters to be estimated.

#### SINGLE DIODE MODEL

In the SDM circuit the current source is associated with the PV current and, the diode represents the energy level threshold for photons to trigger significant production and circulation of electron-hole pairs through the junction [17]. Losses are represented by a series resistance ( $R_s$ ), which is related to the metal–semiconductor contact resistance, the ohmic resistance of the contacts, and the ohmic resistance of the semiconductor material. The leakage currents along the edges of the cell are represented by shunt resistor ( $R_{sh}$ ).

The cell current ( $I_{cell}$ ) be obtained as the algebraic sum of the currents through the diode ( $I_d$ ), the current through the shunt resistor ( $I_{sh}$ ) and the photocurrent ( $I_{ph}$ ). Shockley's equation [18] models the current–voltage relationship in the diode ( $I_d - V_d$ ). Thus, (A.1) represents the resulting cell current ( $I_{cell}$ ).

$$I_{cell} = I_{ph} - I_0 \left( e^{(V_{cell} + I_{cell} R_s) / AV_T} - 1 \right) - \frac{(V_{cell} + I_{cell} * R_s)}{R_{sh}} \quad (A.1)$$

In Eq. (A.1),  $V_{cell}$  is the cell voltage,  $V_T$  is the thermal voltage; and  $I_0$  and  $A$ , the reverse saturation current and the ideality factor of the diode, respectively.

According to the introduction section, five parameters must be evaluated in the SDM to obtain the I–V characteristics of a PV cell. Importantly, this model is only used to represent the behavior of PV cell in  $Q_1$  when is delivering energy.

#### THE BISHOP MODEL

The model proposed by Bishop incorporates an avalanche mechanism into the SDM. This mechanism represents the reverse characteristics of the PV cell, which is controlled by the current through  $R_{sh}$ . This current term is composed of an ohmic term and a nonlinear multiplication factor [5] as shown in Eq. (A.2).

In the Bishop model, Eq.(A.2) relates the output current and the voltage of a PV cell, where  $a$  is the ohmic fraction of the current related to the avalanche breakdown;  $m$ , the avalanche breakdown exponent; and  $V_{br}$ , the junction breakdown voltage.

$$I_{cell} = I_{ph} - I_0 \left( e^{\frac{(V_{cell} + I_{cell} R_s)}{AV_T}} - 1 \right) - \frac{(V_{cell} + I_{cell} * R_s)}{R_{sh}} \left( 1 + a * \frac{(1 - (V_{cell} + I_{cell} R_s))}{V_{br}} \right)^{-m} \quad (A.2)$$

To represent the Bishop model, eight parameters must be estimated, according to the introduction section. This model is commonly used to represent the behavior of a PV cell in both  $Q_1$  and  $Q_2$ , with the cell consuming instead of producing power in  $Q_2$ .

#### DIRECT-REVERSE MODEL

The Direct-Reverse Model (DRM) makes it possible to model the behavior of PV cells in both direct and reverse polarization modes. Using the I-V characteristics from the same sorted series cells, the authors of [16, 19, 20] studied the variability of the curves, not only in the value of the breakdown voltage but also in the slopes of the ohmic regions in  $Q_2$ . Based on this characterization, they were able to observe parts of the curve in  $Q_2$  that could be linearized. In this model, a Thevenin equivalent in series with a diode in the opposite mode models each linear part, where the Thevenin resistance represents the slope of the linear region. As shown in Figure A.31, this model evaluates the behavior of a PV cell in  $Q_1$  using the double-diode model.

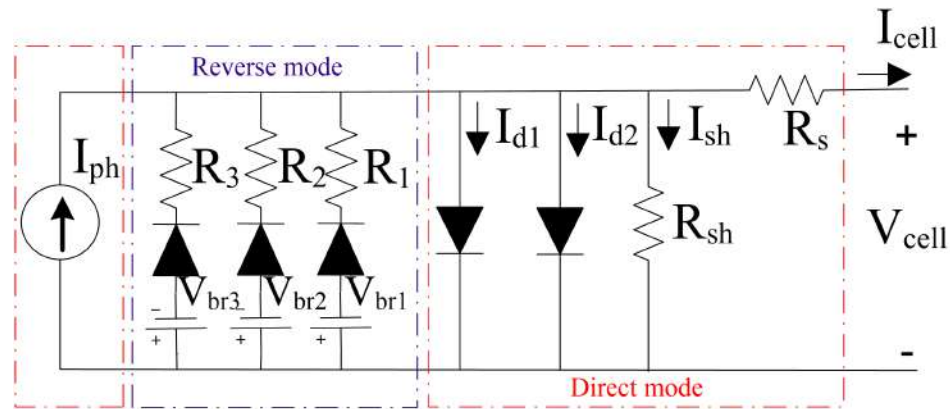


Figure A.31: Circuit diagram of the Direct-Reverse Model

The number of PV parameters that must be estimated depends on the number of branches used to represent the linear approximation. In the example of Figure A.31, the circuit is represented by 13 parameters (7 for the direct mode and 6 for the reverse mode). The DRM can be used for both  $Q_1$  and  $Q_2$  representation.

#### PV PANEL/ARRAY MODELING

An important application of the models described above lies in the capacity of been employed for the PV panel/array modeling, in both  $Q_1$  and  $Q_2$ . PV panel modeling is based on the PV cell model and the number of cells connected in series ( $N_s$ ) and in parallel ( $N_p$ ), as shown in section 3.2. Therefore, when modeling a PV array modeling, the number of panels and their connection must be considered. Another key aspect is the procedure used to solve the resulting equations regarding the connection between the PV panels and the number of parameters to estimate. The I-V characteristics of a PV array, as well as the maximum power reached under a given operating condition, can be obtained by solving such equations.

As previously discussed, each PV model has a defined number of parameters to estimate. Also, due to the nonlinear current-voltage relationship of the models, the cell or panel current ( $I$ ) is expressed as an implicit function of its voltage ( $V$ ), i.e.,  $f(I, V) = 0$ , which requires the use of numerical methods for its analysis and solution. Three types of techniques for parameter estimation have been reported in the literature: (i) metaheuristic techniques such as GA; (ii) analytical techniques such as Lambert W and iterative methods like the Newton-Raphson method; and (iii) hybrid techniques, which use metaheuristic and analytical methods for a more accurate I-V representation. Regarding the SDM, the authors of [21] used a Differential Evolution (DE) algorithm to estimate its five parameters, while the authors of [22] employ a Hybrid Java-NM algorithm for parameter extraction. The Newton-Raphson method was used in [23], whereas the Lambert W function was employed in [24] to find a solution. Due to its low complexity, the SDM is the most commonly used model for PV array modeling, as highlighted by the authors of [25]. Studies such as that in [26] suggest that parameter estimation

for SDM and the DDM, which is an extension of the SDM [27], can be estimated using the same algorithm. As a result, similar computational times are obtained depending on the technique used. In the case of metaheuristic algorithms, the objective function employed, and the tuning parameters of the algorithm have a considerable impact on computational times. The Bishop model can be enhanced with the SDM and the DDM. For instance, authors of [28] modeled a PV array employing the Bishop model with double diode. This solution, nonetheless, may require a higher computational time and be more complex due to the number of variables to estimate. In [29], the Bishop model was used for PV panel modeling, and each PV panel, string, and array were modeled using a piecewise polynomial function approximation, a process similar to that of the DRM. The DRM, which is similar to the Bishop model, is employed to model a PV cell behavior in both the direct and reverse operating modes. Nevertheless, the number of parameters to estimate, which is associated with the number of branches used to model the PV cell, makes it a complex model for PV parameter estimation and PV array modeling. Despite this, authors of [13] used the DRM to model a PV string. In addition, considering the PV panels connected in series/parallel, this model can be used for PV array representation. The complexity in modeling a PV array is determined by the PV cell model used. Therefore, depending on the PV cell data available, such as its technology (e.g., polycrystalline and CIGS), I–V characteristics, and working zone of the experimental tests (e.g.,  $Q_1$ ), the PV models discussed above can be employed for such purpose considering the number of variables to estimate and the method used to solve the associated equations. This study provides a first stage procedure for choosing a proper PV model for a given working condition by comparing the performance of each model with experimental data obtained from a PV cell.

### A.2.3. PROPOSED PARAMETER ESTIMATION TECHNIQUE

The parameter estimation problem for each model presented in Section A.2.2 was solved using the GA. Each step of the estimation process, which are explained in the next subsections, are related to the fitness function and the search space constrains, both of which must be accurately defined to avoid falling into a local minimum. A set of constrains, determined by the search space of the parameters when modeling PV cells, must also be defined. The literature describes the search space for the SDM and DDM of PV cells [30, 31] to represent only  $Q_1$ . Those ranges can be applied to the parameters that are shared by the Bishop model and the DRM; however, search ranges for the parameters that determine the behavior of PV cells in  $Q_2$  are also required. In the DRM, these ranges can be obtained using information contained in the experimental data of the I–V curve.

#### INITIAL POPULATION

A set of solution vectors is randomly generated within the search space to establish the current population, whose size is denoted by the population size ( $p$ ). All solution vectors in the initial population must be different (diversity criterion). Then, the fitness function of each solution vector is evaluated, and that with the minimum value is selected as the *incumbent*.

#### SELECTION

Chosen randomly from the initial population, with a length given by a random integer ( $r$ ). Therefore, to complete the new population,  $r - p$  solution vectors must be created. Next, a pair of solution vectors, which are named parents, are selected to proceed to the crossover stage.

#### CROSSOVER

In this stage, the two solution vectors selected are combined to produce a new vector called offspring, for which a parent crossing point is chosen. Thus, offspring will carry information from both parents.

#### MUTATION

This operation produces spontaneous changes in offspring. It is a random alteration of the value at an offspring's position.

#### POPULATION UPDATE

The algorithm repeats the selection, crossover, and mutation processes until  $p$  children are created. The fitness function of the offspring population must also be evaluated. Offspring and the initial population are concatenated, and then sorted in ascending order based on the evaluation of their fitness function. The first best  $p$  solution vectors will be selected as the initial population of the next generation.

### STOPPING CRITERION

In this study, the stop criterion is the maximum number of iterations for the estimation process (itermax), which are referred to as generations. Algorithm 3 presents the pseudocode of the GA described above.

### FITNESS FUNCTION

The fitness function ( $FF$ ) of the optimization problem addressed in this study, is to minimize the root mean square error ( $RMSE$ ) between the cell current measured in the experimental tests ( $I_{cell_m}$ ) and the value estimated with the optimization technique ( $I_{cell_e}(\phi)$ ), as shown in Eq. (A.3).

$$\min [FF(\phi)] = \min [RMSE(I_{cell_e}(\phi), I_{cell_m})] = \min \left[ \sqrt{\frac{1}{N} \sum_{i=1}^N (I_{cell_e}(\phi) - I_{cell_m})^2} \right] \quad (A.3)$$

$I_{cell_e}(\phi)$  results from evaluating the implicit equations (A.1) and (A.2) using the Newton Raphson method and the estimated parameters.  $\phi$  is the solution vector, which includes the unknown parameters of the model to be identified and  $N$  is the number of samples. Table A.1 presents the coding for the optimization problem considered here, which, as stated in the previous section, depends on the adopted PV model since each model has a specific number of parameters that describe its I-V characteristics.

Table A.1: Evaluation of the estimated  $I_{cell}$  for each model.

Model	$I_{cell_e}(\phi)$	Parameters to estimate ( $\phi$ )	Operation mode
SDM	(A.1)	$[I_{ph}, I_0, A, R_s, R_{sh}]$	$Q_1$
Bishop	(A.2)	$[I_{ph}, I_0, A, R_s, R_{sh}, V_{br}, m, a]$	$Q_1 - Q_2$
DRM	(A.1) Only for $Q_1$	$[I_{ph}, I_0, A, R_s, R_{sh}]$	$Q_1 - Q_2$

### PROBLEM CONSTRAINTS

The constraints of the optimization problem correspond to the search ranges of the parameters to be estimated, which are defined in equations (A.4), (A.5), (A.6), (A.7), (A.8), (A.9), (A.10), and (A.11). Those parameters correspond to the models reported in Section A.2.2, where the search ranges should be respected to ensure a correct estimation of the parameters in each model as presented in Table A.2.

$$A_{min} \leq A \leq A_{max} \quad (A.4)$$

$$R_{smin} \leq R_s \leq R_{smax} \quad (A.5)$$

$$R_{shmin} \leq R_{sh} \leq R_{shmax} \quad (A.6)$$

$$I_{omin} \leq I_o \leq I_{omax} \quad (A.7)$$

$$I_{phmin} \leq I_{ph} \leq I_{phmax} \quad (A.8)$$

$$a_{min} \leq a \leq a_{max} \quad (A.9)$$

$$m_{min} \leq m \leq m_{max} \quad (A.10)$$

$$V_{brmin} \leq V_{br} \leq V_{brmax} \quad (A.11)$$

Table A.2: Number of constraints for each model

Model	Constraints
SDM	Eqs. (A.4), (A.5), (A.6), (A.7), (A.8)
Bishop	Eqs. (A.4), (A.5), (A.6), (A.7), (A.8), (A.9), (A.10), (A.11)
DRM	Eqs. (A.4), (A.5), (A.6), (A.7), (A.8)

---

**Algorithm 3** Pseudocode of GA applied to PV cell parameter estimation.

---

**INPUT:** Experimental  $I - V$  data,  $p$ ,  $iter_{max}$ , search ranges

**OUTPUT:**  $\varphi$  iter=1

1. Generate initial population
  2. Evaluate the fitness function and constrains
  3. Select the best solution
  4. **While**  $iter = 2 : iter_{max}$ 
    - 4.1 **For**  $i = 1 : p$  Select  $r$  vectors of initial population  
Create  $p - r$  vectors randomly  
Generate the new population combining selected and created vectors  
Select two parents randomly from the new population  
Create offspring by recombining parents  
Mutate offspring  
Select the best offspring
    - 4.2 **End For** Generate offspring population  
Evaluate fitness function and constrains  
New population= [initial population; offspring population]  
Initial population= the best  $p$  solution vectors  
Select the best solution  $\varphi$
  5. **End While**
- 

#### A.2.4. RESULTS AND DISCUSSION

The I-V curve for the validation process was obtained from a monocrystalline cell with the following electrical characteristics, which was exposed to an irradiance of  $1008 W/m^2$  and a temperature of  $47.8^{\circ}C$ :

- Short-circuit current  $I_{sc} = 0.43 A$
- Open-circuit voltage  $V_{oc} = 0.5 V$
- Maximum power current  $I_{mp} = 0.36 A$
- Maximum power voltage  $V_{mp} = 0.5 V$

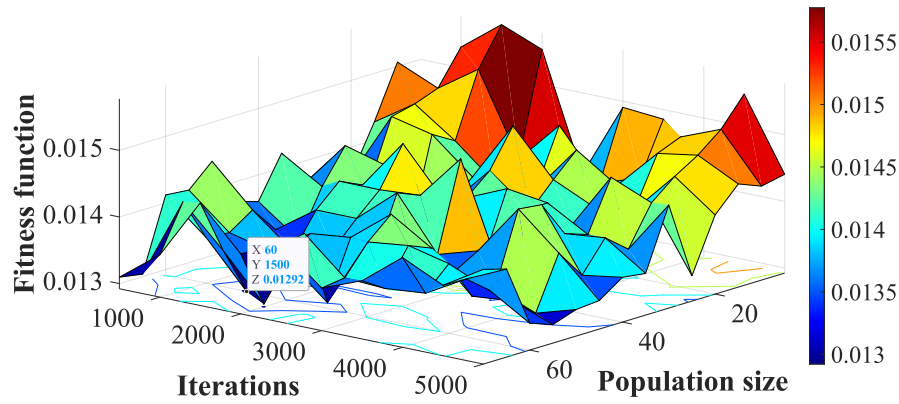
The models were simulated in MATLAB® R2021a on a computer with an Intel Core i5-5200U 2.2GHz processor, 8GB of RAM, and Windows 10 pro. The results obtained with each model, which are presented in the next subsection, were contrasted with the I-V curve obtained experimentally. Table A.3 reports the values of the constraints (i.e. the range of the parameters) used for the estimation problem addressed in this study.

Table A.3: Parameter constraints.

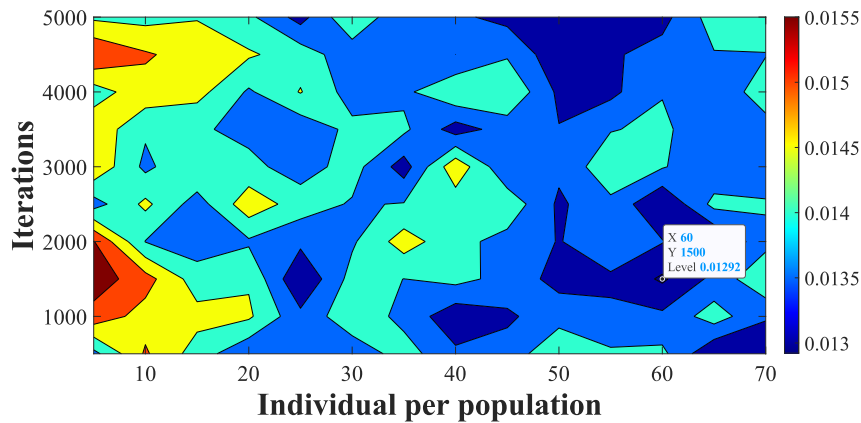
Parameter	Minimum value	Maximum value
$I_{ph}$	$90\% * I_{ph} [A]$	$110\% * I_{ph} [A]$
$I_0$	$1 \times 10^{-10} [A]$	$1 \times 10^{-7} [A]$
$A$	0.05	4
$R_s$	$1 \times 10^{-5} [\Omega]$	2 $[\Omega]$
$R_{sh}$	20 $[\Omega]$	100 $[\Omega]$
$V_{br}$	-10 $[V]$	-50 $[V]$
$m$	2	8
$a$	$1 \times 10^{-3}$	$30 \times 10^{-3}$

The number of individuals per population and the maximum number of iterations were defined by evaluating the GA in a range of [5, 70] individuals per population and [500, 5000] iterations. Figure A.32 illustrates

the tuning results for the SDM. As observed in Figure A.32a, there is an increment in the number of individuals per population and a decrement in the average value of the objective function with a decreasing number of iterations. Figure A.32b shows the contour of the surface, which reports that the objective function reaches its minimum with 65 individuals and after 1500 iterations. A parameter tuning was performed to determine the best number of individuals and iterations for estimating the parameters of each model. Table A.4 shows the results of that tuning process.



(a) Mesh of fitness function in relation with the number of iterations and population size



(b) Contour of fitness function in relation with the number of iterations and population size

Figure A.32: Selection of the estimation parameters for the SDM

Table A.4: Selection of GA variables for each model.

Variable	Individual per population	Number of iterations
SDM	60	1500
Bishop	5	500
DRM	60	500

Then, 100 repetitions of the parameter estimation algorithm (Algorithm 3) were evaluated using the GA variables provided in Table A.4 for each model, where the mean and standard deviation of each estimated parameter of the SDM, Bishop model, and DRM were calculated. Those metrics were also computed for the root mean

square error (RMSE), the mean absolute percentage error (MAPE), and the computational time of each model, as reported in Table A.5.

Table A.5: Parameters estimated for each model (mean ± standard deviation).

Parameter	SDM	Bishop	DRM
$I_{ph}$ [A]	$0.431 \pm 0.019$	$0.434 \pm 0.0244$	$0.433 \pm 0.025$
$I_0$ [ $10^{-8}$ A]	$5.665 \pm 2.538$	$5.722 \pm 2.538$	$5.118 \pm 3.023$
$A$	$1.172 \pm 0.065$	$1.361 \pm 0.219$	$1.179 \pm 0.081$
$R_s$ [ $\Omega$ ]	$0.211 \pm 0.086$	$0.619 \pm 0.390$	$0.267 \pm 0.124$
$R_{sh}$ [ $\Omega$ ]	$47.409 \pm 8.764$	$58.018 \pm 16.597$	$59.877 \pm 26.566$
$V_{br}$ [V]	--	$-24.58 \pm 9.15$	--
$m$	--	$-5.682 \pm 1.774$	--
$a$	--	$0.016 \pm 0.009$	--
RMSE	$0.022 \pm 0.008$	$0.047 \pm 0.017$	$0.032 \pm 0.013$
MAPE	$0.155 \pm 0.0940$	$0.3966 \pm 0.1843$	$0.318 \pm 0.169$
Time [s]	$49.803 \pm 0.867$	$1.274 \pm 0.601$	$3.123 \pm 0.206$

According to Table A.5, parameters  $I_0$  and  $R_{sh}$  have the highest standard deviation, although the RMSE and the MAPE values are considerably low for the three models. This put into evidence the impact of the  $R_{sh}$  parameter in the zone near to  $I_{sc}$ , which is the beginning of the  $Q_2$  zone. The low computation time of Bishop’s model supposes that the tuning parameters of GA are suitable for the number of parameters to estimate. In the case of SDM, computation time is higher since it has three times more iterations; a proper estimation of its parameters is a crucial task to ensure an accurate parameter estimation in  $Q_2$ . The parameters of the DRM in reverse mode, and reported in Figure A.31, were estimated following the instructions provided in [19]. First, it was necessary to identify the zones that could be linearized; in this case, the blue, red, and gray regions highlighted in Figure A.33 are the zones to be linearized. Breakdown voltages  $V_{br1}$ ,  $V_{br2}$ , and  $V_{br3}$  correspond to the points on the curve where the linear zone begins, i.e. 0V, 2.318V and 5.979V, respectively. The values of the resistors ( $R_1 = 90\Omega$ ,  $R_2 = 40\Omega$  and  $R_3 = 26.31\Omega$ ), which correspond to the slopes of the linear zones, were calculated through Ohm’s Law using the extreme points of the corresponding linear zone.

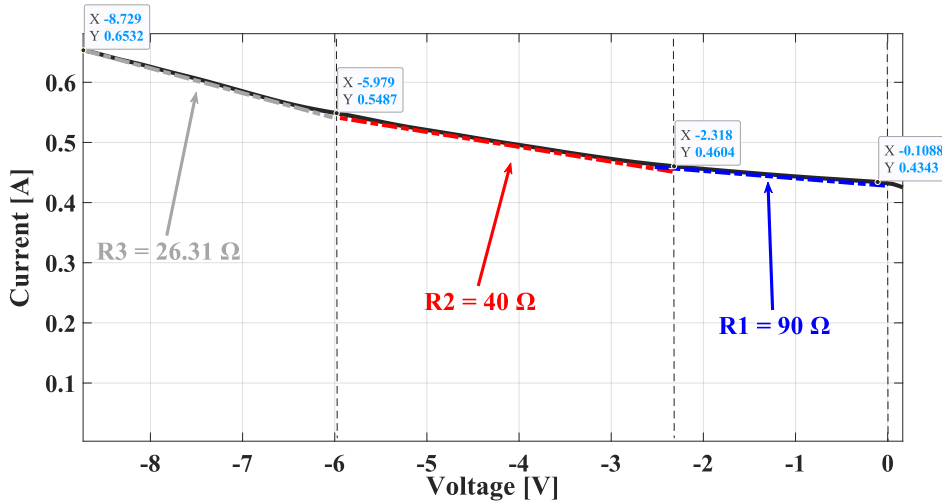


Figure A.33: Estimation of DRM parameters for  $Q_2$ .

The circuit in Figure A.31 was simulated in Simulink to obtain the I–V curve for the DRM. Then, an interpolation with the voltage vector of the experimental data was performed to compare the results of the cell current estimated by the DRM with that predicted by the SDM and the Bishop model.

Figure A.34 illustrates the I-V curves obtained with each model using the best population function results taken from Table A.6. In  $Q_1$ , the three models show a high accuracy between simulation and experimental data. In  $Q_2$ , the Bishop model provides the best result, while the SDM and the DRM exhibit a decrease in their accuracy.

The accuracy of the curve for the DRM depends on the linear zones chosen for the I-V characterization, as well as on the precise calculation of the number of branches. Moreover, the estimation of the parameters that define the DRM model in the first quadrant are the same ones used for the SDM, and those were estimated using only the information of the experimental I-V curve in the first quadrant. Finally, those parameters also affect the behavior of the models in the second quadrant ( $Q_2$ ).

On the other hand, it is observed that the estimation provided by the SDM did not have a good approximation in  $Q_2$ . This model presents a linear behavior for  $Q_2$ , thus the breakdown voltage is not observed. Here, for the parametrization of this model, the whole information of the experimental I-V curve was used ( $Q_1$  and  $Q_2$ ).

Table A.6: Parameters used for the best solution.

Parameter	SDM	Bishop	DRM
$I_{ph}[A]$	0.427	0.428	0.436
$I_0[10^{-8} A]$	6.325	9.957	3.391
$A$	1.165	1.201	1.115
$R_s[\Omega]$	0.157	0.179	0.117
$R_{sh}[\Omega]$	41.825	63.900	86.443
$V_{br}[V]$	--	-23.31	--
$m$	--	-6.975	--
$a$	--	0.025	--

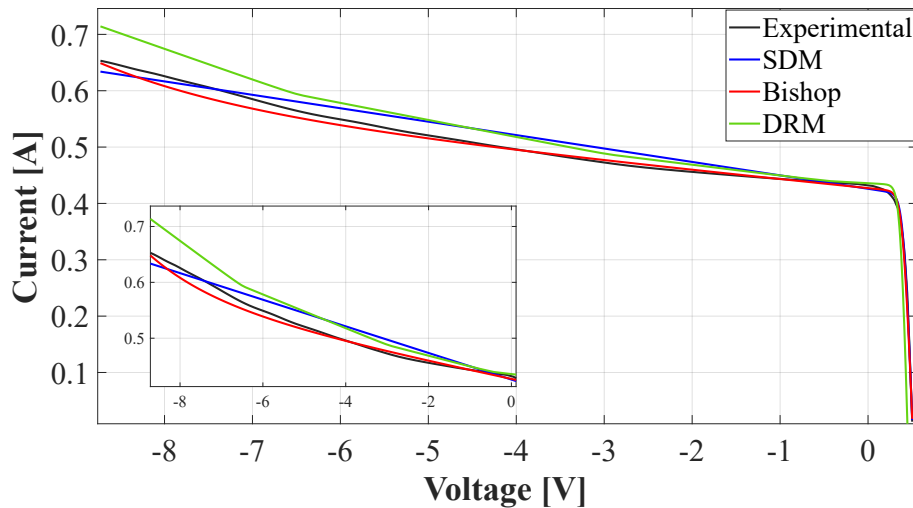


Figure A.34: Comparison between the experimental and estimated curves in  $Q_1$  and  $Q_2$  (zoom-in for  $Q_2$ ).

Table A.7 presents the relative error of the main points of interest, i.e.  $I_{sc}$ ,  $V_{oc}$ ,  $I_{MPP}$ , and  $V_{MPP}$ . The three models show low error values, making them suitable for applications where the delivered power needs to be estimated [32].

As observed in Figure A.35, the SDM and the Bishop model exhibit high accuracy for  $Q_1$  representation, especially at the Maximum Power Point (MPP), which is the most relevant point for power analysis. For the DRM, there is a significant difference in the estimation of  $V_{oc}$ , while the estimation of  $I_{sc}$  exhibits a lower difference. However, both differences affect the estimated location of the maximum power point (MPP) in comparison with the one obtained in the experimental stage.



Table A.7: Relative error of some points of interest in the I-V and P-V curves.

Parameter	SDM	Bishop	DRM
$I_{sc}$ [A]	0.0415	0.007	0.0246
$V_{oc}$ [V]	0.0795	$7.91 \times 10^{-4}$	0.1526
$I_{MPP}$ [A]	0.1316	0.0561	0.1422
$V_{MPP}$ [V]	0	0.0207	0.1134

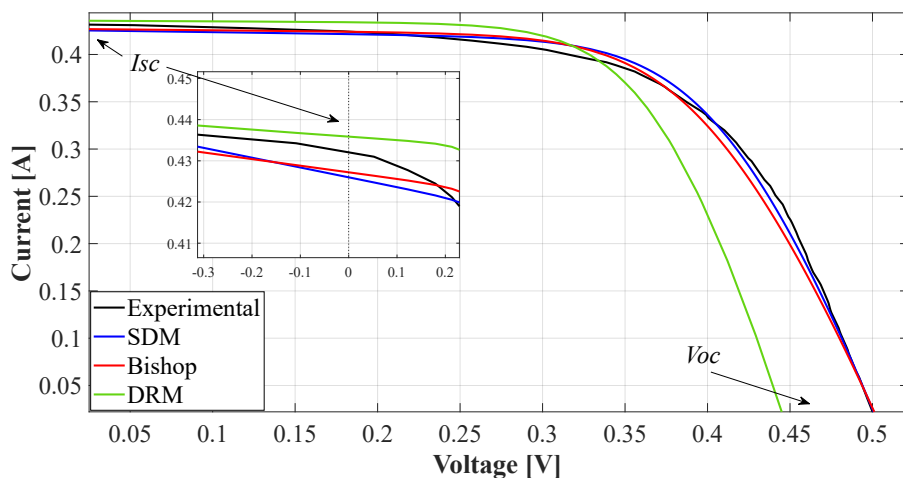


Figure A.35: Comparison between the experimental and estimated curves (zoom-in for  $I_{sc}$ ).

Figure A.36 shows the power vs. voltage (P-V) curves near the MPP obtained with each model. Such curves were generated using the best population function results taken from Table A.6. In this case, the Bishop model and SDM provide the best results for MPP estimation based on the experimental data. The Bishop model exhibits the smallest estimation error of 0.43%, while the error provided by SDM is 2.26%. On the other hand, the DRM presents an error of 4.01%, which is the highest deviation obtained.

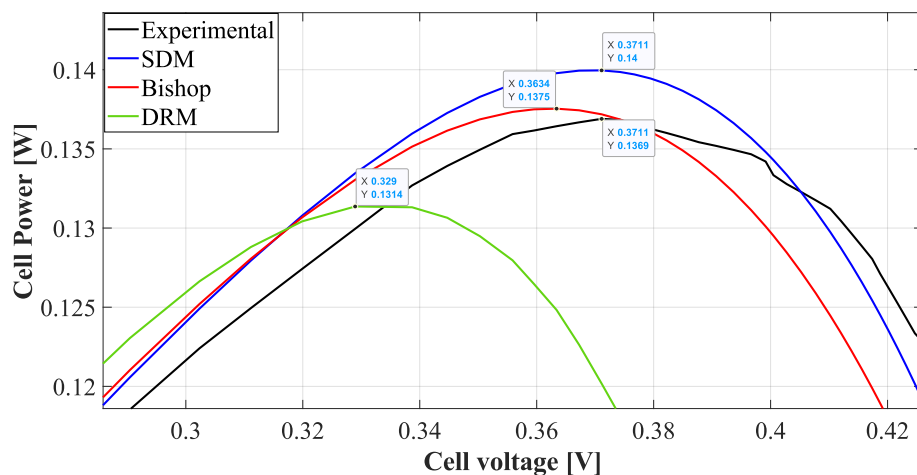


Figure A.36: Maximum power point for each model).

Finally, Figure A.37 depicts the errors obtained for the best estimation of the SDM, the Bishop model, and the

DRM. For  $Q_1$ , the SDM provides the best result for I–V characterization, while for  $Q_2$  the Bishop model exhibits the lowest error. In the case of the DRM, the I–V characterization depends on the accurate parameter estimation in  $Q_1$ , highlighting the impact of  $R_{sh}$  as previously discussed.

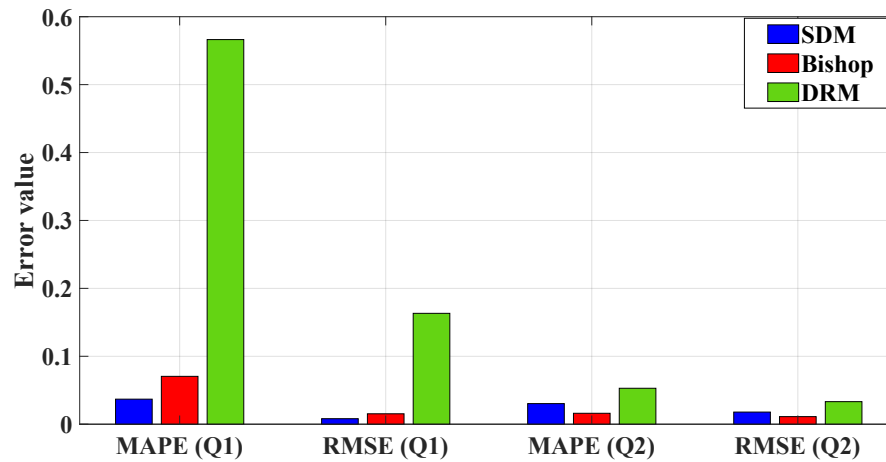


Figure A.37: Estimation error for each model.

### A.2.5. CONCLUSIONS

This paper presented a simple strategy for the I–V characterization of a PV cell considering three PV models. This proposed strategy uses GA and Simulink to extract the parameters from an experimental I–V curve.

The analysis results demonstrate that the SDM model does not correctly reproduce the cell behavior when the current grows exponentially while the voltage at the cell terminals grows negatively ( $Q_2$ ).

The parameter estimation of the DRM model, which was carried out in two stages, demonstrated that estimating the parameters per quadrant has a negative influence in the model accuracy. When estimating the parameters of the first quadrant, exclusively using the experimental information related to that quadrant, the critical parameter  $R_{sh}$  is not correctly identified, which is one of the parameters that imposes the behavior in the second quadrant. Moreover, the results reveal the need for a mathematical formulation that allows estimating the whole set of parameters of this particular model. Here, this procedure was developed with the circuital model evaluation in Simulink, which required the estimation of the five parameters for  $Q_1$  described in Table A.1 and the calculation of the parameters for  $Q_2$  (see Figure A.33), in an independent way.

It is also important to highlight that the proposed procedure can be used, along with PV array modeling methodologies, to analyze the behavior of cells operating in both  $Q_1$  and  $Q_2$ , which is needed for power analysis and losses estimation during partial shading conditions. Future works could consider estimating energy per day, month, or year using the electrical representation described for the PV cell modeling. Also, another future work could consider to apply other optimization techniques to solve the parameter estimation problem, which may reduce both estimation errors and computation time.

## A.3. A LOW-COST SYSTEM FOR REAL-TIME MEASURING OF THE SUNLIGHT INCIDENT ANGLE USING IOT

### A.3.1. HARDWARE IN CONTEXT

Photovoltaic (PV) systems are a promising alternative to reduce the use of fossil fuels. One of the main advantages of PV systems concerns the solar irradiance availability [33], which avoids the costs of fuel transportation.

The power production of a PV panel depends on the solar irradiance reaching the panel surface, which also depends on multiple factors: incident irradiance, panel orientation and inclination, shading pattern covering

the panel, among others [34]. In particular, the solar irradiance available in a geographical location can be estimated from databases [35] or using in-site sensors [36]. Similarly, the panel orientation is defined using a standard expression depending on the place latitude as it is reported in [34] and [35].

The incidence angle of the solar irradiance has a significant effect on the power production of the PV panel. Such an effect is discussed in [37], where mathematical models are used to design mechanical systems for sun tracking. Those tracking devices have the main objective of optimize, in real-time, the incidence angle of the solar irradiance; unfortunately, that work does not provide experimental verifications of the system applicability and an evaluation of the system precision. A similar work was reported in [36], where the effect of both inclination and orientation angles in the PV power production is studied. The work is based on the mathematical models of multiple cell types, but similar to the previous work, it is based on simulations without providing any experimental verification. The study reported in [38] analyses the impact of the incidence angle on the power production of grid-connected PV system installed on Northern Ireland, which is also based only on simulations. The incident angle also affect other operational aspects of the PV system; for example, in [39] is studied the effect of the incident angle on the power degradation produced by dust accumulation on the panel surface. Such a study proposes an empirical equation, based on experimental data, to estimate the incident angle effect. The previous works demonstrate the usefulness of experimental measurements of the irradiance incidence angle taken at the location of a possible PV installation.

The incident angle of the solar irradiance changes with the place elevation, and it could be affected by large geographical bodies (such as mountains) and constructions reflecting additional solar irradiance to the panel (such as windows), hence the effective irradiance magnitude reaching the PV panels will be different than the value reported by meteorological services. To face those conditions, Kyosemi Corporation (Japan) designed a PV cell with spheric geometry named SPHELAR [40], which has the objective of increasing the power density of PV system. This new geometry was designed to absorb the highest irradiance possible along the day, this based on multiple surfaces with different orientations adjusted to the incidence angles of the solar irradiance along the day. This spherical PV cell was evaluated in [40], where the performances of both spherical and traditional PV cells were contrasted, focusing the study on the power production for different incidence angles of the solar irradiance. The study demonstrated that fine-tuning the inclination and position of both spherical and traditional PV cells have a significant impact on the power production; therefore, such a study puts into evidence the need of devices for measuring, precisely, the incidence angle of the solar irradiance.

Partial shading is another phenomenon affecting the power production of PV arrays formed by series-connected modules, which corresponds to the industrial standard [33]. In particular, if a PV panel is partially shaded, the panel current is reduced in comparison with the string current, which produces the activation of the bypass diode protecting the module. Such a diode activation imposes a negative voltage at the panel terminals, which forces that panel to consume power: this operation condition, known as second-quadrant operation, reduces the power production of the PV system and decreases the panel life-time [41]. The partial shading is caused by objects adjacent to the PV panels such as buildings, posts or even other PV panels; and the shape and severity of the shades change along the day. Therefore, estimating the power production and life-time of a PV system, which is exposed to partial shading, requires the data describing the shading pattern affecting the PV array. Multiple solutions have been proposed to face this problem: for example, in [42] was analyzed the shape and trajectory of a shading pattern covering a PV system, with the aim of estimating the PV power; however, such a work does not provide experimental verification to demonstrate the applicability and precision of the proposed solution. In any case, the analysis presented in [42] puts into evidence the importance of the shading pattern analysis for commercial PV installations, which could be solved with suitable measurement devices. However, the physical location of those measurement devices must be carefully selected to cover the path of the shades along the day; for example, the measurement devices could be located at the corners of the area in which the PV field will be installed.

The previous literature review shows the need of designing devices for measuring the effect of the incidence angle on the solar irradiance reaching the PV modules, which will be useful to define the geographical location in which a PV system must be installed. Moreover, the device must take into account the change of the incidence angle along the day: for example, the device reported in [43] is based on five irradiance sensors located on perpendicular planes on a vehicle, which provides information concerning the distribution of the solar irradiance over the vehicle surfaces. Such a device is intended for supporting the design of PV arrays and PV concentrators depending on the vehicle geometry; however, it is not evident the device applicability to classical PV systems.

Another solution, presented in [44], concerns a device based on a CMOS sensor to measure the effect of the irradiance incidence angle on the power production. This device uses an electrical motor to rotate the sensor depending on the sun translation, but the electrical power required by the device, and the maintenance required by the mechanical parts, make difficult the autonomous operation of the device. Therefore, it is needed to design devices to measure and store the physical variables required to perform real-time analyses [45] with low-power consumption, which enable the on-field operation for long periods of time. Such conditions were addressed in [46] by proposing a procedure for reducing the power consumption of wireless sensors and actuators. Similarly, embedded devices require control systems for signal acquisition, processing, storing and transmission; those procedures were addressed in [47] by using a real-time operating system for embedded devices, which provides a simple but flexible programming platform. However, since the operating system is based on a central kernel, this solution could reduce the processing speed in comparison with a direct programming of the microprocessor (MCU).

Embedded devices enable to design custom solutions adjusted to particular applications. This is the case of the flight simulator reported in [48], which was designed to provide both high-realism and low implementation costs in comparison with commercial solutions. In other cases, embedded devices are used to design solutions with improved characteristics in comparison with commercial devices. This is the case of the people detection system reported in [49], where the embedded device enable to introduce higher robustness to light changes, and makes possible the connection with facial recognition systems. Such an approach can also be adopted to improve the analysis of the irradiance incident angle in PV panels: the works reported in [43] and [44] were designed for mobile applications, and those solutions consume a high amount of power, which limit the use of those devices for autonomous measurements, in remote places, and during long periods of time. Moreover, commercial devices for irradiance and shade characterization, such as [50, 51], do not take into account the changes on the irradiance incidence angle, and in some cases, data from meteorological stations is required to supply the lack of sensors.

It is also important to highlight that the effect of the Global Tilted Irradiance (GTI) has been commonly analyzed using simulations [52, 53], where the horizontal data is translated to the desired incidence angle using mathematical models [54]. Such an approximation, based on translational models, are used since traditional pyranometers are installed in horizontal planes, hence horizontal irradiance data is the only available for the PV generation analysis. Moreover, the spatial resolution of the measurements provided by traditional pyranometers can produce imprecise irradiance estimations, hence some authors have performed experiments to quantify those errors [55]. Another approach commonly adopted to estimate the particular irradiance conditions of a given area is based on commercial software and databases; but those resources do not consider some practical factors such as the albedo, dynamic shading or reflected irradiance caused by windows or other surrounding elements, thus introducing estimation errors. Those problems could be solved by measuring, on the field, the effective irradiance reaching the particular area.

Concerning commercial solutions, the device reported in [56] provides a traditional pyranometer with a manual tilt adjustment; however, such a device measures diffuse irradiance, hence the measure effectiveness depends on a correct prediction of the tilt angle. Moreover, since no additional sensors are available, it is impossible to detect the optimal incidence angle of the PV installation. Another commercial device is reported in [57], which allows to measure the Direct Normal Irradiance (DNI) and shading pattern using an array of thermopiles; however, such a device does not track the sun, hence the DNI value is not correlated with the irradiance incidence angle, hence it is not possible to estimate the optimal inclination of the array.

The previous problems are addressed in this paper by designing an embedded system able to analyze the effect of the irradiance incidence angle on a PV system, which is used to define the optimal panel angle for a particular place including all the practical conditions of the site (partial shading, reflected irradiance, etc.), thus providing high accuracy. The proposed device is formed by nine irradiance sensors located in a semi-sphere, hence each sensor measures the irradiance in a particular plane. In addition, a model is developed from the acquired data to calculate the incidence angle providing the highest PV power production. The device uses wireless internet to transfer the sensors data, where the sampling frequency is adjusted depending on the data variability to reduce the stored data, but enabling the characterization of fast changes on the ambient and shading conditions. The device is powered with a PV panel, an energy management system and a battery, which enable autonomous operation for long periods of time; therefore, a large amount of information can be obtained, which is useful for both design and optimize PV installations. In particular, the acquired data is used to estimate the

angle with the highest incidence irradiance for each interval of time, and the best panel angle is obtained from the sum of all the irradiance vectors along the day.

### A.3.2. HARDWARE DESCRIPTION

The Particle Photon has a WiFi module that allows an Internet connection, and it provides the use of the Particle Build IDE, which is a browser-based portal where the Photon code can be created, edited and saved. In addition, the Particle Photon offers a centralized IoT command center, which provides interfaces to simplify the interaction and management of Particle devices. Therefore, using that tool is possible to monitor the health of the device, regardless of the cloud service adopted. Finally, the sensors are connected to the MCU to enable the data capture, and the PV panel provides autonomy to the device.

The irradiance is measured using TLS2591 sensors, which are high sensibility photodetectors that transforms irradiance intensity into digital signals. Those sensors have high-bandwidth and infrared photodiodes for improved measurement; the sensors also integrate two Analog-to-Digital Converters (ADC) to transform the output current from the photodiodes into a digital signal representing the irradiance in each channel. Moreover, the integration time and signal gain can be configured using digital values to adjust the sensibility. The TLS2591 has a  $I^2C$  communication interface, which makes simple to exchange information with a microcontroller, and the TLS2591 does not require external conditioning circuitry. Finally, the sensor range is  $400\text{ nm} - 1100\text{ nm}$  [58].

The mechanical structure designed for imposing the sensors orientation, i.e. the sensors arcs, and the supports for the electronic components and PV panel, were all produced using an ABS 3D printer. The base and protective semisphere were constructed using transparent acrylic. As evidenced in other publications [59], the acrylic transmittance is almost uniform in the visible spectrum, thereby it does not affect the wavelength. On the other hand, the acrylic thickness affects the power because the transmittance value is lower than 100%, however, this influences all sensors uniformly. The arcs where the sensors are located were designed with the same shape as the acrylic dome, in order to avoid any influence on the angle of incidence. In other words, the arcs are parallel to the dome surface.

One important aspect was to isolate the electronics support from the device base, which avoids heat transference to the electronic components. The final prototype, depicted in Figure A.38, has the following components: 2.5 W PV panel, 6000 mA battery, DFRobot solar controller, Particle Photon embedded system, Qwiic Shield for Photon, DFRobot Gravity multiplexers, and nine TLS2591 sensors.

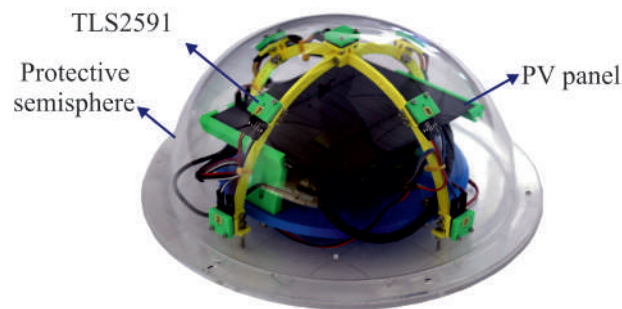


Figure A.38: Physical prototype

Each sensor was enclosed into a custom design capsule with a 1 mm hole, which ensures that the light reaching the sensor is perpendicularly oriented with respect to the sensor plane. Specifically, the hole closes the field of view at an angle of  $10^\circ$  approx, as the light travels through the 4.5mm thickness of the sensor capsule. Such a design isolates the measurement of one sensor from the measurement of the other ones; Figure A.39 shows the designed sensor capsule. The precision and homogeneity of the enclosed sensors were tested using an Ocean Optic HL2000 light source, and the sensors gains were calibrated with a Thorlab PM power measurement device. Therefore, for the same light source, the nine sensors produce the same measurement.



Figure A.39: Sensor capsule

The nine sensors were placed in two semicircular structures (arcs) to measure the light intensity in planes located at  $90^\circ$  and  $45^\circ$  for each cardinal direction (north, south, west and east), and a single sensor was located at  $0^\circ$ . Figures A.40 and A.41 show the sensors positions, using both top and frontal views, where the  $0^\circ$  plane is at the center and top of the device. Sensors 1, 2, 3 and 4 have a  $90^\circ$  inclination, while sensors 5, 6, 7 and 8 have a  $45^\circ$  inclination.

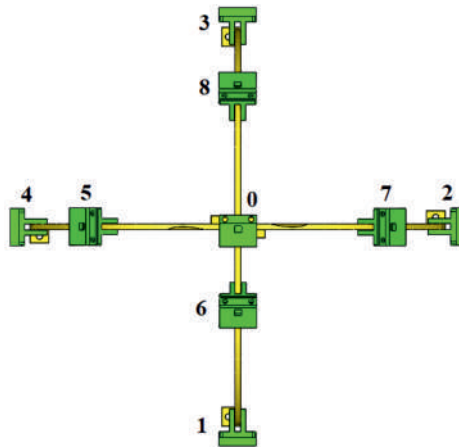


Figure A.40: Top view

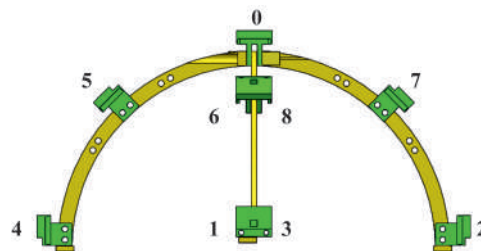


Figure A.41: Front view

Such a custom design enables to measure the irradiance at those precise inclination angles, hence the device provides the irradiance components at those particular planes. This is not possible by using multiple classical photodetectors (or pyranometers) pointing at different orientations, since those sensors are not designed to be isolated from each other, hence it is not possible to obtain information of the irradiance component in each particular plane. Therefore, such a classical solution does not allow a precise calculation of the optimal incident angle, since the same diffuse irradiance could reach two or more pyranometers at the same time, thus introducing an error on the angle estimation.

Under the sensors, the device has a 2.5 W PV panel and a 6000 mA battery, which provide complete autonomy; such a PV panel is observed in Figure A.38. The device also includes a Solar Power Manager from DFRobot,

which ensures the Maximum power Point tracking (MPPT) in the PV panel and the correct battery management [60]. Under the PV panel is located the IoT hardware, which corresponds to a Particle Photon embedded system formed by a Cortex M3 microcontroller and a WiFi Broadcom module. Such an IoT device collects the sensors data, which is transmitted using a TCP/IP internet protocol. In addition, since each TLS2591 sensor has the same  $I^2C$  address, two DFRobot Gravity multiplexers were used to communicate with the nine sensors. Finally, the embedded system has a low-power consumption mode (DeepSleep), which is used to significantly reduce the system energy consumption during the night.

The proposed hardware provides several advantages:

- The IoT characteristics enable the real-time data acquisition, which can be used for improving sun tracking systems; moreover, the device operation can be adjusted depending on the data variability (resolution and sampling time) to reduce power consumption.
- The irradiance measured by each of the nine sensors is normal to the sensor plane, hence it is a directional measurement. Such a characteristic enables to calculate the optimal incidence angle with high precision.
- The device is designed with low-cost elements, hence the overall cost of the proposed solution is lower than the cost of a commercial pyranometer and improves the type of measurement because additionally it is possible to have angle information.

### A.3.3. DESIGN FILES

Figure A.42 shows the scheme of the proposed device, where the elements and connections are described. The device uses a PV panel as main energy source, a battery for support the device operation under low-irradiance conditions, an energy management system for ensuring the correct battery charge and discharge. The embedded device (Photon WiFi Development Board) is used for signal processing and transmission, and multiplexers are used for  $I^2C$  communication. Finally, the device has nine irradiance sensors.

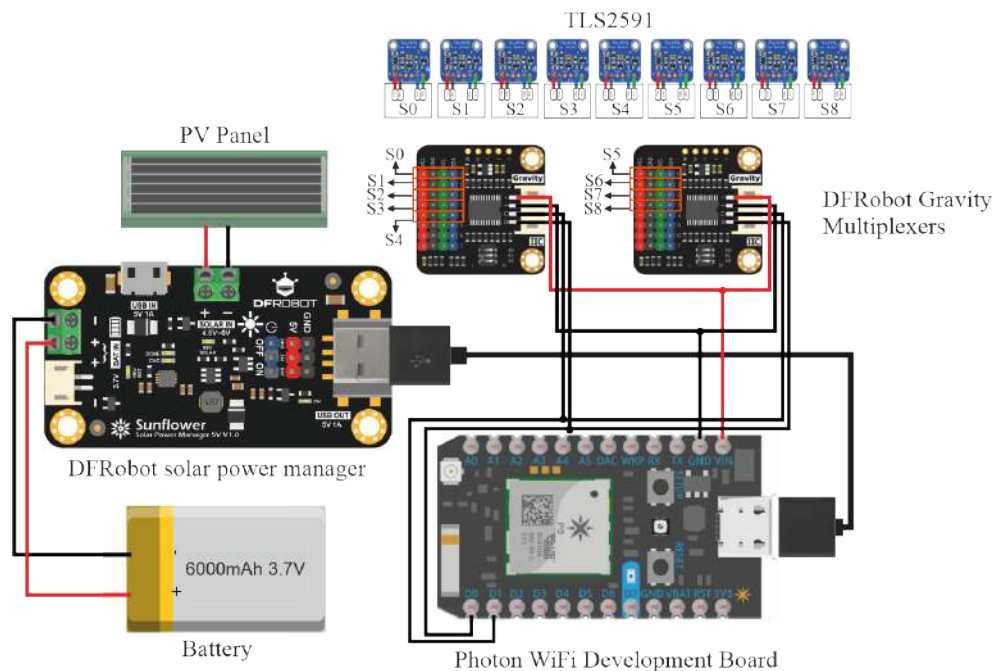


Figure A.42: Schematic

#### DESIGN FILES SUMMARY

- The *ArchSupport01* and *ArchSupport02* correspond to the arches where the sensors are positioned.
- The *BasePlate* is the support for the electronic devices.

Design file name	File type	Open source license	Location file
Box	.png	GNU General Public License (GPL) 3.0	<a href="https://osf.io/wde9j/">https://osf.io/wde9j/</a>
ArchSupport01	.stl	GNU General Public License (GPL) 3.0	<a href="https://osf.io/zu2wb/">https://osf.io/zu2wb/</a>
ArchSupport02	.stl	GNU General Public License (GPL) 3.0	<a href="https://osf.io/42csd/">https://osf.io/42csd/</a>
BasePlate	.stl	GNU General Public License (GPL) 3.0	<a href="https://osf.io/4r8b5/">https://osf.io/4r8b5/</a>
PanelSupport01	.stl	GNU General Public License (GPL) 3.0	<a href="https://osf.io/d54y9/">https://osf.io/d54y9/</a>
PanelSupport02	.stl	GNU General Public License (GPL) 3.0	<a href="https://osf.io/gnexy/">https://osf.io/gnexy/</a>
SensorSupportTop	.stl	GNU General Public License (GPL) 3.0	<a href="https://osf.io/dsycg/">https://osf.io/dsycg/</a>
SensorSupportBottom	.stl	GNU General Public License (GPL) 3.0	<a href="https://osf.io/2d8at/">https://osf.io/2d8at/</a>
SensorFixer	.stl	GNU General Public License (GPL) 3.0	<a href="https://osf.io/sa2wc/">https://osf.io/sa2wc/</a>
Schematic	.png	GNU General Public License (GPL) 3.0	<a href="https://osf.io/bywxd/">https://osf.io/bywxd/</a>
main	.ino	GNU General Public License (GPL) 3.0	<a href="https://osf.io/qnzce/">https://osf.io/qnzce/</a>

- The *PanelSupport01* and *PanelSupport02* are the elements that allow the panel to be positioned above the electronic elements attached to the *BasePlate*. In other words, they are the supports to hold the solar panel.
- The *SensorSupportTop*, *SensorSupportBottom* and *SensorFixer* are the pieces that allow to encapsulate the sensors so they can be attached to the arches.
- The *Schematic* presents the electronic schematic of the device, the main components and their connections.
- In the *main* there is a C code to read the sensors and send the information to the cloud. The code can be changed for customization.

#### A.3.4. BILL OF MATERIALS

Designator	Component	Qty	Unit cost	Total cost	Source of Materials
TLS2591	Irradiance sensor	9	\$5.95 USD	\$53.55 USD	<a href="https://www.adafruit.com/">https://www.adafruit.com/</a>
Photon shield	Qwiic Shield for Photon	1	\$5.95 USD	\$5.95 USD	<a href="http://www.sparkfun.com">www.sparkfun.com</a>
Mux	Gravity I2C Multiplexer	2	\$6.9 USD	\$13.8 USD	<a href="https://www.dfrobot.com">https://www.dfrobot.com</a>
Power Manager	Solar Power Manager 5V	1	\$7.9 USD	\$7.9 USD	<a href="https://www.dfrobot.com">https://www.dfrobot.com</a>
Acrylic Base	Acrylic Base - 18cm diameter	1	\$5.0 USD	\$5.0 USD	<a href="http://www.amazon.com">www.amazon.com</a>
Acrylic semisphere	Acrylic semisphere	1	\$39.99 USD	\$39.99 USD	<a href="http://www.amazon.com">www.amazon.com</a>
PV Panel	Solar Panel	1	\$10 USD	\$10 USD	<a href="http://www.amazon.com">www.amazon.com</a>
Photon	Photon WiFi Development Board - Particle	1	\$19 USD	\$19 USD	<a href="http://www.sparkfun.com">www.sparkfun.com</a>
PLA	Polylactic acid	1/10	18 USD	\$1.8 USD	<a href="http://www.amazon.com">www.amazon.com</a>
Battery	Lithium Ion Battery	1	\$9.95 USD	\$9.95 USD	<a href="http://www.sparkfun.com">www.sparkfun.com</a>

#### A.3.5. BUILD INSTRUCTIONS

First, the device base must be cut (*Acrylic\_Base*). The base corresponds to an acrylic circle of 18 cm in diameter. Then, the following pieces should be 3D printed, *ArchSupport01*, *ArchSupport02*, *BasePlate*, *PanelSupport01*, *PanelSupport02*, *SensorSupportBottom*, *SensorSupportTop* and *SensorFixer*. For that purpose, one can choose to use Polylactic acid (PLA) or Acrylonitrile butadiene styrene (ABS). In this case, the pieces were printed using PLA.

Above the acrylic base, a second base (File: *BasePlate*) is positioned, which aims to serve as a support for electronic devices, with the exception of the sensors and the solar panel. This base has holes that allow you to fix each of the elements and thus prevent them from moving inside the device.

Two multiplexers were employed. The multiplexers were used because the nine sensors have the same I2C address. The sensors are connected to the multiplexers and the multiplexers are connected to the shield that holds the Particle Photon. If a shield is not available, the cables from the multiplexers must be connected directly to the Particle Photon. At this point, the connection between the panel, the DFRobot solar power man-



ager, and the battery must be made. Once all the devices are connected (sensors, multiplexers, Particle Photon, Panel, solar power manager, and battery), then the solar panel supports are attached (*PanelSupport01* and *PanelSupport02*). These elements (panel supports) are attached to the *BasePlate* and allow the Solar Panel to be positioned above all the IoT hardware. In this way, the panel protects electronic devices from receiving direct sunlight and prevents them from heating up.

Now, each of the nine sensors should be attached to 3 elements: *SensorSupportBottom*, *SensorFixer*, and *SensorSupportTop*. The *SensorSupportBottom* is the element that is joined to the arches, the *SensorFixer* allows to set the height of the sensors so that it is not affected by the cable connectors, and finally the *SensorSupportTop* ensures that the light reaching the sensor is oriented perpendicularly with respect to the plane of the sensor. The proper order to couple the pieces are *SensorSupportBottom*, *SensorFixer* Sensor, and finally *SensorSupportTop*. Once the sensors are encapsulated, they can be attached to the arches (or semispheres), which in turn are assembled to the acrylic base, as can be seen in Figure A.38. Finally, the complete system is covered with the acrylic semisphere.

### A.3.6. OPERATION INSTRUCTIONS

To use the proposed device, you must first register on the Particle website. After this, it is necessary to download the Particle application, which allows you to configure the Photon WiFi Development Board so that it can receive user instructions. In addition, Particle has its own IDE available online (Particle Build IDE - <https://build.particle.io/>) to facilitate the code sending and editing. This online, browser-based IDE avoids installing any program on the PC, which is also an advantage for non-expert users. After sending the code to the Photon, WiFi credentials must be updated, either using the app mentioned above or using the console.

At this point you must choose the cloud service that will be used. In the market there are a wide variety of companies that provide this service, and in this case Ubidots was chosen. If the user prefers a different company, then it will be necessary to update some elements of the code and libraries according to the specific cloud service. For Ubidots, there is a unique token number for each user that must be updated before sending data to the Internet. Moreover, it is necessary to verify that in the compilation directives "ubienable" has a value of 1, in the case of other cloud services it must be 0. Finally, for the data to be transmitted through the serial port, "printenable" must be at 1.

Regarding the transmission of the data, the TLS2591 sensor delivers a visible radiation measurement and another global measurement with visible radiation plus infrared. Both values are sent to the cloud every two minutes. However, this time interval can be modified according to the user's needs. Finally, it is important to mention that each sensor has a label to be identified when transmitting the information.

### A.3.7. VALIDATION AND CHARACTERIZATION

The operation of the proposed device was tested on the field, at a roof located in Medellin-Colombia, where a PV array is also in operation; the location of the experiments is described in Figure A.43. The PV system depicted in the figure has a peak power 1.3 kW, and it has instrumentation that provides voltage and current data, which is used for the device validation.



Figure A.43: PV system and proposed prototype installed at  $6^{\circ}14'39.9''N - 75^{\circ}33'07.0''W$ .

## DATA TRANSMISSION AND POWER CONSUMPTION

The irradiance data was sampled each minute, in average, since the sampled time is controllable depending on both the power availability and data variability. In the device, the highest power consumption corresponds to the data transmission to the cloud; therefore, the data transmission rate was limited to reduce the power consumption. Such a procedure was implemented by storing the irradiance data into the NVRAM of the MCU to be transmitted in four-samples packets; moreover, the WiFi module is disabled when the sensors data is acquired. Both strategies enable to save up to 70% of the energy in comparison with a non-optimized operation, i.e. transmitting one data in each cycle, and without disabling the WiFi module at the acquisition time. Figure A.44 presents an example of the current consumption for both modes,  $Mode_1$  is the non-optimized operation, while  $Mode_2$  is the optimized condition: the difference between the current consumption is caused by the time in which the WiFi module is turned on, this example shows the large energy saving achieved with the operation strategy adopted for the proposed device. In particular,  $T_1$  and  $T_2$  correspond to the time intervals in which the WiFi module is disabled and enabled for  $Mode_1$ , respectively; while  $T_3$  and  $T_4$  correspond to the time intervals in which the WiFi module is disabled and enabled for  $Mode_2$ , respectively.

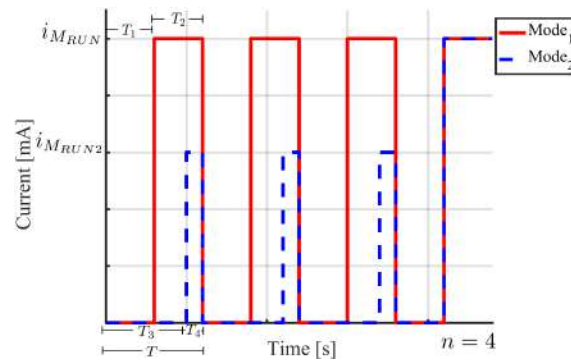


Figure A.44: Energy consumption comparison for traditional ( $Mode_1$ ) and optimized ( $Mode_2$ ) modes.

## VECTORIAL REPRESENTATION OF THE IRRADIANCE DATA

The sensors data are compressed in a vectorial representation to define the orientation of the maximum solar irradiance, which represents both the magnitude and incidence angle of the irradiance. Figure A.45 shows this concept using the sensors data recorded in Medellin-Colombia at 31-08-2019; where the black and cyan vectors represent the irradiance magnitude in each sensor at a given instant of time. Those vectors have a direction defined by the sensor position on the device; hence each sensor imposes the direction vector and magnitude, where that magnitude corresponds to the measured irradiance. In Figure A.45, the three-dimensional cartesian space is defined by the red, green, and blue axes; while the magenta vector  $S$  is the vectorial sum of the nine sensors vectors. Such a vector  $S$  provides the orientation and magnitude of the maximum solar irradiance at that particular location and time. To calculate the  $S$  value for a given period, e.g. a day, the vectors generated by the set of sensors are added using all the measurements along the period. Such information is useful to evaluate the effect of the irradiance incidence angle on the behavior of PV systems, which also helps to define the optimal orientation of the PV panel.

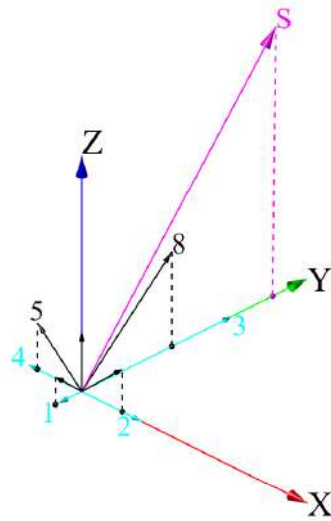


Figure A.45: Sensors' vectorial representation at a given instant of time

#### EXPERIMENTAL MEASUREMENTS

The proposed device was located so that the device axes coincide with the cardinal directions: the axis with sensors 1, 6, 0, 8 and 3 was oriented from east to west. The measurements were taken during two days, from August 31/2019 to September 01/2019, and those are reported in figures A.46a, A.46b, A.47a and A.47b. Moreover, figures A.46a-A.46b present the Hilbert transformation envelope of the experimental data to compensate for shading and irradiance variations, which are neglected for comparison purposes. The Hilbert transformation envelope is a waveform connecting the maximum values of a signal with high-frequency variations, thus filtering those high-frequency variations. In those figures, signal  $F0$  corresponds to the data from sensor 0, and signal  $eF0$  corresponds to the envelope calculated from signal  $F0$ .

Figures A.46a and A.46b show the measurements for sensors 0, 2, 4, 5, 6, 7 and 8 for August 31/2019. Figure A.46a shows that sensor 6, placed in a plane at  $45^\circ$  east, has the highest irradiance at morning when the sun light is perpendicular to that position. Similarly, the highest irradiance for sensor 0 occurs at noon since at that time the sun light is perpendicular. Finally, the highest irradiance in sensor 8 occurs in afternoon since that sensor is placed in a  $45^\circ$  west plane. Those measurements put into evidence the relation between the panel inclination angle and the power production, which could be used to calculate, accurately, the best inclination angle that guarantee the overall highest energy production along the day, or even, along the period in which the data is recorded (a week, a month, a year). Similarly, Figure A.46b presents the data from sensors 2, 4, 5 and 7, which are placed in south-north orientation. Such data enable to perform a  $360^\circ$  position analysis to define the best orientation and inclination of a PV panel depending on the irradiance incidence angle at each instant of time.

Figure A.47a shows the irradiance data obtained by the prototype for September 01/2019, which are in agreement with the data of August 31/2019 concerning the time in which the sensors exhibit the highest irradiance

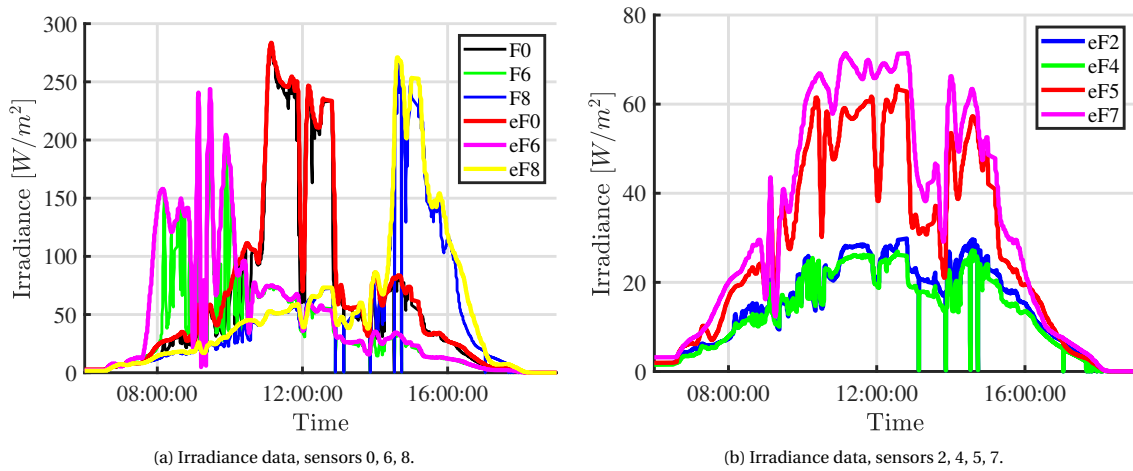


Figure A.46: Irradiance data for 31-08-2019

magnitude. However, in this new case (01-09-2019), Sensor 0 exhibits a much higher irradiance magnitude in comparison with the other sensors, which could be due to clouding conditions at both morning and afternoon, hence having a day with a higher irradiance at noon. Figure A.47b shows the irradiance data captured by sensors 2, 4, 5 and 7 for the same day where, despite the irradiance increment observed in Figure A.47a, the sensors placed in the south-north orientation do not experiment a significant irradiance increment in comparison with the previous day.

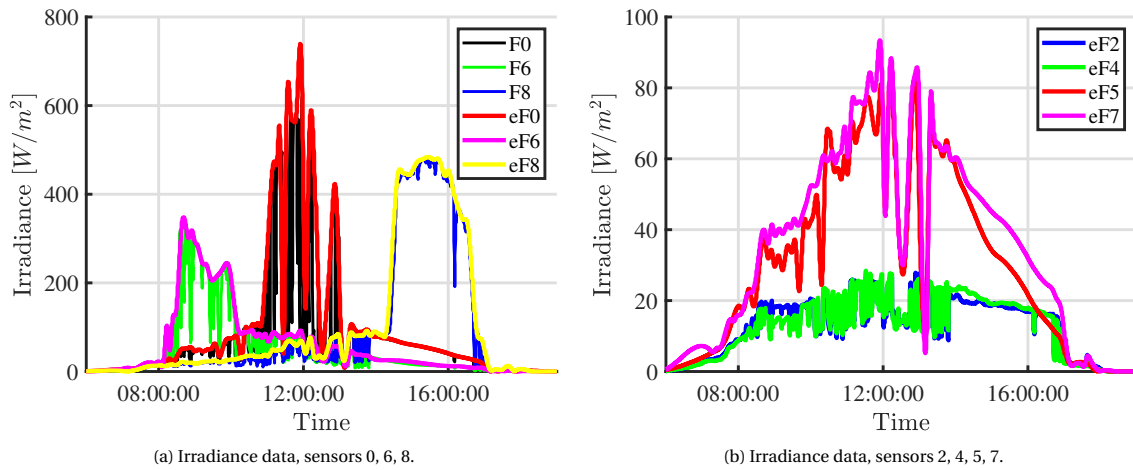


Figure A.47: Irradiance data for 01-09-2019

#### DATA COMPARISON

The irradiance data provided by the proposed prototype is contrasted with the power generated by the PV installation located at the same rooftop used for the experimental test. The PV panels are installed at  $0^\circ$  with respect to the horizontal plane, which corresponds to the inclination of Sensor 0 of the proposed device. However, the PV panels are also affected by the diffuse components caused by other objects. Figure A.48a shows the power generated by the PV panels during August 31/2019, which is in agreement with the irradiance peaks observed in Figure A.46a for the morning, noon and afternoon hours; the current and power data of the PV panels were registered once per minute. Such a correlation confirms that the power generated by a PV panel is caused by the different irradiance levels occurring at different incidence angles; moreover, the data shows that the proposed device is a useful tool for defining the optimal inclination angle for the PV system. Finally, Figure A.48b shows

the power generated by the PV panels during September 01/2019, which is also in agreement with the irradiance peaks observed in Figure A.47b.

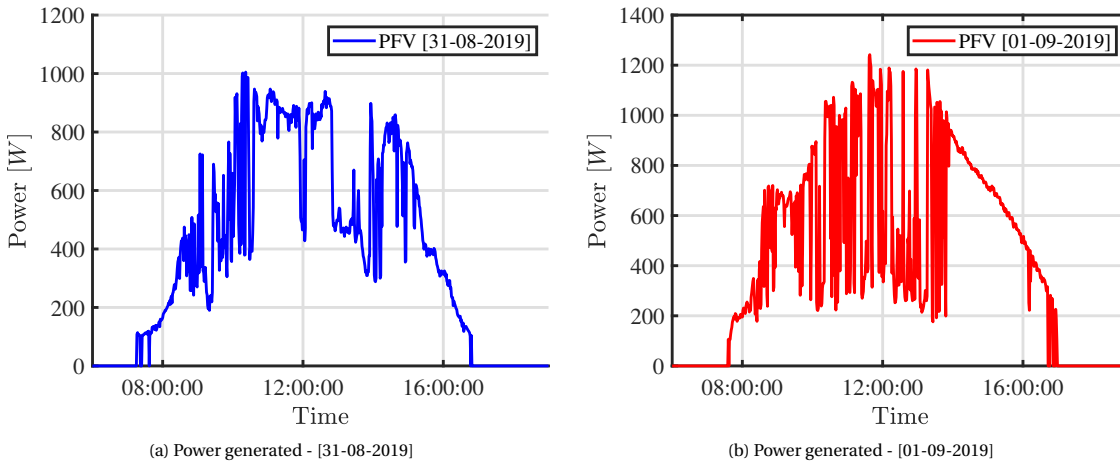


Figure A.48: Generated power

#### ESTIMATION OF THE OPTIMAL INCLINATION ANGLE

One of the main advantages of the proposed prototype, over geographical estimations, is the measurement of on-site conditions, which are difficult to simulate or estimate since, for example, new constructions could produce significant irradiance reflections. Then, using the aggregated irradiance vector, obtained from the vectorial sum of the nine sensors data described in Section A.3.7, figures A.49 and A.50 show the resulting black vectors normalized for each instant of time along the day. The vectors have been normalized to enable a clear visualization of the maximum irradiance angle without accounting for the irradiance magnitude, and such an angle is in agreement with the sun movement for this particular experiment. However, in crowded urban environments, the irradiance reflected by buildings and other objects could produce a different optimal trajectory.

Using the vectors of maximum irradiance for each sampled time, the averaged maximum irradiance vector is calculated, which is depicted in magenta in both figures A.49 and A.50. Such a vector provides the optimal inclination angle for the PV panels located in that particular place during those particular days: for 31-08-2019, the spheric coordinates of that averaged vector are  $[r1.0, \theta74.96, \phi6.59]$ , while for 01-09-2019 the averaged vector coordinates are  $[r1.0, \theta85.29, \phi10.31]$ . In those data,  $\theta$  represents the angle with respect to east-west plane, while  $\phi$  represents the inclination angle with respect to the horizontal plane.

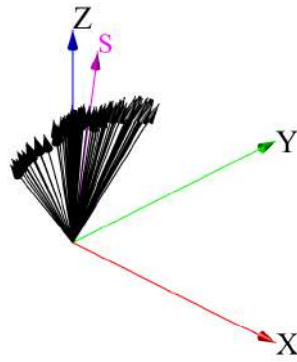


Figure A.49: Higher irradiance vectors: 31-08-2019

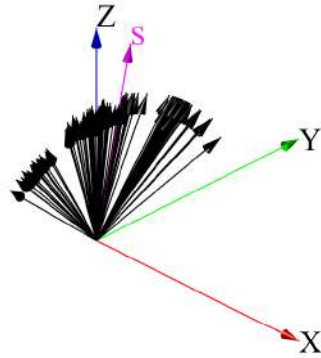


Figure A.50: Higher irradiance vectors: 01-09-2019

Table A.8 presents the normalized integral of the irradiance in each sensor of the proposed device for August 31 to September 05, 2019. Those values were obtained by integrating the irradiance curve of each sensor independently, then the data was normalized with respect to the maximum value obtained on the day. Therefore, in the table, the maximum irradiance for each day has a value of 1.0 highlighted in green. From those results is observed that the maximum irradiance was obtained mostly by sensor number 8, while sensor 0 is often in second place; hence those sensors produce the vectors closer to the optimal vector S, which is also reported in Table A.8. For example, in September 01/2019 the maximum normalized value was obtained in Sensor 8, which is in agreement with Figure A.47a, where such a sensor receives a large amount of irradiance in the afternoon. Contrasting August 31/2019 and September 01/2019 it is observed that the latter one has higher irradiance values, i.e. a sunny day; moreover, at afternoons it is observed that Sensor 8 shows less changes on September 01/2019, which indicates a less cloudy day. The previous analysis is possible due to the large amount of data provided by the proposed device, which can be used to characterize a particular location in which a PV system will be installed.

Finally, the data of some of the sensors is stable for those days, which can be used to reconstruct the shading pattern caused by clouds or surrounding objects. Such an information can be used for reconfiguration purposes, which is another useful strategy to improve the power production of PV installations.

Table A.8: Normalized integral of the irradiance

		[31-08]	[01-09]	[02-09]	[03-09]	[04-09]	[05-09]	Mean
Vector S	r	1.00	1.00	1.00	1.00	1.00	1.00	1.00
	$\theta$	74.96	85.29	80.13	77.03	83.22	84.26	80.81
	$\phi$	6.59	10.31	8.45	7.33	9.57	9.94	8.70
SENSORS	0	1.00	0.70	0.71	1.00	0.71	0.72	0.87
	1	0.22	0.15	0.46	0.36	0.30	0.35	0.33
	2	0.26	0.14	0.26	0.49	0.35	0.22	0.31
	3	0.33	0.26	0.29	0.37	0.51	0.37	0.38
	4	0.23	0.14	0.22	0.43	0.17	0.18	0.25
	5	0.44	0.27	0.48	0.59	0.43	0.43	0.47
	6	0.60	0.50	0.58	0.63	0.60	0.52	0.61
	7	0.52	0.31	0.42	0.59	0.32	0.48	0.47
	8	0.79	1.00	1.00	0.78	1.00	1.00	1.00

### A.3.8. APPLICATION EXAMPLE

In order to validate the proposed solution, a comparative simulation was performed in the System Advisor Model (SAM) software, which is commonly used for design and simulation of renewable energy generation systems. For this example it is considered a design of a 1.3 kW PV array connected to a grid-connected inverter; moreover, the SAM calculations are performed considering the irradiance measured in the real PV installation during the experiments described in the previous subsections, which will enable to validate the results provided by the proposed device.

The SAM software was used to simulate the PV power production for different inclination angles (*Tilt* angle) with respect to the horizontal axis, and for different orientation angles (*Azimuth* angle) with respect to the south-north plane; those simulations were used to validate the device results given in Table A.8. The results of the SAM simulation are reported in Table A.9, where the locations of sensors 0, 5, 6, 7 and 8 define the *Tilt* and *Azimuth* angles for the simulations; then the table reports the Annual Energy production (in kWh) predicted for the PV installation for those *Tilt* and *Azimuth* angles. Moreover, a SAM simulation for the optimal vector S [ $r = 1.0, \theta = 80.81, \phi = 8.70$ ] was also conducted, which corresponds to  $Tilt = 8.70^\circ$  and  $Azimuth = 170.81^\circ$  in the PV installation.

Table A.9 confirms that the highest energy production for the irradiance registered in 2019 occurs with the optimal *Tilt* and *Azimuth* angles defined by proposed device, which validates de measurements and analyses of the IoT device: PV installations configured with the optimal irradiance vector S will produce higher annual energy. The SAM simulations also shows that the second higher energy generation occurs with the *Tilt* and *Azimuth* angles of Sensor 0, hence the PV panels parallel to the horizontal axis; however, such a solution does not allow the air circulation around the panels, hence increasing the panels temperature, which could lead to overheating failures. In fact, that is the real orientation and inclination angle of the PV installation depicted in Figure A.43. The third highest energy production corresponds to the position of Sensor 6, in which the modules are located facing the east with an inclination of 45 degrees, which is a viable configuration for a PV installation on a roof.

On the other hand, it is also noted that the SAM simulation for the angles of Sensor 8 (facing the west with an inclination of 45 degrees) predicts a low annual energy, which is not in agreement with the data of Table A.8 reported by the proposed device. Instead, in Table A.8 the Sensor 8 reports a higher normalized integral of the irradiance in comparison with sensors 5, 6 and 0. Such a difference puts into evidence a significant advantage of the proposed device: the commercial design software (such as SAM) does not take into account the dynamic shading profile and reflective or diffuse irradiance caused by surrounding objects (such as windows), which could lead the software to disregard an orientation option that could produce high power under the real operation conditions of the particular installation. For the example of Sensor 8, the in-situ experimental measurements provided by the IoT device report a high irradiance profile produced by the particular conditions of the location, which will be translated in a high power production; however, the SAM simulation is not able to take into account those real conditions.

This example shows the applicability of this IoT device to define the optimal locations for PV installations in



urban environments, where the panels could be exposed to different shading patterns, or to diffuse and reflective irradiance caused by surrounding objects, which are complex conditions difficult to predict using software packages such as SAM. Another application for the IoT device concerns the interaction with a mechanical tracking system for PV arrays, which could enable the tracking system to follow the sun and avoid deep shading conditions using the IoT device data in real-time, thus improving the energy generation of the PV installation.

Table A.9: PV Simulation using SAM

		<b>Azimuth</b>	<b>Tilt</b>	<b>Annual Energy [kWh]</b>
	0	0	0	1718.55
	5	180	45	1447.32
	6	90	45	1472.49
	7	0	45	1301.39
SENSORS	8	270	45	1427.79
OPTIMAL ANGLE		170.81	8.70	1727.80

Some features and limitations of the device are summarized as follows:

- The IoT characteristics enable the real-time data acquisition, which can be used for improving sun tracking systems; moreover, the device operation can be adjusted depending on the data variability (resolution and sampling time) to reduce power consumption.
- The irradiance measured by each of the nine sensors is normal to the sensor plane, hence it is a directional measurement. Such a characteristic enables to calculate the optimal incidence angle with high precision.
- The device is designed with low-cost elements, hence the overall cost of the proposed solution is lower than the cost of a commercial pyranometer.
- The operation time of the device depends on the energy stored in the battery, thus it requires enough solar irradiance to charge the battery for a full cycle. However, under raining conditions, the battery could be discharged, and the device will be out-of-operation until a minimum battery charge is restored.
- The device can only be programmed using the Particle IDE. This online IDE is ideal for non-expert users, since it does not require the installation of any program on your PC.

With the analysis made in this work, it is possible to establish using a tool for the design of a PV array installation considering the shading incident on the array.

## A.4. PRODUCTS

Products obtained during the master's degree duration

### Articles:

- PV Array Reconfiguration Based on Genetic Algorithm for Maximum Power Extraction and Energy Impact Analysis. Sustainability (MDPI). 2022.
- Analysis of electrical models for photovoltaic cells under uniform and partial shading conditions. International Journal of Electrical and Computer Engineering (IJECE). 2021.
- Low-cost system for sunlight incidence angle measurement using Optical Fiber. HardwareX. 2022. Publicado.

### Software registration:

- GUIDE de dimensionamiento de arreglos PV. Graphical interphase developed in Python.

### Lectures (speaker):

- Analysis of quasi-resonant inverter for domestic induction heating applications. X SICEL 2021. 2021.

**Students guided:**

- Alejandra Ortiz Pasos. Desarrollo de un modelo de representación para celdas fotovoltaicas, operando en modo directo e inverso.
- Juan Manuel Arango Castaño. Identificación de patrones de sombreado en sistemas fotovoltaicos.
- Dany Castrillón Ocampo. Detección de puntos calientes en sistemas fotovoltaicos.
- Duván Antonio Salamandra Murillo, Jhon Camilo Moreno Perea. Análisis experimental del comportamiento bajo sombreado parcial de arreglos en serie de celdas PV.
- Bayron Moncada Peláez, Hugo Albeiro Muñoz Hernández. Pruebas Oscuras en Sistemas Fotovoltaicos.
- Víctor Manuel Berrio Calle, Alexander Eduardo García Mendoza. Desarrollo de Algoritmo PBIL para Estimación de Parámetros en Paneles Fotovoltaicos.

## BIBLIOGRAPHY

- [1] MA Abo-Sennah, MA El-Dabah, and Ahmed El-Biomey Mansour. Maximum power point tracking techniques for photovoltaic systems: a comparative study. *International Journal of Electrical & Computer Engineering (2088-8708)*, 11(1), 2021.
- [2] Zhaodong Wen, Jun Chen, Xian Cheng, Haiyan Niu, and Xuetao Luo. A new and simple split series strings approach for adding bypass diodes in shingled cells modules to reduce shading loss. *Solar Energy*, 184:497–507, 2019.
- [3] A Rezaee Jordehi. Parameter estimation of solar photovoltaic (pv) cells: A review. *Renewable and Sustainable Energy Reviews*, 61:354–371, 2016.
- [4] Fabricio Bradaschia, Marcelo C Cavalcanti, Aguinaldo José do Nascimento, Emerson Alves da Silva, and Gustavo Medeiros de Souza Azevedo. Parameter identification for pv modules based on an environment-dependent double-diode model. *IEEE Journal of Photovoltaics*, 9(5):1388–1397, 2019.
- [5] JW Bishop. Computer simulation of the effects of electrical mismatches in photovoltaic cell interconnection circuits. *Solar cells*, 25(1):73–89, 1988.
- [6] Abdallah Zegaoui, Pierre Petit, Michel Aillerie, Jean-Paul Sawicki, and Jean-Pierre Charles. Experimental validation of photovoltaic direct and reverse mode model. influence of partial shading. *Energy Procedia*, 18:1247–1253, 2012.
- [7] Shangce Gao, Kaiyu Wang, Sichen Tao, Ting Jin, Hongwei Dai, and Jiujun Cheng. A state-of-the-art differential evolution algorithm for parameter estimation of solar photovoltaic models. *Energy Conversion and Management*, 230:113784, 2021.
- [8] Naima Hamid, Rachida Abounacer, Mohammed Idali Oumhand, M'barek Feddaoui, and Driss Agliz. Parameters identification of photovoltaic solar cells and module using the genetic algorithm with convex combination crossover. *International Journal of Ambient Energy*, 40(5):517–524, 2019.
- [9] Madhav Kumar et al. Modelling and parameter estimation of solar cell using genetic algorithm. In *2019 International Conference on Intelligent Computing and Control Systems (ICCS)*, pages 383–387. IEEE, 2019.
- [10] Cecilia Tang and Hang Zhou. Inverse modelling of pv power prediction based on ga method. In *IOP Conference Series: Earth and Environmental Science*, volume 675, page 012080. IOP Publishing, 2021.
- [11] Angel Marinov, Svetlozar Zahariev, Ivelin Ivanov, and Toncho Papanchev. Genetic algorithm for generation of pv panel curves from datasheets. In *2021 17th Conference on Electrical Machines, Drives and Power Systems (ELMA)*, pages 1–4. IEEE, 2021.
- [12] Jhon Jairo Montano, Luis F Grisales Noreña, Andres Felipe Tobon, and Daniel Gonzalez Montoya. Estimation of the parameters of the mathematical model of an equivalent diode of a photovoltaic panel using a continuous genetic algorithm. *IEEE Latin America Transactions*, 20(4):616–623, 2022.
- [13] Zewei Yang, Kailin Liao, Jun Chen, Lei Xia, and Xuetao Luo. Output performance analysis and power optimization of different configurations half-cell modules under partial shading. *Optik*, 232:166499, 2021.
- [14] Manit Seapan, Yoshihiro Hishikawa, Masahiro Yoshita, and Keiichi Okajima. Detection of shading effect by using the current and voltage at maximum power point of crystalline silicon pv modules. *Solar Energy*, 211:1365–1372, 2020.
- [15] Idriss Hadj Mohammed, Amar Hadj Arab, Yahia Bakelli, Messaouda Khennene, Samir Hamid Oudjana, Amor Fezzani, Layachi Zaghba, et al. Outdoor study of partial shading effects on different pv modules technologies. *Energy Procedia*, 141:81–85, 2017.
- [16] Abdallah Zegaoui, Mohamed Boutoubat, Jean-Paul Sawicki, Fatma Zohra Kessaissia, Abdelkader Djahbar, and Michel Aillerie. Enhanced model of photovoltaic cell/panel/array considering the direct and reverse modes. In *AIP Conference Proceedings*, volume 1968, page 030015. AIP Publishing LLC, 2018.

- [17] HA Koffi, A Kuditcher, VCK Kakane, EA Armah, AA Yankson, and JKA Amuzu. The shockley five-parameter model of a solar cell: A short note. *African Journal of Science, Technology, Innovation and Development*, 7(6):491–494, 2015.
- [18] Robert L Boylestad and Louis Nashelsky. *Electronic devices and circuit theory*. Pearson Educación, 2002.
- [19] Abdallah Zegaoui, P Petit, M Aillerie, JP Sawicki, AW Belarbi, MD Krachai, and JP Charles. Photovoltaic cell/panel/array characterizations and modeling considering both reverse and direct modes. *Energy Procedia*, 6:695–703, 2011.
- [20] Pierre Petit, Abdallah Zégaoui, Michel Aillerie, Jean-Paul Sawicki, and Jean-Pierre Charles. The transistor based direct and reverse mode model for photovoltaic strings and panels. *Energy Procedia*, 18:1240–1246, 2012.
- [21] Kashif Ishaque and Zainal Salam. An improved modeling method to determine the model parameters of photovoltaic (pv) modules using differential evolution (de). *Solar energy*, 85(9):2349–2359, 2011.
- [22] Xiong Luo, Longpeng Cao, Long Wang, Zihan Zhao, and Chao Huang. Parameter identification of the photovoltaic cell model with a hybrid jaya-nm algorithm. *Optik*, 171:200–203, 2018.
- [23] Faisal Ghani, EF Fernandez, F Almonacid, and TS O'Donovan. The numerical computation of lumped parameter values using the multi-dimensional newton-raphson method for the characterisation of a multi-junction cpv module using the five-parameter approach. *Solar Energy*, 149:302–313, 2017.
- [24] Amit Jain and Avinashi Kapoor. Exact analytical solutions of the parameters of real solar cells using lambert w-function. *Solar Energy Materials and Solar Cells*, 81(2):269–277, 2004.
- [25] Manoharan Premkumar, Umashankar Subramaniam, Thanikanti Sudhakar Babu, Rajvikram Madurai Elavarasan, and Lucian Mihet-Popa. Evaluation of mathematical model to characterize the performance of conventional and hybrid pv array topologies under static and dynamic shading patterns. *Energies*, 13(12):3216, 2020.
- [26] Tong Kang, Jiangang Yao, Min Jin, Shengjie Yang, and ThanhLong Duong. A novel improved cuckoo search algorithm for parameter estimation of photovoltaic (pv) models. *Energies*, 11(5):1060, 2018.
- [27] Tae Hee Jung, Jae Woo Ko, Gi Hwan Kang, and Hyung Keun Ahn. Output characteristics of pv module considering partially reverse biased conditions. *Solar Energy*, 92:214–220, 2013.
- [28] DL King, JK Dudley, and WE Boyson. Pvsim ©: A simulation program for photovoltaic cells, modules, and arrays. Technical report, Sandia National Labs., Albuquerque, NM (United States), 1996.
- [29] Volker Quaschnig and Rolf Hanitsch. Numerical simulation of current-voltage characteristics of photovoltaic systems with shaded solar cells. *Solar energy*, 56(6):513–520, 1996.
- [30] Juan David Bastidas-Rodriguez, Giovanni Petrone, Carlos Andrés Ramos-Paja, and Giovanni Spagnuolo. A genetic algorithm for identifying the single diode model parameters of a photovoltaic panel. *Mathematics and Computers in Simulation*, 131:38–54, 2017.
- [31] Vun Jack Chin, Zainal Salam, and Kashif Ishaque. An accurate and fast computational algorithm for the two-diode model of pv module based on a hybrid method. *IEEE transactions on Industrial Electronics*, 64(8):6212–6222, 2017.
- [32] Jerry Kumar, Nanik Ram Parhyar, Manoj Kumar Panjwani, and Danish Khan. Design and performance analysis of pv grid-tied system with energy storage system. *International Journal of Electrical and Computer Engineering*, 11(2):1077, 2021.
- [33] E. Romero-Cadaval, G. Spagnuolo, L. Garcia Franquelo, C.A. Ramos-Paja, T. Suntio, and W.M. Xiao. Grid-connected photovoltaic generation plants: Components and operation. *IEEE Industrial Electronics Magazine*, 7(3):6–20, Sept 2013.

- [34] Giovanni Petrone, Carlos Andres Ramos-Paja, and Giovanni Spagnuolo. *Photovoltaic Sources Modeling*. Wiley-IEEE Press, 2016.
- [35] Laura Herrera, Alina Miranda, Eliana I. Arango, Carlos A. Ramos-Paja, and Daniel Gonzalez. Dimensionamiento de sistemas de generación fotovoltaicos localizados en la ciudad de medellín. *TecnoLógicas*, pages 289–301, 2013.
- [36] Taeyon Hwang, Seokyoung Kang, and Jeong Tai Kim. Optimization of the building integrated photovoltaic system in office buildings—focus on the orientation, inclined angle and installed area. *Energy and Buildings*, 46:92 – 104, 2012. Sustainable and healthy buildings.
- [37] Guihua Li, Jingjing Tang, and Runsheng Tang. Performance and design optimization of a one-axis multiple positions sun-tracked v-trough for photovoltaic applications. *Energies*, 12(6):1141, Mar 2019.
- [38] Jayanta Deb Mondol, Yigzaw G. Yohanis, and Brian Norton. The impact of array inclination and orientation on the performance of a grid-connected photovoltaic system. *Renewable Energy*, 32(1):118 – 140, 2007.
- [39] P. Nepal, M. Korevaar, H. Ziar, O. Isabella, and M. Zeman. Accurate soiling ratio determination with incident angle modifier for pv modules. *IEEE Journal of Photovoltaics*, 9(1):295–301, Jan 2019.
- [40] Tadeusz Rodziewicz, Josuke Nakata, Kenichi Taira, Aleksander Zaremba, and Maria Wactawek. Impact of the solar irradiation angle on the work of modules with spherical cells - simulation. *Ecological Chemistry and Engineering S*, 25(1):35–50, 2018.
- [41] G. Spagnuolo, G. Petrone, B. Lehman, C.A. Ramos-Paja, Ye Zhao, and M.L. Orozco Gutierrez. Control of photovoltaic arrays: Dynamical reconfiguration for fighting mismatched conditions and meeting load requests. *IEEE Industrial Electronics Magazine*, 9(1):62–76, March 2015.
- [42] Samer Yassin Alsadi and Yasser Fathi Nassar. A general expression for the shadow geometry for fixed mode horizontal, step-like structure and inclined solar fields. *Solar Energy*, 181:53 – 69, 2019.
- [43] Yasuyuki Ota, Taizo Masuda, Kenji Araki, and Masafumi Yamaguchi. A mobile multipyranometer array for the assessment of solar irradiance incident on a photovoltaic-powered vehicle. *Solar Energy*, 184:84 – 90, 2019.
- [44] J. P. d. C. da Costa, R. H. Gounella, W. B. Bastos, E. Longo, and J. P. Carmo. Photovoltaic sub-module with optical sensor for angular measurements of incident light. *IEEE Sensors Journal*, 19(8):3111–3120, April 2019.
- [45] Alfons Crespo and Alejandro Alonso. Una panorámica de los sistemas de tiempo real. *Revista Iberoamericana de Automática e Informática industrial*, 3(2):7–18, 2006.
- [46] Diego Martínez, Patricia Balbastre, Francisco Blanes, José Simo, and Alfons Crespo. Procedimiento de diseño para minimizar el consumo de potencia y los retrasos en wsan. *Revista Iberoamericana de Automática e Informática industrial*, 7(3):95–110, 2010.
- [47] Adel Fernández Prieto and Orestes Llanes-Santiago. Núcleo de control para sistemas empotrados de control: Una propuesta de arquitectura. *Revista Iberoamericana de Automática e Informática industrial*, 8(1):64–79, 2011.
- [48] J.J. Ortega and M. Sigut. Prototipo de una plataforma móvil de bajo coste para simulación de vuelo de alto realismo. *Revista Iberoamericana de Automática e Informática industrial*, 13:293–303, 2016.
- [49] M. Castrillón-Santana, J. Lorenzo-Navarro, and D. Hernández-Sosa. Conteo de personas con un sensor rgbd comercial. *Revista Iberoamericana de Automática e Informática industrial*, 11(X):348–357, 2014.
- [50] KIIPZONEN. Smp 22 pyranometer, 2020.
- [51] Hukseflux. Hukseflux pyranometer, 2020.

- [52] Abdelatif Takilalte, Samia Harrouni, Mohamed Rédha Yaiche, and Llanos Mora-López. New approach to estimate 5-min global solar irradiation data on tilted planes from horizontal measurement. *Renewable Energy*, 145:2477–2488, jan 2020.
- [53] Smajil Halilovic, Jamie M. Bright, Wiebke Herzberg, and Sven Killinger. An analytical approach for estimating the global horizontal from the global tilted irradiance. *Solar Energy*, 188(June):1042–1053, 2019.
- [54] J. Polo, S. Garcia-Bouhaben, and M. C. Alonso-García. A comparative study of the impact of horizontal-to-tilted solar irradiance conversion in modelling small PV array performance. *Journal of Renewable and Sustainable Energy*, 8(5), 2016.
- [55] Caio Felipe Abe, João Batista Dias, Gilles Notton, and Ghjuvan Antone Faggianelli. Experimental application of methods to compute solar irradiance and cell temperature of photovoltaic modules. *Sensors (Switzerland)*, 20(9), 2020.
- [56] DeltaOhm. LPPYRA02, 2020.
- [57] DeltaT. SPN1, 2020.
- [58] AMS. TSL2591, 2019.
- [59] Xiaoyu Yang, Nan Li, Yuekun Heng, Xiaohui Qian, Xiaoyan Ma, Yuesheng Tang, Jianxia Xiao, Gaofeng Zhang, Wei Cheng, Hongbing Song, Mengzhao Li, Zhiyan Cai, Kaixi Huang, Zhi Wu, Wei He, and Yatian Pei. Study on acrylic transmittance for JUNO Central Detector. *Radiation Detection Technology and Methods*, 5(2):284–289, jun 2021.
- [60] DFROBOT. DFRobot 2019, 2019.

